NASA CONTRACTOR REPORT

NASA CR-732

NASA CR-732

STEADY-STATE AND DYNAMIC PROPERTIES OF JOURNAL BEARINGS IN LAMINAR AND SUPERLAMINAR FLOW REGIMES

I. TILTING-PAD BEARINGS

by F. K. Orcutt

Prepared by
MECHANICAL TECHNOLOGY INCORPORATED
Latham, N. Y.
for Lewis Research Center

NATIONAL AERONAUTICS AND SPACE ADMINISTRATION • WASHINGTON, D. C. • APRIL 1967

NASA CR-732

STEADY-STATE AND DYNAMIC PROPERTIES OF JOURNAL BEARINGS IN LAMINAR AND SUPERLAMINAR FLOW REGIMES

I. TILTING-PAD BEARINGS

By F. K. Orcutt

Prepared under Contract No. NASw-1021 by
MECHANICAL TECHNOLOGY INCORPORATED
Latham, N. Y.

for Lewis Research Center

NATIONAL AERONAUTICS AND SPACE ADMINISTRATION

FOREWORD

The work described in this report was performed by Mechanical Technology Incorporated under NASA Contract NASw-1021. One purpose of the work was to calculate and experimentally verify steady-state and dynamic design data for two journal bearings, namely, the tilting-pad and full floating ring bearings. The design data cover operation in both laminar and turbulent flow regimes with incompressible lubricants. A second purpose was to investigate the fundamentals of Taylor vortex flow and turbulence in concentric and eccentric annuli.

In previous work, done under NASA contract NASw-771, the steady-state and dynamic properties of basic bearing elements, the partial arc, and the full cylindrical bearing were calculated and compared with experimental measurements in laminar and turbulent flow regimes (NASA Contractor Report CR-54034). Also, investigation of the fundamentals of vortex and turbulence in concentric annuli was begun. This work provided the foundation for the work now being reported on NASA Contract NASw-1021.

The work reported herein was done under the technical management of Joseph P. Joyce, Space Power Systems Division, NASA-Lewis Research Center, with William J. Anderson, Fluid System Components Division, NASA-Lewis Research Center, as research consultant. The report was originally issued as MTI Report 65TR32, June 1965.

ABSTRACT

Calculated data on steady-state load capacity and friction torque and dynamic stiffness and damping coefficients are given for the tilting-pad journal bearing for laminar and turbulent flow conditions for Reynolds Numbers up to 12,000. Design curves are given for the four-pad, 80-degree pad arc, bearing for four values of preload coefficient. Some tabulated data are given for the three-pad, 100-degree pad arc bearing. The design data are verified and supplemented by experimental measurements of both steady-state and dynamic properites. Correlation between measured and calculated performance is good so it is concluded that the data are effective for design analysis purposes.

TABLE OF CONTENTS

STEADY-STATE AND DYNAMIC PROPERTIES OF JOURNAL BEARINGS IN LAMINAR AND SUPERLAMINAR FLOW REGIMES

I. Tilting-Pad Bearings

By F. K. Orcutt
Mechanical Technology Incorporated

SUMMARY

The tilting-pad journal bearing is an outstanding candidate for application to high-speed rotary machinery lubricated by low kinematic viscosity fluids such as the alkali metals because of its unexcelled dynamic characteristics including stability. High speeds and low kinematic viscosity lubricants mean that bearings for such applications will operate in the turbulent regime. The same characteristics mean that the dynamics of the rotor-bearing system including critical speeds, response to dynamic load, and stability will be of critical importance.

This report presents theoretical steady-state and dynamic design data for the three and four pad tilting-pad bearings with L/D = 1. The data are presented in tabular and design chart form for laminar and turbulent flow. The design data are verified and supplemented by experimental measurements for the four-pad bearing including steady-state and dynamic loads and operation from laminar flow to Reynolds numbers up to 12,000. The calculated static load capacity and friction torque agree with the measurements within about 10 percent. The theoretical dynamic stiffness and damping coefficients are verified by comparing the measured motion of the shaft in response to dynamic load with the calculated response obtained by a rotor-dynamic analysis using the calculated bearing coefficients. Correlation between measured and calculated dynamic performance has been good though not as close as the agreement for steady-state conditions owing to the complexity of the system and the many factors other than the test bearing which influence the results. In most instances, measured and calculated response to dynamic load agree within 20 percent. A theoretical criterion for bearing stability based on the ability of the pads to follow the shaft motions closely is also presented and tested. Again experiment and theory are in good agreement.

This work has confirmed the expected advantages of the tilting-pad bearing for space power machinery. It has also confirmed the expectation of relatively high power loss for these bearings under conditions resulting in highly turbulent lubricant films.

INTRODUCTION

This report presents design data with experimental verification for the tilting-pad journal bearing operating in the laminar and superlaminar flow regimes. A potential application for the data which are given would be in the design of bearings and rotor systems for high-speed machines lubricated by liquid metals.

Liquid metals have very low values of kinematic viscosity compared with oils and most other fluids that have been used as bearing lubricants. Because of this, liquid-metal lubricated bearings for high-speed rotors generally operate in the turbulent regime. The static loads are low and the speeds are high in the type of machinery under discussion, so the dynamic characteristics of the rotor-bearing system including critical speeds, response to dynamic load and stability are the primary matters for concern. The difficulty of obtaining good dynamic characteristics of the rotor-bearing system is increased with liquid-metal lubricants because, with their low viscosities, the bearing stiffness and damping are much lower than would be the case for oil lubricants. Because the tilting-pad bearing can be designed to have: (a) favorable dynamic characteristics, (b) inherent stability and, (c) a degree of self-alignment capability, it is a primary candidate for support of high-speed rotors, lubricated with low viscosity fluids such as liquid metals.

DESCRIPTION OF THE TILTING-PAD BEARING

The tilting-pad journal bearing consists of a set of pads which are individually pivoted, as shown schematically in Fig. 1. The geometrical parameters that define the bearings are:

(a) Bearing diameter (D)

(b) Number of Pads

(c) Angular extent of the pads (β)

(d) Slenderness ratio ($\frac{L}{D}$)

(e) Pad clearance ratio ($\frac{C}{R}$)

(f) Pivot location ($\frac{\theta_P}{\beta}$)

(g) Pad mass and inertia

(h) Geometrical preload coefficient (m)

The parameters which are peculiar to this type of bearing are f, g and h, and these are discussed briefly below.

Pivot Location

Each pad of the bearing is pivoted individually to permit one or two degrees of freedom. With proper design, the friction torque in the pivot is negligibly small in comparison with the moment induced in the fluid film when the resultant of the fluid film forces does not pass through the pivot. Each bearing pad will, therefore, assume an inclination such that the resultant of the fluid film forces passes through its pivot point. Thus, the location of the pivot point is critical since it governs the inclination that each pad will assume, hence the magnitude of the hydrodynamic pressures that are generated in the fluid film. Where the bearing has to be designed for either direction of rotation, a centrally located pviot ($\theta_p/\beta = 0.5$) is generally desirable.* Where the bearing is subject to only one direction of rotation, increased stiffness can be achieved at low eccentricity ratios by locating the pivot point a little after the midplane of the pads (ref. 15). The individual pad load capacity is nearly constant from $\theta_p/\beta = 0.5$ to $\theta_p/\beta = 0.6$, however, the latter case results in much larger pad attitude angles, exceeding 90 degrees, at low pad eccentricities. This means that in bearings with low preload operating at low eccentricity, the top pads are active and contribute to the bearing stiffness when θ_p/β is greater than 0.5.

Pad Mass and Inertia

Proper functioning of tilting-pad bearings, under dynamic loads is predicated upon the pads being able to "track" the orbits of the journal. As the journal center moves along an orbit, the individual pads of the bearing must vary their inclinations, such that the vector sum of the fluid-film forces generated in the pads is always equal and opposite to the instantaneous journal load. If this condition is not satisfied, the tilting-pad bearing loses much of its advantage. It will approach in performance the fixed pad bearing and will become subject to a low threshold of instability. The ability of the tilting-pad bearing to track journal motions can be analyzed in terms of the inertia of the individual pads and the stiffness and damping of their fluid films. The analysis yields equations which define: (a) the magnficiation factor (i.e., the ratio of the amplitudes of motion of the pads to those of the journal), and (b) the phase angle between these motions – in terms of the mass of the pads and the stiffness and damping coefficients of the fluid film. The value of the pad mass, at which the phase angle is 90^{o} (compared to 0^{o} if the pads have zero mass) is called the critical mass of the pads (M_{crit}). In order to assure satisfactory tracking of the journal orbits, the pads should be designed such that their mass is a small fraction of the critical mass. In practice, it is found that satisfactory tracking is achieved if the pad mass is less than one-half the critical pad mass. The critical pad mass has been computed and plotted in the design charts included in this report, as a function of Sommerfeld Number and Reynolds number to facilitate design calculations.

---

* We are concerned here with journal bearing pads which are circular arcs. Such pads can generate hydrodynamic pressures, with centrally located pivots. The situation is quite different in the case of thrust bearings, where it can be shown that perfectly flat, centrally pivoted pads cannot generate hydrodynamic pressures. The load capacity exhibited by centrally pivoted thrust bearing pads is almost entirely due to the fact that the pads "crown" under load, as a result of (a) the distributed load on the active faces and the point (or line support) on the back faces of the pads, and (b) the thermal gradients across the pads caused by heat generated by fluid shear on the active faces of the pads.

Geometrical Preload Coefficient

Geometrical preloading is used in order to achieve:

(a) High bearing stiffness, even with zero net load on the shaft.

(b) Positive fluid film pressures acting on all the bearing pads (even those located in the part of the bearing away from the direction of load). Thus bearing stability is improved.

Geometrical preloading is achieved by assembling the pads such that their centers of curvature, with zero inclinations, form a circle of radius "a" about the center of the bearing. Figures 2A and 2B show, respectively, the geometrical arrangement of the pads without and with geometrical preload. Let:

R_P = Radius of curvature of the pads as machined

R_S = Radius of shaft as machined

a = Radius of preload circle

$C_P=R_P-R_S$ = Radial clearance of the pads (machined clearance)

In the preloaded case, "the bearing radius" is now defined as:

$$R_B = R_P - a$$

The "bearing radial clearance" (i.e., running clearance over the pivots at zero load) is defined as:

$$C_B = R_B - R_S = R_P - a - R_S$$

From the definition of C_P and the equation above, it is seen that

$$a = C_P - C_B$$

The preload coefficient is defined as:

$$m = 1 - \frac{C_B}{C_P} = 1 - \frac{(R_P - a - R_S)}{R_P - R_S} = \frac{a}{R_P - R_S}$$

Under load, the shaft center will move away from the bearing center. Also, each pad will incline such that the resultant of the fluid film pressures passes through the pivot point. Its center of curvature will, therefore, move along an arc of a circle, whose center is the pivot point.

Let e_B = distance between the shaft center and the bearing center under a given load on the shaft (bearing eccentricity).

Let e_P = distance between the shaft center and the center of curvature of a pad, under same load on the shaft (pad eccentricity).

We then define two eccentricity ratios as follows:

Pad eccentricity ratio is:

$$\epsilon_P = \frac{e_P}{C_P}$$

and bearing eccentricity ratio is:

$$\epsilon_B = \frac{e_B}{C_B}$$

Test Bearing Design

The numerous variables in the design of a tilting-pad journal bearing can be grouped into those describing the design of the individual pad; those which determine how the pads are assembled together into the bearing; and those which describe the pivot. The pad design variables and the values chosen for the test bearing include:

(a) Clearance ratio (C/R) - 3×10^{-3} in./in.

(b) Slenderness ratio (L/D) - 1.0

(c) Arc length (β) - 80 degrees

(d) Position of the pivot along the pad arc (which will determine the direction of the resultant of the fluid film forces acting on the pad since this must pass through the pivot) - 44 degrees from leading edge, or 0.55 of the arc length.

The variables describing the assembly of pads into the bearing are:

(a) The number of pads - 4

(b) The preload coefficient, m - adjustable for $0 < m < 1$.

The pivot design variables depend on the exact pivot configuration chosen, but for the sphere in contact with an internal cylindrical surface, as is used here, they are:

(a) Material modulus of elasticity - 30×10^6 psi for hardened tool steel

(b) Radius of the sphere - 0.625 inch

(c) Radius of the cylinder - 0.655 inch

The position of the pivots was chosen as it is approximately the optimum position from the standpoint of load capacity for a bearing using incompressible lubricant. The principal guidelines in planning the pivot design were to hold the Hertzian contact stress below 200,000 psi while minimizing relative sliding of the contacting surfaces. The elastic stiffness of the pivot contacts has been calculated. The stiffness varies as the 2/3 power of the pad load and is 1.3×10^6 lb/in. at 500 lb load. This is within an order of magnitude of the expected fluid-film stiffness; therefore, pivot deflection will be a factor to be considered both with respect to the overall bearing stiffness and because of the tendency to reduce bearing preload at high values of static load. The test bearing pivots are about as stiff as they can reasonably be if the self-aligning feature of the bearing is to be retained (a cylinder contacting a cylinder would be stiffer but would pivot in one plane only). Therefore, this is a property of the bearing which is encountered in turbomachinery as well as in the test bearing and it will be factored into the calculations that are made for comparison of theoretical and test data. It is planned to compare the experimental and theoretical results in this program by using the calculated bearing characteristics in a rotor-bearing analysis of the test machine and comparing calculated and measured response orbits and critical speeds. Pivot stiffnesses will be included in the pedestal characteristics in the calculations just as we would expect to do in a design analysis.

SUPERLAMINAR FLOW IN BEARING FILMS

There are two distinct modes of superlaminar flow that can occur in journal bearing films. The first of these is vortex flow and the second is fully developed turbulence.

The transition to vortex flow in the annular space between two concentric cylinders, with the inner cylinder rotating and the outer one stationary, occurs at a critical value of the Reynolds Number given by:

$$Re_{crit} = \left(\frac{2\pi RNC}{\nu}\right)_{crit} = 41.1\sqrt{\frac{R}{C}} \tag{1}$$

where

- Re = Reynolds Number
- R = Bearing radius
- N = Speed of rotation of the inner cylinder (shaft speed), R.P.S.
- C = Radial clearance, inches
- ν = Kinematic viscosity, in.^{2}/sec

This criterion for onset of vortex flow was determined both analytically and experimentally by G. I. Taylor (ref. 1). It has been found experimentally to apply, approximately, for lightly loaded (and, hence, nearly concentric) journal bearings (ref. 2 and 3). It also applies qualitatively to eccentric journal bearings, except that the transition speed is then modified by the pressure gradient effects (ref. 4).

At the critical Reynolds Number, vortices are generated in the annular space between the concentric cylinders, due to the radial centrifugal pressure gradient. This flow is free from the random fluctuation that characterize true turbulence, however, it is accompanied by a measurable increase in the drag loss, analogous to that encountered in turbulent flow. Fully developed turbulence has been found experimentally, to set in when the Reynolds Number ($Re = 2\pi RNC/\nu$) reaches a value of about 1000 to 1500, for the case of rotating inner cylinder and a stationary outer cylinder.

Equation (1) shows that the onset of Taylor vortices will occur in journal bearings at values of the Reynolds Number that range from about 750 for a clearance ratio (C/R) of 0.003 inches per inch, to about 1300 for a clearance ratio of 0.001 inches per inch. Thus, except in cases where bearings with excessively large clearance ratios are used, the region where Taylor vortices occur without developed turbulence in the fluid film is quite small. All the turbulent lubrication analysis,which is the basis of the calculated bearing data which will be presented, presumes fully developed turbulence in the fluid film.

In classical analysis of fluid film bearings, it is assumed that the lubricant flow in the clearance spaces is laminar. This is generally true of conventional bearings which have small clearance (of the order of 10^{-3} inches) and which are lubricated with hydrocarbon oils whose kinematic viscosity is high (of the order of 10^{-2} to 10^{-1} in.^{2}/sec). The situation is quite different in the case of high-speed, rotating machinery lubricated with liquid metals or other low kinematic viscosity lubricants. The combination of low kinematic viscosity and high operating speed results in superlaminar flow in the bearing film. This is illustrated in Table I, which shows the speed at which transition to turbulence should occur for a lightly loaded 4.0 inch diameter bearing. The onset of turbulence is taken to occur when the fluid film Reynolds Number reaches 1500.

TABLE I

COMPARISON OF ESTIMATED SPEEDS FOR
ONSET OF TURBULENCE USING VARIOUS LUBRICANTS[a,b]

Lubricant	Kinematic Viscosity ($in.^2$/sec)	Speed for Onset of Developed Turbulence, rpm
Water (80F)	1.33×10^{-3}	1,850
SAE 10 Oil (150F)	2.16×10^{-2}	30,100
Potassium (1200F)	3.31×10^{-4}	460
Sodium (1200F)	3.86×10^{-4}	536
Silicone Oil (0.65 cs)	1.01×10^{-3}	1,410
Silicone Oil (5.0 cs)	7.75×10^{-3}	10,900
Air (80F and 15 psia)	2.52×10^{-2}	35,200
Mercury (400F)	1.2×10^{-4}	168

[a]Bearing diameter = 4.0 inches, C/R = 3.0×10^{-3}

[b]These values are computed for concentric, plain journal bearings

PART I

ANALYSIS AND PRESENTATION OF DESIGN DATA

The theoretical analysis of the tilting-pad bearing for laminar and turbulent flow is summarized. Details are given in Appendices. Design data graphs for the four-pad bearing with L/D = 1 are presented. Tabulated data for the three-pad bearing are given in Appendix C.

THEORETICAL ANALYSIS OF THE TILTING-PAD BEARING IN THE TURBULENT FLOW REGIME

Broadly speaking, the theoretical analysis for the tilting-pad bearing is constructed by summation of the effects of the individual pads which are determined from the lubrication theory for partial-arc journal bearings. There are additional factors and complications to be considered as will be shown, but this is the essence of the procedure which is followed. The stepwise development of the tilting-pad bearing theory, beginning with the linearized turbulent flow theory for the individual fixed partial arc, then to the individual tilting pad, and finally to the composite bearing, will be described briefly in the following sections. The analysis and the numerical solution of the resulting equations are described in more detail in the Appendices.

Linearized Turbulent Lubrication Theory for a Partial-Arc Bearing

The development of the linearized, turbulent-flow lubrication theory based on the eddy diffusivity concept was described by Ng and Pan in ref. 5. The mathematical analysis leading to the theory was given also in Appendix to ref. 6 and the procedure for numerical integration of the turbulent lubrication equation for calculating static and dynamic load characteristics of a single-bearing element was presented in ref. 7.

In the linearized version of the turbulent lubrication theory, the governing differential equation is linearized with respect to the pressure gradients. The end result is a modified form of the Reynolds Equation which, for the incompressible journal bearing, can be written as follows:

$$\frac{1}{R^2}\frac{\partial}{\partial\theta}\left(\frac{h^3}{\mu}G_\theta\frac{\partial P}{\partial\theta}\right)+\frac{\partial}{\partial z}\left(\frac{h^3}{\mu}G_z\frac{\partial P}{\partial z}\right)=\left(\frac{V}{2R}\frac{\partial}{\partial\theta}+\frac{\partial}{\partial t}\right)h$$

where G_θ and G_z are functions of the local Reynolds Number, $\frac{Vh}{\nu}$. Under laminar flow conditions (small values of the Reynolds Number), the functions G_θ and G_z approach the value $\frac{1}{12}$, so that Equation 1 reduces to the conventional Reynolds Equation. More recently, a non-linear version of the theory has been completed (ref. 8). Comparison of results from the two versions has shown that the linearized theory can be used satisfactorily for self-acting bearings. In ref. 5, good correlation between the results of the linearized theory and experimental data for 360-degree cylindrical and 60-degree partial-arc bearings is shown for static properties. Earlier work in this program (ref. 7) showed good correlation between theory and experiment for both static and dynamic properties for the 100-degree partial-arc bearing.

The solution of the linearized, turbulent-flow lubrication theory has been extended to calculate the frictional loss and lubricant flow as well as the static and dynamic load characteristics of the individual pad. The numerical solution is discussed in more detail in Appendix A.

Dynamic Analysis of the Partial-Arc Bearing

The dynamic load analysis of the individual partial-arc bearing is based on an examination of small motions of the journal center about its equilibrium position. The analysis is limited to small motions because the resultant of the hydrodynamic fluid-film forces is a non-linear function of the displacement, attitude angle, and velocity of the journal center. Therefore, the agreement between the analysis and the behavior of practical rotor systems depends, in part, on how closely the relationship between the gradient of the bearing film force and the shaft center displacement approaches linearity in the region of interest. In most hydrodynamic journal bearings, this relationship is reasonably linear for values of eccentricity ratio up to about 0.8. Above this eccentricity ratio, the curvature of the force-displacement curve increases sharply. Ordinarily, design loads for high-speed rotating machinery result in equilibrium eccentricity ratios well within the useful range of the dynamic analysis.

In the dynamic analysis, the fluid-film force resultant is reduced to a set of spring and damping force coefficients. The values of these force coefficients are the gradients of the force-displacement and force-velocity curves at the equilibrium position of the journal center. In principle, this system is analogous to a mechanical system of springs and dashpots supporting the shaft. However, there are significant differences:

(1) The bearing film force versus displacement and force versus velocity relationships are non-linear, so the spring and damping coefficients are not constants but vary continuously with the equilibrium position of the shaft center. In the case of turbulent flow bearings, the coefficients change also with Reynolds Number.

(2) There is a cross-coupling effect, arising from the fact that the resultant of the film forces caused by a displacement, or velocity, of the shaft center is not co-linear with the displacement or velocity. Thus, if the shaft is displaced, or if a velocity is imparted to it, the resulting change in fluid-film force will have components both along the direction of displacement, or velocity, and normal to it.

If the dynamic fluid-film force and the shaft displacement and velocity are resolved into components along x and y coordinates, with the steady-state load (F_o) directed along the x axis, we have:

$$F_x - F_o = - K_{xx}x - B_{xx}\dot{x} - K_{xy}y - B_{xy}\dot{y}$$

$$F_y = - K_{yx}x - B_{yx}\dot{x} - K_{yy}y - B_{yy}\dot{y}$$

where the first subscript defines the direction of force and the second subscript defines the direction of the displacement or velocity. The eight coefficients have been calculated for the 80 degree, arc bearing in the manner described in Appendix B for Reynolds Numbers up to 12,000 and for equilibrium eccentricity ratios from 0.01 to 0.99.

Dynamic Analysis of the Tilting Pad

The small motions of the shaft center caused by dynamic load will cause the individual tilting pad to oscillate about its pivot point. Under certain conditions of bearing operation and pad design, this oscillation will approach a resonance. When this happens, the amplitude of oscillation becomes very large. For typical pad designs, resonance will occur when the pad eccentricity ratio is small and, therefore, the load on that particular pad will be light. In addition, the effects of fluid-film damping, which will be large for small eccentricity, and of the mass inertia of the pad about its pivot will provide some support at the pad resonance condition. It may be that the most serious effects of pad resonance are on the pivots where fretting may be brought on by large oscillation amplitudes at high frequency. A comparatively large bearing preload should help to avoid pad resonance by avoiding low eccentricity ratios, and low film stiffness, for the pads on the side of the bearing away from the static load direction.

The analysis to determine the critical mass of the pad for resonance is given in Appendix B. This analysis can be used to calculate the dimensionless pad critical mass as a function of bearing Sommerfeld Number for different values of Reynolds Number, once the pad fluid film dynamic characteristics are determined from the turbulent lubrication analysis for the fixed pad. This has been done and the results will be presented later in this report. They can be used in bearing design to assure proper tracking and to avoid having a pad resonance at or near the normal machine operating conditions.

Analysis of the Composite Tilting-Pad Bearing

The static and dynamic load characteristics of the composite, tilting-pad bearing are determined by summation of the effects of the individual pads. The procedure for doing this is long and tedious. Briefly, it is required that the total force component in the y-direction (normal to the load line) summed over all pads must be zero. For a given eccentricity ratio and bearing preload, several values of attitude angle are assumed. The individual pad forces resulting from each of these assumed journal positions are determined from the data for a single pad. The summation of the pad forces for each assumed attitude angle are plotted and, by interpolation, the attitude angle where the summation of forces in the y-direction is zero is determined. The individual pad forces can then be analyzed again for the correct attitude angle. The procedure can be simplified a great deal if the pad pivots are located symmetrically about the x-axis, or static load line, and if pad inertia is neglected. In this event, the attitude angle will always be zero and, moreover, since the force and displacement vectors are now co-linear, the cross-coupling spring and damping coefficients vanish. Furthermore, for the four-pad bearing with the load line between the pivots, the dynamic coefficients in the x- and y-directions will be identical because of symmetry, and response of the shaft to a rotating load will always be a circle.

The analysis for dynamic characteristics of the composite tilting-pad bearing is given in more detail in Appendix B.

CALCULATED STATIC AND DYNAMIC CHARACTERISTICS FOR THE FOUR-PAD BEARING

In order to verify the analysis and the computer programs for calculating bearing design data, static load results were calculated for laminar flow for comparison with Raimondi and Boyd's results (ref. 9) for partial-arc bearings with laminar flow. The calculated values (in parenthesis) are compared with Raimondi and Boyd's results in the table below. The number of mesh points for the finite difference solution of the Reynolds equation is given for each case.

ϵ	ϕ	$\frac{R}{C}f$	$\frac{Q}{RCNL}$	Q_s/Q	S
	L/D = 1.0 60^o Arc (mesh: circumferential-16, axial -14)				
0.1	67.92(65.35)	29.1(28.86)	3.07(3.05)	0.0267(0.0212)	8.52 (8.59)
0.8	18.33(18.26)	1.42(1.39)	0.883(0.836)	0.200(0.159)	0.101(0.102)
	L/D = 1.0 120^o Arc (mesh: circumferential-16, axial -14)				
0.1	72.43(71.99)	14.5(14.20)	3.20 (3.19)	0.0876(0.0777)	2.14 (2.135)
0.8	27.42(27.28)	1.27(1.195)	1.57 (1.428)	0.535 (0.484)	0.0531(0.0529)
	L/D = 1.0 Full Journal (mesh: circumferential-20, axial -14)				
0.1	79.5 (83.73)	26.4(24.8)	3.37 (3.39)	0.150 (0.144)	1.33 (1.30)
0.8	36.24(36.13)	1.7(1.38)	4.62 (4.78)	0.842 (0.820)	0.0446(0.043)

The agreement seems quite satisfactory.

Calculations of static load capacity, dynamic coefficients, friction torque and flow through the bearing have been made for a four-pad bearing with the static load line directed midway between pivots. Consistent with the test bearing design, the pad arc-length is 80 degrees and the pivot is located at 0.55 of the arc length (44 degrees) from the leading edge.

Static load capacity results are given in Figs. 3 through 6 for preload coefficients, 0, 0.3, 0.5 and 0.7 respectively. The results are presented as Sommerfeld Number plotted against eccentricity ratio for various values of Reynolds Numbers up to 16,000.

The locus of attitude angle versus eccentricity ratio for the individual pad with 0.55 pivot position is given in Fig. 7 for several Reynolds Numbers up to 16,000. The effect of Reynolds Number on the attitude-angle eccentricity relationship is quite small after the transition to turbulence has taken place. The attitude angle versus eccentricity ratio locus for the composite bearing is simply the direction of the load line, i.e., $\phi_o = 0$ for all ϵ, because of symmetrical positioning of the pivots about that line.

PART II

EXPERIMENTAL VERIFICATION OF DESIGN DATA

The dynamic load bearing apparatus and instrumentation are described. The steady-state and dynamic performance of the four-pad bearing with $L/D = 1$ and $m = 0$ and 0.5 are compared with the theoretical design data.

THE DYNAMIC LOAD BEARING APPARATUS

Mechanical Features

This apparatus was designed for the purpose of experimental determination of the static and dynamic properties of journal bearings operating in the laminar or turbulent regimes. The apparatus capabilities include the following:

Bearing Diameter	4.0 inches
Bearing L/D	Up to 1-1/2
Speed	2000 to 11,500 rpm
Static Load	0 to 1000 lb
Dynamic Load	Magnitude depends on speed; load rotational frequency from 2000 to 24,000 rpm in either direction; driven independently of shaft rotation.

The arrangement of the principal mechanical components of the apparatus is shown schematically in Fig. 28. Figure 29 illustrates the test bearing housing with the tilting-pad bearing in place. A duplex pair of angular-contact support bearings are at one end of the shaft with the test bearing at the other end. The span between bearings is 40 inches. Static and rotating loads are applied at the test bearing end of the shaft, outboard from the test bearing. Static load is applied through a self-aligning, double-row ball bearing by a cable to which tension is applied by a large, low spring rate (125 lb/in.) coil spring. An upward load, to counterbalance all or part of the shaft weight, can be applied to the same bearing by a spring-type load cell mounted above the shaft. The shaft is shown with a fixed unbalance weight as the rotating load but it is also possible to apply rotating load at any frequency, from 2000 to 24,000 rpm, or in either direction of rotation, independently of shaft rotation. This is done by mounting a double-row ball bearing on the end of the shaft in place of the disk which is shown in Fig. 28. Unbalance weight is then attached to the housing which is mounted on the outer race of the ball bearing and the outer race-housing assembly is driven by a small universal electric motor through a flexible-disk coupling.

The shaft is of steel tubing (three inch I.D.) with shrink-fitted end sections and is coated with a tungsten carbide cermet in the test bearing area. Test bearing, support bearing, and loader bearing diameters are all concentric within 0.0002 inch TIR. The shaft was balanced first in a balancing machine and then in place at operating speeds to approximately 0.08 inch-ounce unbalance. This represents a displacement of the mass center from the geometric center of about 50 microinches. There is very little restraint to shaft motion within a 10 mil clearance radius at the test bearing from the support bearings or the drive coupling. The change in upward force required to lift the shaft from bottom to top of such a clearance circle is 1.5 lbs.

Considerable care was taken in the design and fabrication of the apparatus to assure close alignment between test and support bearings. Alignment is checked on each assembly by measuring the squareness of the test-bearing housing face with the shaft axis. The housing face is known to be square with the housing bore within 0.0005 inch on a four-inch radius. There has been no difficulty in maintaining alignment within 0.0003 over the bearing length. The tilting-pad test bearing self-aligning feature is capable of accepting misalignments much greater than this without measurable effect on performance.

The 7-1/2 hp variable-speed electric drive is coupled to the support bearing end of the shaft by a dynamically balanced, flexible-disk coupling.

Two lubricants were used in these experiments: a 5.0 cs (77 F) silicone oil with viscosity-temperature coefficient $\left(1 - \frac{\text{viscosity at 210 F}}{\text{viscosity at 100 F}}\right)$ of 0.55 for laminar flow and low Reynolds Number data, and a 0.65 cs (77 F) silicone oil with viscosity-temperature coefficient of 0.31 for high Reynolds Number data. Oil is supplied to the test bearing at controlled temperature by a variable-delivery pump. Lubricant returns to the sump by an overflow line which taps into the top of the test bearing housing, or by scavenge pumps which drain the cavities outside the clearance seals at either end of the test bearing housing. During operation, the bearing is submerged in lubricant at atmospheric pressure.

Instrumentation

The following variables must be measured for experimental data or control purposes:

(a) Dynamic motion of the shaft axis at the test bearing and support bearing locations.

(b) Steady-state locus of the shaft axis with respect to the test bearing center.

(c) Dynamic motions of one bearing pad about its pitch and roll axes.

(d) Shaft speed.

(e) Static load on test bearing.

(f) Test bearing torque.

(g) Test bearing temperature.

The steady-state locus and dynamic motion of the shaft axis are measured by eddy current proximity sensors. (Bently Nevada Corp.) At each plane of measurement there are two sensors; one to measure position and motion along the vertical axis and one for the horizontal axis. There are two planes of measurement at the test bearing location (Fig. 29); one at either end of the housing just outside the seal and scavenging rings. The outputs of the two vertical probes, and of the two horizontal probes,at this location are averaged by adding them together using summing amplifiers. This was done to minimize the effects of any shaft bending. Readout of the shaft locus measurements was by oscilloscope using x-y axis presentation. With this arrangement, the locus of the shaft center is represented as a point whose motion and position within the bearing clearance circle is easily seen. Variable electronic filters set for band-pass operation were used when measuring the response of the shaft to dynamic load. A low-pass operation was needed to eliminate high-frequency fluctuations from the signal caused by magnetic inhomogeneity of the shaft material or stray magnetic fields in the shaft. The high-pass operation eliminates fluctuations due to small amplitude fractional-frequency whirl and is also needed to offset the phase shift in the signal caused by the low-pass operation.

The eddy current proximity sensors are not influenced by the presence, or absence, of silicone oil lubricant in the gap between probe tip and shaft surface. This would not be true of a lubricant which is not a good dielectric. They do experience zero drift with temperature changes. This was not a problem in these experiments because the probes were in an ambient environment outside the test bearing housing. During the experiments, frequent checks for zero drift were made by running with zero load so the shaft center coincided with the bearing center.

In connection with the measurements of shaft response to dynamic load, it is necessary to mark or identify the instant when the rotating load is directed along the x axis and again when it is directed along the y axis. This is done by magnetic pickups placed on each of these axes to sense the passage of the unbalance weight.

Eddy current proximity sensors were used also to measure motions of one pad about its pivot. This was done to determine whether the pads were following the shaft motion in response to dynamic load. Two probes were located at the ends of the pad along the line passing through the pivot and parallel to the shaft axis to measure pad roll. These are the probes shown in Fig. 29. The output voltages of these two probes were of opposite polarity so that when the outputs are summed, the combined signal is sensitive only to roll motions and not to other movements such as those caused by pivot deflection. A second pair of probes was mounted on the roll axis at the leading and trailing edges of the pad to measure pad pitch. The instrumented pad was located on the lower side of the bearing ahead of the load line during the experiments.

Torque was measured by a strain gage rotary torquemeter (Lewbow Associates Inc. Model 121) coupled into the drive train between the drive motor and the shaft end. Rated capacity of the torquemeter is 200 inch-pound. Initially, a commercial null-balance indicator was used for readout and excitation. However, it was found that dynamic fluctuations in torque were not being averaged out properly with this arrangement. An alternate arrangement incorporating mercury cells was used for excitation, and the output was fed into an electronic filter set for low-pass operation with a cut-off frequency of several cycles-per-second. After filtering, the output was displayed on an oscilloscope. This arrangement gave high sensitivity and extremely good stability and reproducibility of results. The range of variation in torque for fixed operating conditions for periods of operation of as much as 30 minutes was typically 0.3 inch-pound with mean torque values of 10 to 40 inch-pounds.

The total torque measured by the torquemeter includes losses in the support and loader bearings, in the clearance seals, and from "windage" for the portion of the shaft which is inside the test bearing housing but which is not enveloped by the test bearing. These superfluous drag losses were determined experimentally by making the following modifications to the apparatus:

(1) An externally-pressurized, gas-lubricated bearing was substituted for the test bearing to establish support and loader bearing losses for a range of speeds. The gas bearing drag was calculated using Petroff's equation for concentric cylinders and this was subtracted from the total to obtain the correction torques shown in Fig. 30. The effect of load is small and not entirely consistent, so a mean value was used independent of load.

(2) Housing windage and seal ring losses were determined by experiments in which the test bearing end of the shaft was supported by the ball bearing which is normally the static load bearing. A special housing was made which was the same as the test bearing housing except it was thinner by the four-inch section normally occupied by the test bearing. The shaft was run with this housing and the seal rings in place, and with lubricant circulating, to obtain the seal ring and housing windage drag. The results are shown in Fig. 31. An attempt was made to calculate these losses using the following two approaches: (1) extrapolation of the data on drag between concentric cylinders (ref. 3) to the much higher C/R and Re of the bearing housing, and (2) using data on windage of a rotating cylinder in an infinite body of fluid (ref. 10). Neither approach was accurate which is not surprising, considering the gross simplifications and extrapolations which were involved. As might be expected, the experimental losses are greater than the calculated results for concentric cylinders and lower than those calculated from windage data.

The shaft speed is measured by means of a magnetic pickup which senses the passage of a set screw protruding slightly from the shaft surface. The output of the pickup is amplified and supplied to a frequency meter. Static load is measured by a strain gage load cell to which the cable which applies the load is connected.

Bearing temperature is measured by a thermocouple welded to the trailing edge of one of the lower pads flush with the bearing surface. The measured bearing temperature is used to establish lubricant viscosity for determination of Sommerfeld and Reynolds Numbers.

The dynamic bearing characteristics are plotted as dimensionless stiffness ($\frac{C}{W}K$) or damping ($\frac{C}{W}\omega B$) versus Sommerfeld Number for the various values of Reynolds numbers up to 16,000 in Figs. 8 through 15 for m = 0, 0.3, 0.5, and 0.7. There is only one spring and one damping coefficient to describe the bearing dynamic characteristics completely because of symmetry of the pivots with respect to both x- and y- axis and because of the assumption of inertialess pads.

Curves of dimensionless friction torque ($\frac{T}{C_P W}$) versus Sommerfeld Number are given in Figs. 16 through 19.

Dimensionless flow versus Sommerfeld Number is plotted in Figs. 20 through 23 for the different preloads. This is the hydrodynamic flow into the entrance of the individual bearing pad. The temperature rise across the pad can be estimated closely from the calculated flow and torque.

Finally, the dimensionless critical mass of the pad is given as a function of Sommerfeld Number in Figs. 24 through 27. There are separate values of critical mass for the pads which are on the side away from the load and for those on the loaded side. Except for the cases of lower preload ($m \leq 0.3$), the smaller of the two values are plotted. For the low preload cases, the top pads will nearly always be completely unloaded so the critical mass for the bottom pad is plotted.

MEASURED STATIC LOAD PROPERTIES OF THE FOUR-PAD TILTING-PAD BEARING

The static load capacity and friction torque of the tilting-pad bearing have been measured for Reynolds Numbers from laminar to 12,000 and for two values of preload coefficient, 0 and 0.5. The combination of speed and oil viscosity which were used to obtain the Reynolds Numbers used in the experiments are given in Table II.

TABLE II

Reynolds Number $\frac{2\pi RNC_P \rho}{\mu}$	Shaft Speed rpm	Oil Viscosity centistokes
320 (Laminar)	2020	5.0
1000	4800	3.9 (100 F)
3000	2400	0.65
5000	4000	0.65
8000	6400	0.60 (91 F)
12000	8250	0.50 (132 F)

For each Reynolds Number, the Sommerfeld Number, $\mu NLD/W\ (R/C_P)^2$, was varied by changing the static load applied to the shaft. In all cases, the static load direction was midway between the pivots of the loaded pads.

In high-speed machines, especially those with hollow shafts, reduction in bearing clearance because of centrifugal growth of the shaft can have a significant effect on bearing performance. The centrifugal growth of the test apparatus shaft was calculated and it was found that there was a reduction in pad clearance (C_P = 0.006 inches) of 2.8, 7.1, and 11.8 percent at 4000, 6400 and 8250 rpm respectively. The effect on performance was significant at 6400 rpm and higher so corrections to C_P were made to all data for 6400 and 8250 rpm.

Static Load Capacity

Experimental static load capacity data for the tilting-pad bearing are plotted along with the corresponding theoretical results in Figs. 32 and 33 for m = 0 and Figs. 34 and 35 for m = 0.5. The notation which is used for eccentricity ratio, $\epsilon_B(1-m)$, reduces to the eccentricity of the shaft center divided by the machined clearance of the pad, C_P. Thus, a displacement of the shaft center which is equal to the clearance at the pivots represents an eccentricity ratio of 1.0 for m = 0 and 0.5 for m = 0.5. Since the load direction is between pivots, it is possible to have eccentricities greater than the pivot clearance without contact between shaft and pads.

The experimental measurements and the theoretical results are in good agreement. This is important for the obvious reason that the bearing designer wants to know what the eccentricity ratio and minimum film thickness will be for his operating conditions. It is important also because good agreement between calculated and actual steady state position of the shaft center in the bearing clearance is essential to accurately specify the dynamic properties of the bearing.

With the load direction midway between pivots, the shaft attitude angle should be zero for all values of eccentricity ratio. This expectation was confirmed by the measurements.

Friction Torque

Measured and calculated friction torque results are compared in dimensionless form in Figs. 36 and 37 for $m = 0$ and Figs. 38 and 39 for $m = 0.5$. The experimental data are obtained from the total measured torque minus corrections for support and loader bearing drag and for seal ring and housing windage losses. The determination of these corrections was described in the section on instrumentation for torque measurement.

Again, the agreement between measured and calculated results is good. In most cases, the measured torques are slightly higher than the calculated values. This may reflect the drag from the narrow gaps between the pads which are not considered in the analysis. Alternatively, it may be the result of inaccuracy in the determination of housing and seal losses stemming from inexactitude of the short housing without a test bearing as a model for the losses in the housing with test bearing. It is worth noting that the seal and housing losses in this apparatus were nearly as large as the test bearing torques. Housing losses were probably uncommonly high in this case because the housing was designed to accept bearings with L/D of up to 1.5 which leaves extra space at the ends of the bearing when L/D of one is used. Nevertheless, when computing total power requirements for a bearing-rotor system, the designer would be well advised to analyze the seal and housing losses to insure that adequate allowance for them is made.

DYNAMIC PERFORMANCE OF THE TILTING-PAD BEARING

In rotating machinery design analysis, the dynamic properties of bearings are used as inputs to a rotor-dynamics analysis which determines:

(a) Critical speeds of the rotor-bearing system.

(b) Response of the rotor to unbalance or other dynamic load.

(c) Hydrodynamic stability boundaries of the rotor-bearing system.

The stiffness and damping properties of the journal bearings have a strong influence on the dynamic characteristics of the rotor-bearing system.

Therefore, the most straightforward and meaningful way of evaluating the dynamic properties of journal bearings in the test apparatus is to experimentally observe the dynamic performance of the system as the operating conditions are varied. The experimental observations can then be compared with the critical speeds, response, and stability characteristics which have been calculated from a rotor-dynamics analysis of the test apparatus in which the theoretical bearing stiffness and damping coefficients are used. This amounts to performing a design analysis of the test apparatus rotor-dynamics by using the theoretical bearing data,and then evaluating the analysis, and thus the bearing data, by experimental measurement.

The rotor-dynamics analysis is based on the assumption that for small amplitudes of motion the bearing fluid film forces can be linearized and expressed by means of spring and damping coefficients (ref. 11). The method used in the analysis of rotor motion is that of Myklestad-Prohl (ref. 12) which is an extension of the Holzer method. The rotor is represented by a finite number of mass points connected by weightless elastic elements. Thus, the rotor is divided into a suitable number of sections (in this case, eight) with each section having a constant stiffness along its length and with the mass of the section divided into two parts which are concentrated at the end points of the sections.

The MTI program provides for including the effects of pedestal flexibility. The pedestal is represented by a mass and a mass moment of inertia and is supported on springs and dashpots for both translatory and rotational motion. In these calculations, this feature is used to include the effects of bearing pivot flexibility. The elastic stiffness of the pivots was calculated and found to be 5.5×10^5 pounds per inch at 100-pounds load (stiffness varies as the 2/3 power of load). The measured stiffness, obtained by measuring shaft deflection when loaded without rotation, was 5.12×10^5 pounds per inch and it remained nearly constant over the range of load. A pedestal stiffness of 5.5×10^5 pounds per inch was used for all conditions in the rotor-dynamic analysis and the pad mass and mass moment of inertia were inserted. The pedestal damping and the stiffness for rotational motion were made equal to zero.

Critical Speeds

The critical speed map of the experimental rotor-bearing system is shown in Fig. 40. The support bearing stiffness was determined (ref. 13) and is assumed to be constant at 1.3×10^6 pounds per inch independent of test bearing stiffness. The critical speeds of the system with a particular test bearing in place can be determined by plotting the curve of test bearing stiffness as a function of speed. The system critical speeds are then defined by the intersection of the bearing stiffness versus speed curve and the resonance frequency versus bearing stiffness curves. Several dashed line curves of tilting-pad test bearing stiffness are given in Fig. 40 to illustrate the effects of preload and static load on the system critical speeds.

Ordinarily, rotor-bearing systems with even slight amounts of damping will go through the two lowest system critical speeds without any sharp peak in vibration amplitude. This has been the case with the test apparatus as will be shown in the results on shaft response to dynamic load. In the absence of a peak in vibration amplitude or a very rapid shift in phase angle between unbalance force and shaft response, it has not been possible to identify the first system critical speed experimentally. The second and third critical speeds are above the operating speed range.

Response to Dynamic Load

The theoretical response of the shaft to a rotating unbalance load is a circular orbit for four shoe tilting-pad bearings with the static load directed midway between pivots. The shaft center orbits measured at the test bearing were characteristically circular and very stable. This is illustrated by the oscilloscope photograph, Fig. 41(b), of the filtered, a-c component of the shaft displacement signal. Figure 41(a) is a photograph of the orbit at the test bearing without filters and with d-c coupling. The high-frequency "hash" in the unfiltered signal is caused by magnetic inhomogenities of the shaft. The clearance "square" is shown also in Fig. 41(a). The pivots are oriented at 45 degrees from the grid lines and this results in the characteristic square-on-edge shape of the clearance space for a four-pad bearing. The pivot clearance, C_p, is half of the side of the square.

The experimental procedure was to operate at constant speed, fixed Reynolds Number, and vary the static load to show the variation with Sommerfeld Number of the response orbit amplitude and the phase angle between unbalance force and shaft response. The unbalance weight was chosen to give a response orbit diameter of less than 0.2 times the radial pivot clearance (C_p) for each operating condition. This limitation on response orbit dimensions was applied to maintain linearity between the exciting force and response orbit amplitudes and to avoid transmission of large dynamic forces through the pedestals and support structure.

The response of the shaft was calculated using the theoretical bearing stiffness and damping coefficients for conditions corresponding to those of the experiments. The theoretical curves and experimental data points of response orbit amplitude are given for comparison in Figs. 42 and 43 for $m = 0$ and Figs. 44 and 45 for $m = 0.5$. The agreement is very good considering the many other characteristics of the entire rotor-bearing-support assembly which can influence the results.

Measured and calculated phase angles do not agree as well (sample results are given in Fig. 46), but this is not surprising since the accuracy of measurement is not as good and the experimental results can be affected greatly if the response orbit is not precisely circular. Agreement between theoretical and experimental results very similar to that shown in Fig. 46 was obtained for the other Reynolds Numbers.

In most instances, rotor response analysis for design purposes is performed by calculating the response of a proposed rotor-bearing system as the speed is increased through the operating range. As was mentioned before, the experimental procedure was different in that a fixed speed was maintained while the static load was changed to vary the bearing properties. However, sample results similar to those which would normally be obtained in design analysis can be had by plotting the response at the different speeds for the same static load. This is done for the m = 0 bearing in Fig. 47 and for the m = 0.5 bearing in Fig. 48. Again, good agreement between experimental and theory is demonstrated. The response curves characteristically reach a maximum at or shortly after the first critical speed.

The response curves show that the higher stiffness and damping of the preloaded bearing result in a substantial increase in the first critical speed of the system and the response orbit amplitude is about half that of the upreloaded bearing for equivalent operating conditions. Increasing the static load on either bearing results in a much smaller increase in the critical speed. Increased load reduces the response amplitude noticeably at speeds well below the first critical speed, but there is very little effect as the first critical speed is reached and exceeded.

Overall, the comparisons between calculated and measured dynamic behavior of the apparatus are convicning evidence that the theoretical bearing stiffness and damping coefficients for the tilting-pad bearing in laminar and turbulent regimes permit reliable dynamic analysis of rotor-bearing systems.

Bearing Stability

The tilting-pad bearing should be stable as long as the pads track the motions of the journal center. This means that the operating speed should be substantially less than the natural frequency of the spring-mass system representing the pad and its lubricant film. The critical mass moment of inertia (M_{cr}) of the pads for resonance of the pad-film system can be calculated from the curves of Figs. 24 through 27. A conservative criterion for pad following is to specify that the operating speed should be less than half the natural frequency of the pad and film. This means that: $\sqrt{M_{cr}/M_{pad}} > 2$.

The actual mass moment of inertia of the pads (M_{pad}) is 6.7×10^{-4} lb.sec^2/in. The values of M_{cr} for the bearing with m = 0.5 range from 0.1 to 0.32 lb.sec^2/in., so $\sqrt{M_{cr}/M_{pad}}$ ranges from 12.2 to 21.9. Therefore, there should have been no problem with pad flutter or instability with the m = 0.5 bearing.

As was predicted, there was no evidence of instability for any operating condition, including zero load, for the bearing with m = 0.5. In addition, the pad motions, as measured by the probes mounted in the ring and referencing against the back of the pad, remained close to being in phase with the shaft motions. This is illustrated by the oscilloscope traces of the pad pitch and roll motions shown in Fig. 49a. The interruption in the traces is caused by the unbalance force position marker and it indicates that at that time the force is directed vertically upward. If there were zero phase angles between unbalance force and shaft motion and between shaft and pad motions, the marker should occur at the midplane of the sinusoidal signal (zero tilt). Actually the markers occur about 70 degrees past the midplane (the beam sweeps from left to right). The unbalance force/shaft motion phase angles for these operating conditions were about 40 degrees, so the phase angle between shaft and pad motions is about 30 degrees. The amplitude of the roll motion (cyclic, axial misalignment) remained fairly constant for all values of load and speed. The pitch and roll motions were usually nearly 90 degrees out of phase, as shown in Fig. 49a, although there were some small variations.

The values of M_{cr} for the bearing with m = 0 range from about 0.03 to 0.1 lb.sec^2/in. so $\sqrt{M_{cr}/M_{pad}}$ ranges from 6.7 to 12.2. Again, the criterion indicates that the pads should follow and the bearing should be stable. However, with the m = 0 bearing, very small amplitude fractional frequency whirl was observed for loads of about 20 pounds or less at speeds of 6000 rpm and higher. This is illustrated by the oscilloscope traces of pad motion and shaft center locus for 20 pounds load and 6400 rpm in Fig. 49b. The dominant motions are a synchronous pitch and roll of the pad in response to a rotating unbalance load. In addition, there is a smaller motion at almost exactly half synchronous frequency which appears as a "double loop" shaft motion orbit and as a beat effect on the pad motions. The small interruptions in the traces are from the synchronous unbalance force location marker.

While fractional-frequency whirl instability can occur in tilting-pad bearings, it seems clear that it is limited to high-speed, very lightly loaded operation with unpreloaded bearings for the pad masses obtained by normal design practice. Even when whirl does occur, it should be very well controlled with amplitudes too small to endanger bearing operation. Even so, it is probably desirable to use some preload on these bearings to prevent flutter of the unloaded pads which could result in pivot fretting. There was no sign of pivot fretting on the test bearing after several hundred hours total bearing operation. There may be difficulty with pivot fretting over longer periods of operation with other fluids which are poor lubricants. However, silicone oil is known to be a poor boundary lubricant for steels, so the experience in these tests is encouraging.

PART III

APPLICATION OF THE TILTING-PAD BEARING TO LIQUID-METAL LUBRICATED MACHINERY

Special considerations applicable to the choice and design of tilting-pad bearings for high-speed rotary machines with liquid metals as the working fluid are discussed.

The tilting-pad journal bearing has been proposed as an outstanding choice for liquid-metal lubricated space power applications principally because of its excellent dynamic characteristics including stability. The experimental results have confirmed these advantages. Equally important, the experimental results have verified the theoretical design data for the bearing for a wide range of conditions from laminar flow to Reynolds numbers as high as 12,000. Thus, the design data curves given in the report can be used with confidence in the analysis of proposed rotor-bearing systems including static load capacity, friction torque, critical speeds, response to dynamic load, system stability and flow requirements.

The choice of a bearing type, and following this, the choice of values for the design variables of that bearing for an application as difficult and complex as liquid-metal lubricated space-power machinery requires consideration of many factors. Design data such as are given here for the tilting-pad bearing are essential in order to make such choices rationally. There are other factors to be considered also, and some of these which might influence the choice of the tilting-pad bearing or its design are:

1. Large thermal gradients and the desire to keep structure weight low make the possibility of bearing misalignment very likely in these applications. The tilting-pad bearing with point-contact pivots can accept sizeable misalignments without adverse effect.

2. Pivot fretting may occur with poor lubricating fluids such as liquid metals. As yet, there is no firm evidence that the problem is real, but care should be exercised to keep pivot stresses low and to hold slip of the surfaces in the pivot contact as low as possible.

3. Preloading the tilting-pad bearing results in greater stiffness and damping and thus improves dynamic characteristics. It also means lower minimum film thickness and, usually, higher power loss. Fractional-frequency whirl has been observed in the unpreloaded tilting-pad bearing at high speeds and very light loads, but the amplitudes of the motion were very small and did not represent a real threat to bearing performance. Preloading can stop instability completely.

4. In design analysis of any high-speed rotor-bearing system, the effect of centrifugal growth of the shaft on bearing clearance should be investigated. This is especially true for hollow shafts.

5. In calculations of rotor-bearing system power losses, the drag from bearing seals and from losses inside the bearing housing but outside the bearing itself should be considered carefully since they are likely to be nearly as large as the direct bearing losses. Substantial savings in power consumption should be possible from careful design of seals and housings.

6. One of the most effective ways of reducing bearing power loss is to reduce shaft diameter. The liquid-metal lubricated space power machines constructed to date have been rigid shaft machines which operate well below the third system critical speed (free-free mode). Shaft and bearing sizes have

been dictated by the desire to stay below the third critical speed and not by any need for extra bearing load capacity. A flexible-shaft machine with smaller bearings would have substantially lower power loss but there would be more difficult problems of system dynamics. The excellent dynamic characteristics of tilting-pad bearings could be a factor in the development of flexible-shaft, liquid-metal lubricated machinery.

7. Large quantities of lubricant can be circulated through the tilting-pad bearing housing for cooling with little expenditure of pumping power since there is very little restriction to flow. The temperature rise from inlet to exit of a single pad in the tilting-pad bearing is normally on the order of 10 F or lower, so bearing temperatures can be effectively controlled by controlling the bulk lubricant temperature within the bearing housing.

8. There are indications that cavitation erosion damage may occur in high-speed liquid-metal lubricated bearings under some conditions. The tilting-pad bearing should have relatively low susceptibility to such damage because the short pad arc helps insure adequate lubricant supply to all areas of the film in the event of high-frequency vibrations, and because regions of subambient film pressure are minimized. The four-pad bearing has some advantage over the three-pad bearing in this respect.

Long duration operating tests using liquid-metal lubricants with realistic operating conditions are required before there can be firm assurance that the technology needed for design of reliable liquid-metal lubricated, tilting-pad journal bearings is available. During such testing, the potential problems of pivot fretting and cavitation erosion would be investigated. Also tests with liquid metal lubricant would permit evaluation of bearing materials to withstand repeated starts and stops and occasional, brief high-speed contacts without deleterious effects on bearing performance.

NOMENCLATURE

a	geometrical preload, inches
B	damping coefficient, lb.sec/inch
C_B	bearing radial clearance $(= C_P(1-m))$, inches
C_P	pad radial clearance (= radius of curvature of pad - radius of curvature of shaft), inches
D	diameter, inches
e_B	bearing eccentricity (= distance between journal and bearing centers), inches
e_P	pad eccentricity (= distance between center of journal and center of curvature of pad), inches
f	coefficient of friction
F	force, lbs
F_o	steady state force, lbs
F_x, F_y	components of dynamic force, lbs.
I	mass moment of inertia of pad around axial axis, lb.in.sec^2
K	stiffness coefficient, lbs/inch
L	length, inches
m	geometrical preload coefficient $(= \frac{a}{C_P})$
M	equivalent pad mass $(= I/(R_p)^2)$, lb sec^2/in
M_{crit}	equivalent mass of bearing pad for resonance, lbs.sec^2/inch
N	speed, rps
Q	flow into bearing pad, in^3/sec
Q_s	side leakage flow, in^3/sec
R	radius, inches
Re	Reynolds Number $(= \pi \, DNC_P \, \rho/\mu)$
S	Sommerfeld Number $(= \frac{\mu NLD}{W}(\frac{R}{C_P})^2)$
T	dimensionless torque $= \frac{\tau}{C_p W}$
W	steady-state bearing load (= vector sum of the loads on the individual pads), lbs.
x, y	co-ordinates, inches

β angular extent of pad, degrees

ε_B bearing eccentricity ratio $(= \frac{e_B}{C_B})$

ε_P pad eccentricity ratio $(= \frac{e_P}{C_P})$

θ_P angular distance of pivot point from inlet of pad, degrees

ρ mass density, $\frac{\text{lb.sec}^2}{\text{in}^4}$

τ torque, in-lb.

ω angular speed, radians/second

μ absolute viscosity, $\frac{\text{lb.sec}}{\text{in}^2}$

APPENDIX A

NUMERICAL ANALYSIS FOR LINEARIZED, TURBULENT INCOMPRESSIBLE, FULL AND PARTIAL JOURNAL BEARINGS

by C. W. Ng
Mechanical Technology Incorporated

This section describes the Reynolds equation based on the linearized turbulent lubrication theory and its finite difference form. Boundary conditions are given for the full journal and partial arc bearing. Expressions for flow and torque are given. Finally, the method for iteration and extrapolation as well as the criterion for convergence are discussed in detail.

Reynolds Equation for Turbulent Lubrication

Let the flow per inch in the fluid film be denoted Q with the components Q_x and Q_z. Then, from the thin film approximation of incompressible Navier-Stokes Equation. (see ref. 14).

$$Q_x = \frac{1}{2} \; R\omega\bar{h} \; - G_x \frac{\bar{h}^3}{\mu} \frac{\partial \bar{P}}{\partial \bar{x}} \tag{A1}$$

$$Q_z = - G_z \frac{\bar{h}^3}{\mu} \frac{\partial \bar{P}}{\partial \bar{z}} \tag{A2}$$

where

$\bar{P}$	=	pressure, psi
$\bar{h}$	=	film thickness, inch
$\bar{\mu}$	=	viscosity of lubricant, lb.sec/in.^{2}
R	=	journal radius, inch
ω	=	angular velocity, rad/sec.
G_x, G_z	=	flow parameter, equal to 1/12 for laminar flow and for turbulent flow, they are functions of Reynolds number (linearized theory) and pressure gradient in the flow direction as well as perpendicular to it, (non-linear theory) see refs. 5 and 8.

Other notation which is used in developing this analysis is given in the Nomenclature at the end of this Appendix.

The continuity equation is:

$$\frac{\partial}{\partial \bar{x}} \; (Q_x) + \frac{\partial}{\partial \bar{z}} \; (Q_z) \; \frac{\partial \bar{h}}{\partial t} \; = \; 0 \tag{A3}$$

Introduce Eqs. (A1) and (A2) into Eq. (A3)

$$\frac{\partial}{\partial x}\left[G_x \frac{\bar{h}^3}{\mu} \frac{\partial \bar{P}}{\partial \bar{x}}\right] + \frac{\partial}{\partial z}\left[G_z \frac{\bar{h}^3}{\mu} \frac{\partial \bar{P}}{\partial \bar{z}}\right] = \frac{1}{2} R\omega \frac{\partial \bar{h}}{\partial \bar{x}} + \frac{\partial \bar{h}}{\partial t} \qquad (A4)$$

To obtain the dimensionless form, set

$$h = \bar{h}/C = 1 + \epsilon \cos(\theta - \phi)$$

$$P = \bar{P}/\mu N \left(\frac{R}{C}\right)^2, \quad \omega = 2\pi N$$

$$x = \bar{x}/D, \quad z = \bar{z}/L, \quad \theta = \bar{x}/R = 2x$$

Hence the dimensionless Reynolds Equation is:

$$\frac{\partial}{\partial x}\left[G_x h^3 \frac{\partial P}{\partial x}\right] + \left(\frac{D}{L}\right)^2 \frac{\partial}{\partial z}\left[G_z h^3 \frac{\partial P}{\partial z}\right] = 8\pi\left[\frac{\epsilon}{\omega}\cos(\theta - \phi) + \left(\frac{\epsilon\dot{\phi}}{\omega} - \frac{\epsilon}{2}\right)\sin(\theta - \phi)\right] \qquad (A5)$$

Finite Difference Equations

The Reynolds equation is solved numerically by finite difference methods. The bearing film is subdivided into a mesh shown in the figure below. Equation (A5) can be written in the finite difference form.

$$P_{i,j} = \frac{\left\{\begin{aligned} &- 8\pi (\Delta X)^2 \left[\frac{\epsilon}{\omega}\cos(\theta-\phi) + \left(\frac{\epsilon\dot{\phi}}{\omega} - \frac{\epsilon}{2}\right)\sin(\theta-\phi)\right]_{i,j} \\ &+ G_x h^3\Big|_{i,j+\frac{1}{2}} P_{i,j+1} + G_x h^3\Big|_{i,j-\frac{1}{2}} P_{i,j-1} \\ &+ \left(\frac{D}{L}\right)^2 \left(\frac{\Delta X}{\Delta Z}\right)^2 \left[G_z h^3\Big|_{i+\frac{1}{2},j} P_{i+1,j} + G_z h^3\Big|_{i-\frac{1}{2},j} P_{i-1,j}\right] \end{aligned}\right\}}{G_x h^3\Big|_{i,j+\frac{1}{2}} + G_x h^3\Big|_{i,j-\frac{1}{2}} + \left(\frac{D}{L}\frac{\Delta X}{\Delta Z}\right)^2 \left[G_z h^3\Big|_{i+\frac{1}{2},j} + G_z h^3\Big|_{i-\frac{1}{2},j}\right]} \qquad (A6)$$

The boundary conditions are:

$i = 1 \qquad P_{1,j} = 0$

$i = n + 1 \qquad P_{n+2,j} = P_{n,j}$

$$j = 1 \qquad P_{i,1} = \begin{cases} P_{inlet} & \text{partial arc} \\ P_{i,m+1} & \text{full journal} \end{cases}$$

$$j = n + 1 \qquad P_{i,m+1} = \begin{cases} P_{outlet} & \text{partial arc} \\ P_{i,1} & \text{full journal} \end{cases}$$

$i,j \qquad$ If $(P_{i,j})_{calculated} < P_{cavitation} \rightarrow P_{i,j} = P_{cavitation}$

The pressure is initially set equal to zero and Eq. (A6) is then solved by iteration. Pressure derivatives are found from the pressure distribution and they will be used to compute the dimensionless flow.

The load carrying capacity is calculated from

$$f_r = -2 \int_0^{\frac{1}{2}} \int_{\theta_{in}}^{\theta_{out}} P \cos(\theta - \phi)\, dxdz = -2\Delta x \cdot \Delta z \sum_{i,j} P_{i,j} \cos(\theta_{i,j} - \phi) \qquad (A7)$$

$$f_t = 2 \int_0^{\frac{1}{2}} \int_{\theta_{in}}^{\theta_{out}} P \sin(\theta - \phi)\, dxdz = 2\Delta x \cdot \Delta z \sum_{i,j} P_{i,j} \sin(\theta_{i,j} - \phi) \qquad (A8)$$

$$\frac{W}{\mu NDL(\frac{R}{C})^2} = \frac{1}{S} = \sqrt{f_r^2 + f_t^2}$$

$$\phi_{calc} = \tan^{-1}(f_t/f_r)$$

where f_r is the dimensionless radial force component, f_t is the tangential component, S is the Sommerfeld number and ϕ_{calc} is the calculated attitude angle.

The indicated summations are computed by Simpson rule of integration, i.e., $\frac{1}{3}\Delta\left[P_1 + 4P_2 + 2P_3 + 4P_4 + - - - -\right]$ and if either m or n are odd the first interval is integrated by $\frac{1}{12\Delta}\left[5P_1 + 8P_2 - P_3\right]$. In addition, end corrections are made at the boundary to the ruptured film.

The dimensionless flow components are expressed by

$$\frac{Q_x}{RCNL} = h\pi - h^3 G_x \int_o^1 \frac{\partial P}{\partial \theta} dz'$$

$$\frac{Q_z}{RCNL} = -\frac{1}{2}\left(\frac{D}{L}\right)^2 \int_o^{2\pi} h^3 G_z \frac{\partial P}{\partial z} d\theta$$

And the dimensionless frictional torque is defined as,

$$\bar{F} = \frac{T}{WC}$$

$$= \frac{1}{WC}\int_{-\frac{1}{2}}^{\frac{1}{2}} d\bar{z} \int_o^{2\pi} \tau w R^2 d\theta$$

τw = shear stress on journal surface

W = load

The above integral is calculated with the help of the following relation:

$$\tau w = \tau_c + \frac{\bar{h}}{2R}\frac{\partial \bar{P}}{\partial \theta}$$

where

$$\tau_c = \frac{C_f}{8}\rho V^2$$

C_f being the coefficient of friction for the Couette flow corresponding to the local gap. Thus,

$$\int_{-\frac{1}{2}}^{\frac{1}{2}} d\bar{z} \int_o^{2\pi} \tau_w R d\theta$$

$$= \int_{-\frac{1}{2}}^{\frac{1}{2}} d\bar{z} \int_o^{2\pi} \left(\tau_c + \frac{\bar{h}}{2R}\frac{\partial \bar{P}}{\partial \theta}\right) R d\theta$$

$$= LR\int_o^{2\pi} \tau_c d\theta + \frac{1}{2}\int_{-\frac{1}{2}}^{\frac{1}{2}} dz \left\{(\bar{P}\bar{h})_{outlet} - (\bar{P}\bar{h})_{inlet} - \int_o^{2\pi} \bar{P}\frac{\partial \bar{h}}{\partial \theta} d\theta\right\}$$

$$= L\left\{R\int_o^{2\pi} \tau_c\, d\theta + \frac{1}{2}\left[(\bar{P}\bar{h})_{outlet} - (\bar{P}\bar{h})_{inlet} + \mu NC\left(\frac{R}{C}\right)^2 \epsilon\ f_t\right\}\right.$$

In the computation of the friction torque; when cavitation is present the cavitated area is reduced by the ratio of h_{min}/h_{local}. Also the frictional coefficient is given in the form of $2\tau/\rho V^2$ which is conventionally used to study the flow between rotating cylinders. The definitions of G_x, G_z, and C_f, are given in ref. 5.

Iteration Convergence and Extrapolation

The convergence of the pressure iteration is tested for relative convergence as well as absolute convergence. The relative convergence is tested as follows: after the k'th pressure iteration compute:

$$\frac{\sum\limits_i \sum\limits_j \left| P_{i,j}^{(k)} - P_{i,j}^{(k-1)} \right|}{\sum\limits_i \sum\limits_j P_{i,j}^{(k)}} - \delta_R = \Delta_R \tag{A9}$$

where δ_R is given by the input. When Δ_R becomes zero or negative then relative convergence has been achieved.

To compute the absolute convergence the following criteria is chosen. After each iteration the sum of the pressures are computed. Let the result for the k'th iteration be denoted:

$$y_k = \sum_i \sum_j P_{i,j}^{(k)} \tag{A10}$$

Assume that after infinitely many iterations this sum will be $y_{k\infty}$ and set:

$$y_k = y_{k\infty} - Ae^{-Bk} \quad \text{(A and B constants)}$$

from which one can show

$$y_{k\infty} = y_k + \frac{(y_k - y_{k-1})^2}{2y_{k-1} - y_{k-2} - y_k} \tag{A11}$$

$y_{k\infty}$ is calculated after each iteration (exceptions, see later) and the absolute convergence is computed from:

$$\frac{y_{k\infty} - y_k}{y_k} - \delta_A = \Delta_A \tag{A12}$$

where δ_A is given by the input. When Δ_A becomes zero or negative absolute convergence has been achieved.

Equations (A9), (A11) and (A12) are printed as output after each iteration. Equation (A11) serves an additional purpose, namely to extrapolate the pressure distribution. When y_k becomes a smooth curve and starts to level off then a new extrapolated pressure distribution is calculated from

$$P_{i,j} = \frac{y_{k\infty}}{y_k} \cdot P_{i,j}^{(k)} \tag{A13}$$

and the pressure iterations proceed from this new distribution either until convergence is achieved or until y_k again becomes sufficiently smooth that Eq. (A13) may be used once more.

It remains to define the meaning of "smoothness". Equation (A11) is not executed after the first two iterations or after the two iterations following a pressure extrapolation. In there cases the computer output shows:

$$\left.\begin{aligned} y_{k\infty} &= 10^5 \\ \Delta_A &= 1.0 \end{aligned}\right\} \tag{A14}$$

Furthermore, $y_{k\infty}$ is not calculated if the y_k-curve is not monotonically tending toward a limit as controlled by an input quantity δ_{ex}. The criteria for executing Eq. (A13) are:

$$\left.\begin{aligned} &\text{a)}\quad 0 \leq \left(\frac{y_{k-1,\infty} - y_{k-2,\infty}}{y_{k-1,\infty}}\right) \leq \delta_{ex} \\ &\text{b)}\quad 0 \leq \left(\frac{y_{k\infty} - y_{k-1,\infty}}{y_{k\infty}}\right) \leq \delta_{ex} \\ &\text{c)}\quad \Delta_A \neq 1.0 \\ &\text{d)}\quad k \geq 4,\ (k - k_{\text{extrapolation}}) \geq 4 \end{aligned}\right\} \begin{array}{l}\text{When these equations are} \\ \text{satisfied Eq. (A13) is} \\ \text{performed, otherwise not.}\end{array} \tag{A15}$$

NOMENCLATURE FOR APPENDIX A

C	Radial clearance, inch
D	Journal diameter, inch
F	Force, lbs
$\bar{F}$	Dimensionless frictional force
f	Friction coefficient = F/W
f_r, f_t	Radial and tangential force components, dimensionless, see Fig. 2
f_v, f_h	Vertical and horizontal force components, dimensionless, see Fig. 2
h	Dimensionless film thickness
i, j	Finite difference coordinates, axial and circumferential
k	Iteration number
L	Bearing length, inch
m	Number of circumferential subdivisions
n	Number of axial subdivisions
N	Journal speed, rps
P	Dimensionless pressure (above ambient)
Q_x, Q_z	Flow in x,z direction, in^3/sec
R	Journal radius, inch
S	Sommerfeld number
t	Time, seconds
x, z	Circumferential and axial coordinates, dimensionless
y_k	Sum of all pressures after the k'th iteration, see Eq. (A10)
$y_{k\infty}$	Extrapolated pressure sum after the k'th iteration, see Eq. (A11)
α	Attitude angle, degrees
$\dot{\alpha}$	Tangential speed of journal center, rad/sec.
δ_A	Absolute convergence limit, see Eq. (A12)
δ_R	Relative convergence limit, see Eq. (A9)
Δ_A	Error in absolute convergence, see Eq. (A12)
Δ_R	Error in relative convergence, see Eq. (A9)
ϵ	Eccentricity ratio
$\dot{\epsilon}$	Radial speed of journal center, sec^{-1}

θ Circumferential angular coordinate, see Fig. 2

μ Viscosity, lbs-sec/in^2

ω Angular speed of journal, rad/sec.

APPENDIX B

DYNAMIC LOAD ANALYSIS OF THE TILTING-PAD BEARING

By J. Lund and C. W. Ng
Mechanical Technology Incorporated

Steady-state Equilibrium

Referring to Fig. B-1 and the nomenclature at the end of this Appendix, let the center of the tilting-pad bearing be O_B. The bearing is made up of a number of tilting pads, the arbitrary pad having the pivot point P located at an angle ψ from the vertical load line. The pad is free to tilt around the pivot point which for convenience is assumed to be located on the surface of the pad. The steady-state position of the journal center is O_J which is the origin of two fixed coordinate systems: The x-y system (x-axis vertical downward, y-axis horizontal) and the ξ-η system (the ξ-axis is parallel to the line O_BP). The location of O_J with respect to the bearing center is given by the eccentricity $O_BO_J = e_o = C'\epsilon_o$ and the attitude angle ϕ_o. The steady-state position of the pad center is designated O_n such that the journal center eccentricity with respect to the pad is determined by $O_nO_J = e = C\epsilon$. The corresponding attitude angle is ϕ. The journal radius is R, the radius of the pad is $O_nP = R+C$ and the radius of the circle passing through all pivot points with center in O_B is $O_BP = R+C'$.

The point O_{no} is the center of curvature of the pad with no tilting. Hence, $O_{no}O_n$ is a circular arc, or for small motions, a line perpendicular to $O_{no}P$. Projecting O_J on $O_{no}P$ yields:

$$\epsilon \cos \phi = 1 - \frac{C'}{C} - \frac{C'}{C} \epsilon_o \cos (\psi - \phi_o) \tag{B1}$$

This equation contains three unknowns, namely ϵ, ϕ and ϕ_o since ϵ_o is the independent variable. The second equation derives from the requirement that the force on the pad passes through the pivot point which establishes a relationship between ϵ and ϕ (i.e. the journal center locus with respect to the pad). The third relationship is the requirement that the total horizontal force component (in the y-direction), summed over all pads, is zero:

$$\sum_{\substack{\text{all} \\ \text{pads}}} F_{\sin \psi} = 0 \tag{B2}$$

Equation (B2) is usually used to determine ϕ_o by trial-and-error as follows: for a particular case ϵ_o, $\frac{C'}{C}$ and ψ are known in Eq. (B1). For several assumed values of ϕ_o calculate $\epsilon \cos \phi$ for each pad, determine the pad forces F from available pad data and plot Σ F sin ψ as a function of ϕ_o. The zero point determines the desired value of ϕ_o.

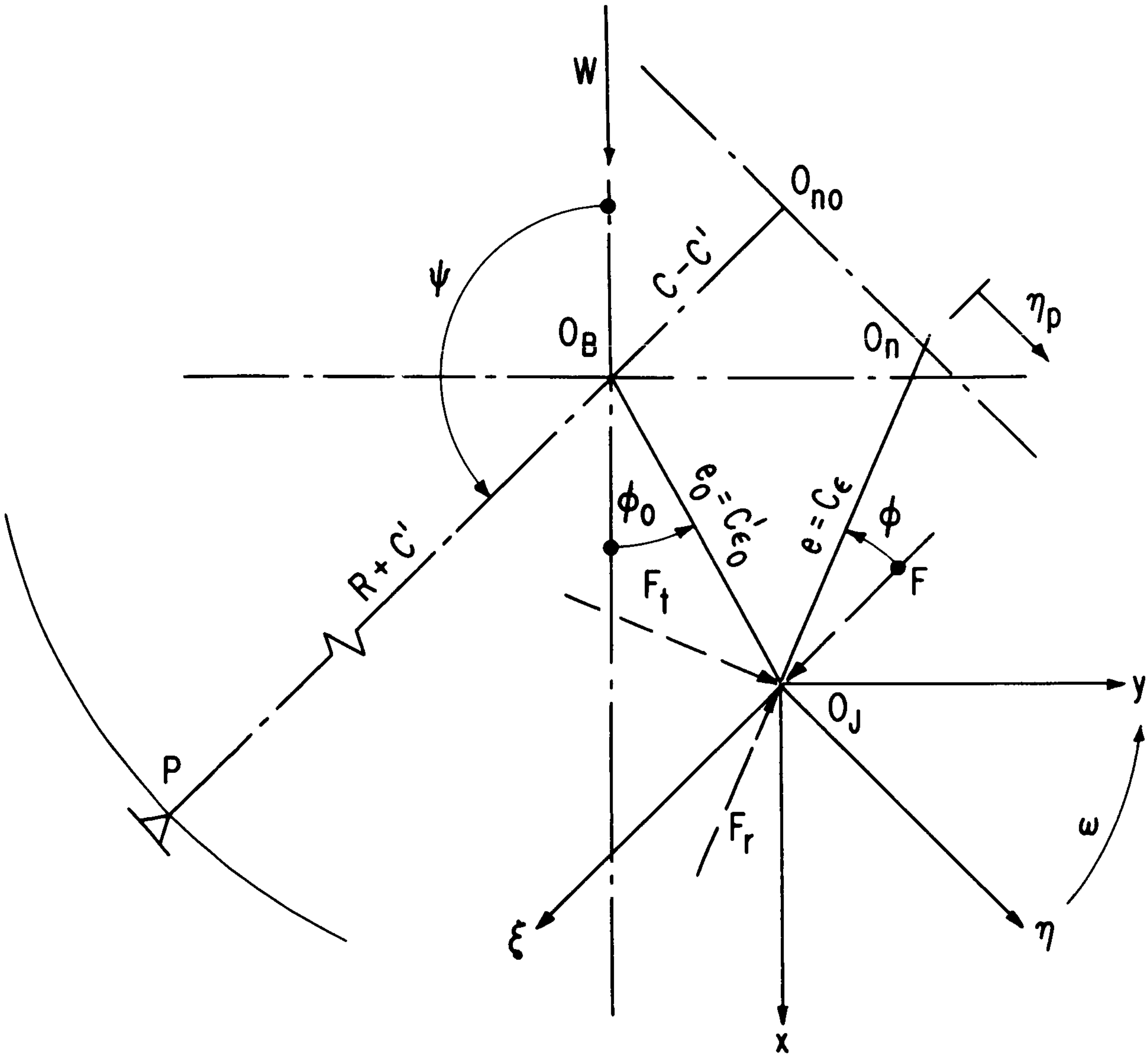

Fig. B 1 Coordinate System for Analysis

The procedure is at best tedious. It becomes very complicated if the pivot point is not in the center of the pad in which case the pad force F can be a multivalued function of $\epsilon \cos \phi$. However, when the pivot points are located symmetrically with respect to the vertical load line through the bearing center O_B then $\phi_o = 0$. A further simplification arises when the pivot point is in the center of the pad since the pad force F then is uniquely determined by $\epsilon \cos \phi$. The analysis requires only that ϵ and ϕ are known for each pad. How these values have been arrived at is immaterial in so far as the analysis is concerned.

Fixed Pad Coefficients

In order to determine the spring and damping coefficients for the complete tilting-pad bearing it is necessary to know the forces and their derivatives for each pad as if the pad was fixed. Under steady-state conditions the journal center has the eccentricity ratio ϵ and the attitude angle ϕ with respect to the pad center. The fluid film pad force has the components F_ξ and F_η and under steady-state conditions the resultant force passes through the pivot point, i.e., $F_\xi = -F$ and $F_\eta = 0$, see Fig. B1. Thus, F denotes the load on the pad. Usually, the force is resolved along the radial and the tangential directions with the components F_r and F_t, respectively, see Fig. B1. Hence:

$$\begin{Bmatrix} F_\xi \\ F_\eta \end{Bmatrix} = \begin{Bmatrix} -F \\ 0 \end{Bmatrix} = - \begin{Bmatrix} \cos \phi & \sin \phi \\ \sin \phi & -\cos\phi \end{Bmatrix} \begin{Bmatrix} F_r \\ F_t \end{Bmatrix} \tag{B3}$$

For infinitesimally small motion around the steady-state position the dynamic forces become from Eq. (B3):

$$\begin{Bmatrix} dF_\xi \\ dF_\eta \end{Bmatrix} = - \begin{Bmatrix} \cos \phi & \sin \phi \\ \sin \phi & -\cos \phi \end{Bmatrix} \begin{Bmatrix} dF_r + F_t \, d\phi \\ dF_t - F_r \, d\phi \end{Bmatrix} \tag{B4}$$

The infinitesimal dynamic motion of the journal center is described by the coordinates (ξ, η):

$$\xi = d\,(e \cos \phi) \qquad \eta = d(e \sin \phi)$$

or

$$\begin{Bmatrix} de \\ ed\,\phi \end{Bmatrix} = \begin{Bmatrix} \cos \phi & \sin \phi \\ -\sin \phi & \cos \phi \end{Bmatrix} \begin{Bmatrix} \xi \\ \eta \end{Bmatrix} \tag{B5}$$

The velocities transform similarly:

$$\begin{Bmatrix} d\dot{e} \\ ed\,\dot{\phi} \end{Bmatrix} = \begin{Bmatrix} \cos \phi & \sin \phi \\ -\sin \phi & \cos \phi \end{Bmatrix} \begin{Bmatrix} \dot{\xi} \\ \dot{\eta} \end{Bmatrix} \tag{B6}$$

The dynamic force components dF_r and dF_t may be expressed in terms of the dynamic amplitudes. From Reynolds equation it can be shown that the fluid film force F can be written (refs. 11, 14):

$$F = \lambda\omega\left(1-2\frac{\dot\phi}{\omega}\right)\cdot f\left(\epsilon,\ \phi,\ \left(\frac{\dot\epsilon}{\omega}\right)/\left(1-2\frac{\dot\phi}{\omega}\right)\right) \tag{B7}$$

where:

$$\lambda = \frac{\mu RL}{\pi}\left(\frac{R}{C}\right)^2 \tag{B8}$$

$$F = \frac{1}{S_P} \tag{B9}$$

$$S_P = \frac{\mu NDL}{F}\left(\frac{R}{C}\right)^2 \qquad \text{(Pad Sommerfeld Number)} \tag{B10}$$

Therefore:

$$dF = \lambda\omega\left\{\left(1-2\frac{\dot\phi}{\omega}\right)\left[\frac{\partial f}{\partial\epsilon}d\epsilon + \frac{\partial f}{\epsilon\partial\phi}\epsilon d\phi + \frac{\partial f}{\partial\left(\frac{\dot\epsilon}{\omega},\left(1-2\frac{\dot\phi}{\omega}\right)\right)}d\left(\frac{\frac{\dot\epsilon}{\omega}}{1-2\frac{\dot\phi}{\omega}}\right)\right] - \frac{2f}{\omega\epsilon}\epsilon d\dot\phi\right\} \tag{B11}$$

Now:

$$d\left(\frac{\frac{\dot\epsilon}{\omega}}{1-2\frac{\dot\phi}{\omega}}\right) = \frac{1}{1-2\frac{\dot\phi}{\omega}}d\left(\frac{\dot\epsilon}{\omega}\right) + \frac{2\left(\frac{\dot\epsilon}{\omega}\right)}{\left|1-2\frac{\dot\phi}{\omega}\right|^2}d\left(\frac{\dot\phi}{\omega}\right) = d\left(\frac{\dot\epsilon}{\omega}\right)$$

because at the equilibrium position $\dot\epsilon = \dot\phi = 0$. Hence, Eq. (B11) reduces to:

$$dF = \frac{1}{C}\lambda\omega\left\{\frac{\partial f}{\partial\epsilon}de + \frac{\partial f}{\epsilon\partial\phi}ed\phi + \frac{1}{\omega}\frac{\partial f}{\partial(\dot\epsilon/\omega)}d\dot e - \frac{1}{\omega}\frac{2f}{\epsilon}ed\dot\phi\right\} \tag{B12}$$

Equation (B12) applies to both F_r and F_t. Let the corresponding dimensionless forces be denoted to f_r and f_t as defined by Eq. (B7). Thus, by substitution of Eq. (B12) into Eq. (B4):

$$\begin{Bmatrix} dF_\xi \\ dF_\eta \end{Bmatrix} = -\frac{1}{C}\lambda\omega\begin{Bmatrix} \cos\phi & \sin\phi \\ \sin\phi & -\cos\phi \end{Bmatrix}\left[\begin{pmatrix} \frac{\partial f_r}{\partial\epsilon} & \left(\frac{\partial f_r}{\epsilon\partial\phi} + \frac{f_t}{\epsilon}\right) \\ \frac{\partial f_t}{\partial\epsilon} & \left(\frac{\partial f_t}{\epsilon\partial\phi} - \frac{f_r}{\epsilon}\right) \end{pmatrix}\begin{Bmatrix} de \\ ed\phi \end{Bmatrix} + \frac{1}{\omega}\begin{pmatrix} \frac{\partial f_r}{\partial\frac{\dot\epsilon}{\omega}} & -\frac{2f_r}{\epsilon} \\ \frac{\partial f_t}{\partial\left(\frac{\dot\epsilon}{\omega}\right)} & \frac{2f_t}{\epsilon} \end{pmatrix}\begin{Bmatrix} d\dot e \\ ed\dot\phi \end{Bmatrix}\right] \tag{B13}$$

Define the fixed pads spring and damping coefficients by:

$$
\begin{aligned}
dF_\xi &= -K_{\xi\xi}\xi - C_{\xi\xi}\dot{\xi} - K_{\xi\eta}\eta - C_{\xi\eta}\dot{\eta} \\
dF_\eta &= -K_{\eta\xi}\xi - C_{\eta\xi}\dot{\xi} - K_{\eta\eta}\eta - C_{\eta\eta}\dot{\eta}
\end{aligned}
\tag{B14}
$$

To determine the eight coefficients, substitute Eq. (B5) and (B6) into Eq. (B13) and collect the terms in accordance with Eq. (B14) to get:

$$K_{\xi\xi} = \frac{1}{C}\lambda\omega\left[\frac{\partial f_r}{\partial\epsilon}\cos^2\phi - \frac{\partial f_t}{\epsilon\partial\phi}\sin^2\phi - \left(\frac{\partial f_r}{\epsilon\partial\phi} - \frac{\partial f_t}{\partial\epsilon}\right)\cos\phi\sin\phi - \frac{f_\eta}{\epsilon}\sin\phi\right] \tag{B15}$$

$$\omega C_{\xi\xi} = \frac{1}{C}\lambda\omega\left[\frac{\partial f_r}{\partial(\dot{\epsilon}/\omega)}\cos^2\phi + \frac{\partial f_t}{\partial(\dot{\epsilon}/\omega)}\cos\phi\sin\phi - \frac{2f_\xi}{\epsilon}\sin\phi\right] \tag{B16}$$

$$K_{\xi\eta} = \frac{1}{C}\lambda\omega\left[\frac{\partial f_r}{\epsilon\partial\phi}\cos^2\phi + \frac{\partial f_t}{\partial\epsilon}\sin^2\phi + \left(\frac{\partial f_t}{\epsilon\partial\phi} + \frac{\partial f_r}{\partial\epsilon}\right)\cos\phi\sin\phi + \frac{f_\eta}{\epsilon}\cos\phi\right] \tag{B17}$$

$$\omega C_{\xi\eta} = \frac{1}{C}\lambda\omega\left[\frac{\partial f_t}{\partial(\frac{\dot{\epsilon}}{\omega})}\sin^2\phi + \frac{\partial f_r}{\partial(\frac{\dot{\epsilon}}{\omega})}\cos\phi\sin\phi + \frac{2f_\xi}{\epsilon}\cos\phi\right] \tag{B18}$$

$$K_{\eta\xi} = \frac{1}{C}\lambda\omega\left[-\frac{\partial f_t}{\partial\epsilon}\cos^2\phi - \frac{\partial f_r}{\epsilon\partial\phi}\sin^2\phi + \left(\frac{\partial f_t}{\epsilon\partial\phi} + \frac{\partial f_r}{\partial\epsilon}\right)\cos\phi\sin\phi + \frac{f_\xi}{\epsilon}\sin\phi\right] \tag{B19}$$

$$\omega C_{\eta\xi} = \frac{1}{C}\lambda\omega\left[-\frac{\partial f_t}{\partial(\frac{\dot{\epsilon}}{\omega})}\cos^2\phi + \frac{\partial f_r}{\partial(\frac{\dot{\epsilon}}{\omega})}\cos\phi\sin\phi - \frac{2f_\eta}{\epsilon}\sin\phi\right] \tag{B20}$$

$$K_{\eta\eta} = \frac{1}{C}\lambda\omega\left[-\frac{\partial f_t}{\epsilon\partial\phi}\cos^2\phi + \frac{\partial f_r}{\partial\epsilon}\sin^2\phi + \left(\frac{\partial f_r}{\epsilon\partial\phi} - \frac{\partial f_t}{\partial\epsilon}\right)\cos\phi\sin\phi - \frac{f_\xi}{\epsilon}\cos\phi\right] \tag{B21}$$

$$\omega C_{\eta\eta} = \frac{1}{C}\lambda\omega\left[\frac{\partial f_r}{\partial(\frac{\dot{\epsilon}}{\omega})}\sin^2\phi - \frac{\partial f_t}{\partial(\frac{\dot{\epsilon}}{\omega})}\cos\phi\sin\phi + \frac{2f_\eta}{\epsilon}\cos\phi\right] \tag{B22}$$

Where:

$$f_\xi = \frac{-1}{S_P} \tag{B23}$$

$$f_\eta = 0 \tag{B24}$$

$$\frac{1}{C}\lambda\omega = \frac{1}{C} FS_P \tag{B25}$$

and all forces and derivatives are calculated for the given steady-state position defined by ϵ.

Tilting Pad Coefficients

Referring to Fig. B1, O_n is the steady-state position of the pad center. Under dynamic load the pad center oscillates around O_n with the amplitude η_P so η_P/R_P represents the dynamic tilting angle of the pad (R_P is the distance from the actual pad pivot to the pad center). The moment on the pad from the fluid film pressure is $-R_P dF_\eta$. Therefore, if the mass moment of inertia of the pad is I, the equation of motion becomes:

$$I \frac{\ddot{\eta}_P}{R_P} = -R_P \, dF_\eta$$

or

$$\frac{I}{R_P^2}\ddot{\eta}_P = M\ddot{\eta}_P = -dF_\eta \tag{B26}$$

where:

$$M = \frac{I}{R_P^2} \tag{B27}$$

Thus, under dynamic conditions η should be replaced by $(\eta-\eta_P)$ in Eq. (B14). In order to eliminate η_P substitute the expression for dF_η into Eq. (B26):

$$M\ddot{\eta}_P = K_{\eta\xi}\xi + C_{\eta\xi}\dot{\xi} + K_{\eta\eta}(\eta - \eta_P) + C_{\eta\eta}(\dot{\eta} - \dot{\eta}_P) \tag{B28}$$

Let the dynamic motion of the journal center around the steady-state position be harmonic:

$$(\xi,\eta)\, e^{i\omega t} \tag{B29}$$

Hence, solve Eq. (B28):

$$\eta - \eta_P = -\frac{(K_{\eta\xi} + i\omega C_{\eta\xi})\xi + M\omega^2\eta}{K_{\eta\eta} - M\omega^2 + i\omega C_{\eta\eta}} = -\left[(K_{\eta\xi} + i\omega C_{\eta\xi})\xi + M\omega^2\eta\right](P-iQ) \tag{B30}$$

where:

$$P = \frac{K_{\eta\eta} - M\omega^2}{(K_{\eta\eta} - M\omega^2)^2 + (\omega C_{\eta\eta})^2} \tag{B31}$$

$$Q = \frac{\omega C_{\eta\eta}}{(K_{\eta\eta} - M\omega^2)^2 + (\omega C_{\eta\eta})^2} \tag{B32}$$

Thus, replacing η by $(\eta - \eta_P)$ Eq. (B14) becomes:

$$\begin{aligned} dF_\xi &= -(K'_{\xi\xi} + i\omega C'_{\xi\xi})\xi - (K'_{\xi\eta} + i\omega C'_{\xi\eta})\,\eta \\ dF_\eta &= -(K'_{\eta\xi} + i\omega C'_{\eta\xi})\xi - (K'_{\eta\eta} + i\omega C'_{\eta\eta})\,\eta \end{aligned} \tag{B33}$$

where $K'_{\xi\xi}$, $C'_{\xi\xi}$ etc., are the spring and damping coefficients for the tilting pad and given by:

$$K'_{\xi\xi} = K_{\xi\xi} - (PK_{\xi\eta} + Q\omega C_{\xi\eta})K_{\eta\xi} - (QK_{\xi\eta} - P\omega C_{\xi\eta})\,\omega C_{\eta\xi} \tag{B34}$$

$$\omega C'_{\xi\xi} = \omega C_{\xi\xi} - (PK_{\xi\eta} + Q\omega C_{\xi\eta})\omega C_{\eta\xi} + (QK_{\xi\eta} - P\omega C_{\xi\eta})\,K_{\eta\xi} \tag{B35}$$

$$K'_{\xi\eta} = -M\omega^2\,(PK_{\xi\eta} + Q\omega C_{\xi\eta}) \tag{B36}$$

$$\omega C'_{\xi\eta} = M\omega^2(QK_{\xi\eta} - P\omega C_{\xi\eta}) \tag{B37}$$

$$K'_{\eta\xi} = -M\omega^2\,(PK_{\eta\xi} + Q\omega C_{\eta\xi}) \tag{B38}$$

$$\omega C'_{\eta\xi} = M\omega^2\,(QK_{\eta\xi} - P\omega C_{\eta\xi}) \tag{B39}$$

$$K'_{\eta\eta} = -M\omega^2\,(PK_{\eta\eta} + Q\omega C_{\eta\eta}) = -M\omega^2\,(1 + PM\omega^2) \tag{B40}$$

$$\omega C'_{\eta\eta} = M\omega^2\,(QK_{\eta\eta} - P\omega C_{\eta\eta}) = (M\omega^2)^2 Q \tag{B41}$$

If the pad has no inertia, i.e., $M = 0$, only $K'_{\xi\xi}$ and $\omega C'_{\xi\xi}$ remain as would be expected.

Bearing Spring and Damping Coefficients

Having determined the spring and damping coefficients for the individual tilting pads it remains to combine them into the overall bearing coefficients. The coordinate system for the bearing is the x-y system, see Fig. B1, with the coordinate transformation:

$$\begin{Bmatrix} \xi \\ \eta \end{Bmatrix} = - \begin{Bmatrix} \cos\psi & \sin\psi \\ -\sin\psi & \cos\psi \end{Bmatrix} \begin{Bmatrix} x \\ y \end{Bmatrix} \tag{B42}$$

$$\begin{Bmatrix} dF_x \\ dF_y \end{Bmatrix} = - \begin{Bmatrix} \cos\psi & -\sin\psi \\ \sin\psi & \cos\psi \end{Bmatrix} \begin{Bmatrix} dF_\xi \\ dF_\eta \end{Bmatrix} \tag{B43}$$

where dF_x and dF_y are the dynamic forces measured in the x-y system. The bearing spring and damping coefficients are defined by:

$$\begin{aligned} dF_x &= -K_{xx}x - C_{xx}\dot{x} - K_{xy}y - C_{xy}\dot{y} \\ dF_y &= -K_{yx}y - C_{yx}\dot{x} - K_{yy}y - C_{yy}\dot{y} \end{aligned} \tag{B44}$$

Thus, substituting Eq. (B42) and (B43) into Eq. (B33) and grouping terms in accordance with Eq. (B44) yields:

$$K_{xx} = K'_{\xi\xi}\cos^2\psi + K'_{\eta\eta}\sin^2\psi - (K'_{\xi\eta} + K'_{\eta\xi})\cos\psi\sin\psi \tag{B45}$$

$$\omega C_{xx} = \omega C'_{\xi\xi}\cos^2\psi + \omega C'_{\eta\eta}\sin^2\psi - (\omega C'_{\xi\eta} + \omega C'_{\eta\xi})\cos\psi\sin\psi \tag{B46}$$

$$K_{xy} = K'_{\xi\eta}\cos^2\psi - K'_{\eta\xi}\sin^2\psi + (K'_{\xi\xi} - K'_{\eta\eta})\cos\psi\sin\psi \tag{B47}$$

$$\omega C_{xy} = \omega C'_{\xi\eta}\cos^2\psi - \omega C'_{\eta\xi}\sin^2\psi + (\omega C'_{\xi\xi} - \omega C'_{\eta\eta})\cos\psi\sin\psi \tag{B48}$$

$$K_{yx} = K'_{\eta\xi}\cos^2\psi - K'_{\xi\eta}\sin^2\psi + (K'_{\xi\xi} - K'_{\eta\eta})\cos\psi\sin\psi \tag{B49}$$

$$\omega C_{yx} = \omega C'_{\eta\xi}\cos^2\psi - \omega C'_{\xi\eta}\sin^2\psi + (\omega C'_{\xi\xi} - \omega C'_{\eta\eta})\cos\psi\sin\psi \tag{B50}$$

$$K_{yy} = K'_{\eta\eta}\cos^2\psi + K'_{\xi\xi}\sin^2\psi + (K'_{\xi\eta} + K'_{\eta\xi})\cos\psi\sin\psi \tag{B51}$$

$$\omega C_{yy} = \omega C'_{\eta\eta}\cos^2\psi + \omega C'_{\xi\xi}\sin^2\psi + (\omega C'_{\xi\eta} + \omega C'_{\eta\xi})\cos\psi\sin\psi \tag{B52}$$

A summation over all the pads making up the bearing gives the bearing spring and damping coefficients. If the pads have no inertia the equations simplify to:

$$\begin{aligned}
K_{xx} &= K'_{\xi\xi}\cos^2\psi & \omega C_{xx} &= \omega C'_{\xi\xi}\cos^2\psi \\
K_{xy} &= K_{yx} = K'_{\xi\xi}\cos\psi\,\sin\psi & \omega C_{xy} &= \omega C_{yx} = \omega C'_{\xi\xi}\cos\psi\,\sin\psi \\
K_{yy} &= K'_{\xi\xi}\sin^2\psi & \omega C_{yy} &= \omega C'_{\xi\xi}\sin^2\psi
\end{aligned} \tag{B54}$$

Thus, for symmetry around the x-axis and no pad inertia, the cross-coupling terms disappear.

Pad Motion

The pad motion is given by Eq. (B30) which can also be written:

$$\eta_P = \frac{(K_{\eta\xi} + i\omega C_{\eta\xi})\xi + (K_{\eta\eta} + i\omega C_{\eta\eta})\eta}{K_{\eta\eta} - M\omega^2 + i\omega C_{\eta\eta}} \tag{B55}$$

Let $\eta_o = \eta_P$ for $M = 0$, i.e., for no pad inertia:

$$\eta_o = \eta + \frac{K_{\eta\xi} + i\omega C_{\eta\xi}}{K_{\eta\eta} + i\omega C_{\eta\eta}}\,\xi \tag{B56}$$

Then:

$$\frac{\eta_P}{\eta_o} = \frac{K_{\eta\eta} + i\omega C_{\eta\eta}}{K_{\eta\eta} - M\omega^2 + i\omega C_{\eta\eta}} = 1 + \frac{M\omega^2}{K_{\eta\eta} - M\omega^2 + i\omega C_{\eta\eta}} = 1 + PM\omega^2 - iQM\omega^2 \tag{B57}$$

or:

$$\left|\frac{\eta_P}{\eta_o}\right| = \sqrt{(1 + PM\omega^2)^2 + (QM\omega^2)^2} \tag{B58}$$

$$\arg(\eta_o) - \arg(\eta_P) = \tan^{-1}\left(\frac{QM\omega^2}{1+PM\omega^2}\right) = \tan^{-1}\left(\frac{\omega C_{\eta\eta}M\omega^2}{K_{\eta\eta}(K_{\eta\eta}-M\omega^2)+(\omega C\eta\eta)^2}\right) \tag{B59}$$

Equation (B58) gives the amplitude ratio, i.e., the magnification factor, and Eq. (B59) gives the phase angle lag with respect to a inertialess pad. Thus, the two equations indicate how well the pad follows the shaft motion. The phase angle becomes 90° when:

$$M_{crit}\omega^2 = \frac{K_{\eta\eta}^2 + (\omega C_{\eta\eta})^2}{K_{\eta\eta}}$$

Hence, if the pad mass satisfies Eq. (B60) there will be a resonance of the pad motion.

It is convenient to use Eq. (B60) to establish a value for M, designated the critical mass. In dimensionless form Eq. (B60) may be written:

$$\frac{CWM_{crit}}{\left[\mu DL\left(\frac{R}{C}\right)^2\right]^2} = \frac{1}{4\pi^2 S}\,\frac{\left(\frac{CK_{\eta\eta}}{W}\right)^2 + \left(\frac{C\omega C_{\eta\eta}}{W}\right)^2}{\frac{CK_{\eta\eta}}{W}}$$

where S is the bearing Sommerfeld number.

NOMENCLATURE FOR APPENDIX B

C		Pad clearance (radius of curvature of pad minus journal radius) inch
C'		Pivot circle clearance (radius of pivot circle minus journal radius) inch
$C_{xx}, C_{xy}, C_{yx}, C_{yy}$		Bearing damping coefficients, lbs sec/in.
$C_{\xi\xi}, C_{\xi\eta}, C_{\eta\xi}, C_{\eta\eta}$		Fixed pad damping coefficients, lbs sec/in.
$C'_{\xi\xi}, C'_{\xi\eta}, C'_{\eta\xi}, C'_{\eta\eta}$		Tilting pad damping coefficients, lbs.sec/in.
D		Journal diameter, inch
e		Journal center eccentricity with respect to pad center, inch
e_o		Journal center eccentricity with respect to bearing center, inch
F		Load on pad, lbs.
F_r, F_t		Radial and tangential components of pad load, lbs.
F_ξ, F_η		Components in ξ and η-direction of pad load, lbs. (see Fig.1)
f	=	$F/\lambda\omega$, dimensionless pad force
f_r, f_t		Radial and tangential components of dimensionless pad force
f_ξ, f_η		Components in ξ and η-direction of dimensionless pad force
I		Transverse mass moment of inertia of shoe around pivot, lbs. in.sec^2.
$K_{xx}, K_{xy}, K_{yx}, K_{yy}$		Bearing spring coefficients, lbs/in.
$K_{\xi\xi}, K_{\xi\eta}, K_{\eta\xi}, K_{\eta\eta}$		Fixed pad spring coefficients, lbs/in.
$K'_{\xi\xi}, K'_{\xi\eta}, K'_{\eta\xi}, K'_{\eta\eta}$		Tilting pad spring coefficients, lbs/in.
L		Bearing length, inch
M	=	I/R_p^2, equivalent pad mass, lbs.sec^2/in.
M_{crit}		Value of equivalent of pad mass to cause pad motion resonance, lbs.sec^2/in.
N		Rotational speed of journal, RPS
P, Q		Coefficients defined by Eqs. (B31) and(B32)
R		Journal radius, inch

R_P		Radius from pad center to actual pivot point of pad, inch
S	=	$(\mu NDL/W) \cdot (R/C)^2$, bearing Sommerfeld number.
S_P	=	$(\mu NDL/F) \cdot (R/C)^2$, pad Sommerfeld number.
W		Bearing load, lbs.
x,y		Coordinates of journal center with respect to the bearing, see Fig. 1, inch.
ϵ	=	e/C, eccentricity ratio with respect to the pad center.
ϵ_o	=	e_o/C, eccentricity ratio with respect to the bearing center.
η_o		Amplitude of the center of a massless pad, inch.
η_P		Amplitude for pad center motion, see Fig. 1 inch.
λ	=	$(\mu RL/\pi) \cdot (R/C)^2$ bearing coefficient
μ		Lubricant viscosity, lbs.sec/in^2.
ξ,η		Coordinates of journal center with respect to the pad, see Fig. 1
ϕ		Attitude angle with respect to the pad load line, radians
ϕ_o		Attitude angle with respect to the bearing load line, radians
ψ		Angle from vertical (negative x-axis) to pad pivot point, see Fig. 1. inch.
ω		Angular speed of shaft, radian/sec.

APPENDIX C

DESIGN DATA FOR THE THREE-PAD BEARING

The basic data for the individual tilting pad with β = 100 degrees, θ_p = 0.5 was available from the previous work on the single partial-arc bearing (Ref. 7). This has been combined to give design data for the three-pad bearing for values of m of 0.5 and 0 (Tables C-1 and C-2 respectively). There are relatively few data points for the zero preload bearing but the dependent variables appear to vary regularly and smoothly with ϵ_B so that interpolation should be reasonable. The friction and flow were not included in the earlier computations so they are not available for the composite bearing.

TABLE C-1

DESIGN DATA FOR THE THREE-PAD TILTING-PAD BEARING

(a) β = 100 degrees, θ_p = 0.5, m = 0.5

(b) Static load line passes through top pad pivot and bisects the angle between the bottom pad pivots

ϵ_B	S	$\frac{C_p}{W} K_{xx}$	$\frac{C_p}{W} K_{yy}$	$\frac{\omega C_p}{W} B_{xx}$	$\frac{\omega C_p}{W} B_{yy}$	$\frac{C_p W M_{crit}}{\left[\mu DL(\frac{R}{C_p})^2\right]^2}$
Laminar						
.01	2.89	62.3	67.7	88.7	92.4	.0723*
.05	.605	11.9	16.3	17.3	21.1	.276*
.1	.315	5.82	10.2	8.62	12.3	.402*
.2	.163	3.22	7.65	4.49	8.31	.498*
.4	.0732	2.78	8.16	2.71	6.78	.578*
.5	.050	3.15	9.44	2.17	6.51	15.8
.6	.035	4.00	12.0	21.6	6.47	32.3
Re = 1663						
.01	2.16	65.1	69.3	91.8	95.4	.135*
.05	.451	12.3	16.5	18.0	21.6	.530*
.1	.234	5.93	10.1	8.90	12.4	.790*
.2	.121	3.16	7.35	4.63	8.24	1.02*
.4	.055	2.56	7.47	2.72	6.49	1.38*
.5	.038	2.84	8.51	2.04	6.13	26.0
.6	.027	3.61	10.8	2.04	6.11	49.5
Re = 2378						
.01	1.90	60.1	64.0	92.3	95.8	.174*
.05	.398	11.4	15.2	18.1	21.6	.685*
.1	.205	5.51	9.30	8.96	12.4	1.02*
.2	.106	3.00	6.92	4.64	8.12	1.36*
.4	.049	2.48	7.21	2.67	6.30	1.84*
.5	.034	2.74	8.22	1.98	5.93	32.4
.6	.025	3.48	10.4	1.98	5.92	60.9
Re = 3326						
.01	1.65	58.9	62.8	93.2	96.5	.235*
.05	.344	11.1	14.9	18.4	21.6	.931*

*This is the critical mass for the top pad, the value for bottom pad is greater. At high eccentricity, the top pad becomes unloaded and then the bottom pad critical mass is given.

TABLE C-1 – Concluded

ϵ_B	S	$\frac{C_p}{W} K_{xx}$	$\frac{C_p}{W} K_{yy}$	$\frac{\omega C_p}{W} B_{xx}$	$\frac{\omega C_p}{W} B_{yy}$	$\frac{C_p W M_{crit}}{\left[\mu DL\left(\frac{R}{C_p}\right)^2\right]^2}$
.1	.178	5.33	9.14	9.08	12.4	1.42*
.2	.092	3.01	6.95	4.62	7.96	1.90*
.4	.042	2.45	7.11	2.64	6.21	2.54*
.5	.029	2.63	7.89	1.99	5.98	42.9
.6	.022	3.23	9.69	2.09	6.27	82.2
Re = 5820						
.01	1.24	62.0	65.1	95.0	98.2	.429*
.05	.258	11.9	15.0	18.7	21.9	1.71*
.1	.133	5.82	8.95	9.20	12.4	2.63*
.2	.069	2.94	6.60	4.64	7.87	3.50*
.4	.032	2.33	6.79	2.61	6.03	4.78*
.5	.022	2.52	7.56	1.95	5.86	75.3
.6	.016	3.11	9.34	2.10	6.30	138.
Re = 8314						
.01	1.00	50.2	54.1	97.3	100.	.614*
.05	.209	9.34	13.1	19.2	22.5	2.50*
.1	.108	4.53	8.23	9.45	12.8	3.97*
.2	.056	2.65	6.35	4.80	8.01	5.53*
.4	.026	2.27	6.62	2.58	5.95	7.43*
.5	.018	2.44	7.32	1.91	5.74	115.
.6	.014	3.01	9.03	2.06	6.16	208.
Re = 13,304						
.01	.749	62.8	66.3	96.8	100.	1.16*
.05	.156	12.0	15.3	19.1	22.3	4.69*
.1	.080	5.78	9.16	9.39	12.6	7.37*
.2	.041	2.93	6.56	4.74	7.94	10.1*
.4	.019	2.21	6.40	2.65	5.99	14.6*
.5	.014	2.33	7.02	1.93	5.78	208.
.6	.010	2.88	8.65	2.07	6.21	368.

*This is the critical mass for the top pad, the value for bottom pad is greater. At high eccentricity, the top pad becomes unloaded and then the bottom pad critical mass is given.

TABLE C-2

DESIGN DATA FOR THE THREE-PAD TILTING-PAD BEARING

(a) β = 100 degrees, θ_p = 0.5, m = 0

(b) Static load line passes through the top pad pivot and bisects the angle between the bottom pad pivots

ϵ_B	S	$\frac{C_p}{W} K_{xx}$	$\frac{C_p}{W} K_{yy}$	$\frac{\omega C_p}{W} B_{xx}$	$\frac{\omega C_p}{W} B_{yy}$	$\frac{C_p W M_{crit.}}{\left[\mu DL\left(\frac{R}{C_p}\right)^2\right]^2}$ *
Laminar Flow						
.02	.200	1.56	4.68	2.13	6.39	1.13
.1	.182	1.63	4.89	2.10	6.32	1.39
.2	.160	1.72	5.17	2.08	6.26	1.81
.4	.123	1.93	5.78	2.10	6.29	3.01
.8	.697	2.59	7.77	2.15	6.45	8.63
Re = 1663						
.02	.136	1.45	4.34	1.99	5.97	2.33
.1	.124	1.51	4.53	1.98	5.93	2.81
.2	.111	1.59	4.78	1.96	5.89	3.57
.4	.087	1.76	5.30	1.98	5.94	5.65
.8	.051	2.34	7.02	2.03	6.09	14.9
Re = 2378						
.02	.116	1.31	3.92	1.96	5.87	3.06
.1	.107	1.36	4.10	1.94	5.82	3.69
.2	.096	1.44	4.33	1.93	5.78	4.68
.4	.076	1.64	4.93	1.93	5.79	7.29
.8	.045	2.25	6.75	1.97	5.89	18.8
Re = 3326						
.02	.099	1.26	3.77	1.93	5.80	4.21
.1	.091	1.32	3.96	1.91	5.73	5.05
.2	.082	1.40	4.21	1.89	5.67	6.36
.4	.065	1.62	4.86	1.87	5.62	9.76
.8	.039	2.21	6.62	1.93	5.78	24.8

*Values of critical mass are for the bottom, loaded, pads in all cases since the top pad is always unloaded when ϵ_B is finite.

TABLE C-2 — Concluded

ϵ_B	S	$\frac{C_p}{W} K_{xx}$	$\frac{C_p}{W} K_{yy}$	$\frac{\omega C_p}{W} B_{xx}$	$\frac{\omega C_p}{W} B_{yy}$	$\frac{C_p W M_{crit.}}{\left[\mu DL\left(\frac{R}{C_p}\right)^2\right]^2}$ *
Re =	5820					
.02	.072	1.27	3.80	1.91	5.73	7.87
.1	.067	1.29	3.88	1.89	5.66	9.37
.2	.060	1.34	4.02	1.86	5.58	11.7
.4	.048	1.54	4.61	1.83	5.49	17.9
.8	.029	2.10	6.31	1.87	5.60	44.8
Re =	8314					
.02	.058	1.04	3.12	1.94	5.82	11.3
.1	.053	1.12	3.35	1.92	5.77	13.4
.2	.048	1.22	3.67	1.90	5.71	16.7
.4	.039	1.47	4.40	1.85	5.55	26.1
.8	.024	2.04	6.13	1.84	5.51	68.6
Re =	13,304					
.02	.042	1.25	3.76	1.89	5.68	21.7
.1	.039	1.29	3.87	1.87	5.62	25.7
.2	.035	1.35	4.04	1.85	5.55	31.9
.4	.028	1.51	4.52	1.82	5.46	49.4
.8	.0178	1.97	5.92	1.85	5.54	126.

*Values of critical mass are for the bottom, loaded, pads in all cases since the top pad is always unloaded when ϵ_B is finite.

REFERENCES

1. Taylor, G. I.: Stability of a Viscous Liquid Contained Between Two Rotating Cylinders. Phil. Trans. Roy. Sec. (London), series A, vol. 223, 1923.

2. Smith, M. I.; and Fuller, D. D.: Journal Bearing Operation at Superlaminar Speeds. ASME, vol. 78, 1956.

3. Vohr, J. H.: Analysis of Turbulent Lubrication. Vol 2. An Experimental Study of Vortex Flow and Turbulence in Concentric and Eccentric Annuli. Mechanical Technology Incorporated report no. MTI-64TR20. Final Report to NASA on Contract NASw-771, May 1964.

4. DiPrima, R. C.: A Note on the Stability of Flow in Non-Concentric Annuli. Mechanical Technology Incorporated report no. MTI-62TR15, August 1962.

5. Ng, C. W.; and Pan, C. H. T.: A Linearized Turbulent Lubrication Theory. ASME Paper 64-Lub-29. Presented at the International Lubrication Conference, (Washington, D.C.), October, 1964.

6. Arwas, E. B.; Orcutt, F. K.; and Vohr, J. H.: Second Quarterly Report - Lubrication Analysis in Turbulent Regime. NASA Contract NASw-771, January 1964.

7. Orcutt, F. K.: and Arwas, E. B.: Analysis of Turbulent Lubrication. Vol. 1. The Static and Dynamic Properties of Journal Bearings in Laminar and Turbulent Regimes. Mechanical Technology Incorporated report no. MTI-64TR19. NASA CR 54034 Final Report to NASA on Contract NASw-771, May 1964.

8. Elrod, H. G.; Ng, C. W.; and Pan, C. H. T.: A Theory for Turbulent Fluid Films and Its Application to Bearings. Mechanical Technology Incorporated report no. MTI-65TR9, March 1965.

9. Raimondi, A. A.; and Boyd, J.: A Solution for the Finite Journal Bearing and Its Application to Analysis and Design: III. Trans. ASLE, vol. 1, no. 1, 1958.

10. Theodorsen, T.; and Reiger, A.: Experiments on Drag of Revolving Disks, Cylinders and Streamline Rods at High Speeds. NACA report no. 793, Thirtieth Annual Report, 744-803, 1944.

11. Lund, J. W.: Spring and Damping Coefficients for the Tilting-Pad Journal Bearing. ASLE Paper 64AM-2B3. Presented at the Annual Meeting (Chicago), May 1964.

12. Prohl, M. A.: A General Method for Calculating Critical Speed of Flexible Rotors. Trans. ASME, 1945, pp. A142-A148.

13. Malanoski, S. B.: and Lewis, P.: Rotor-Bearing Dynamics Technology. Part IV - Ball Bearing Design Data. AFAPL-TR65-45. (Also available as Mechanical Technology Incorporated Report no. MTI-65TR35, July 1965.)

14. Pinkus, O.: and Sternlicht, B.: Theory of Hydrodynamic Lubrication. McGraw-Hill Book Co., Inc., 1961.

15. Warner, P.C., "Static and Dynamic Properties of Partial Journal Bearings," ASME paper 62-LubS-11, presented at the Lubrication Symposium, Miami, 1962.

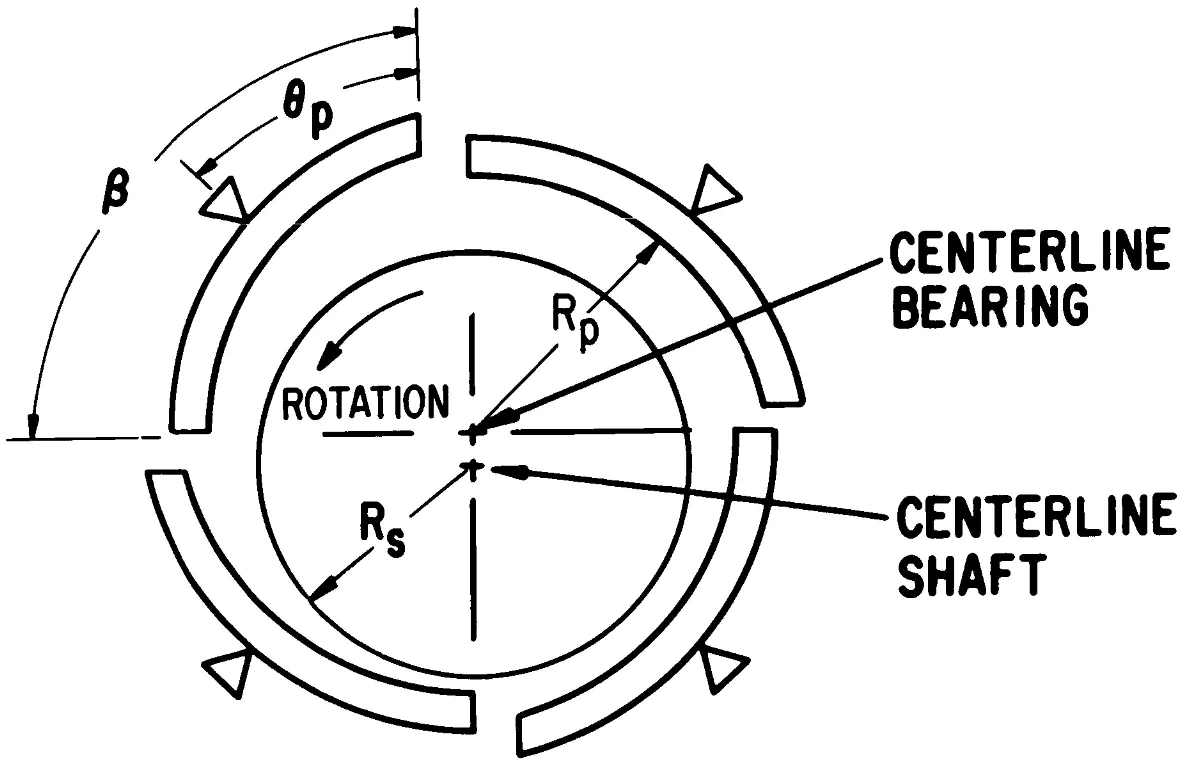

Figure 1. - Schematic of tilting-pad bearing.

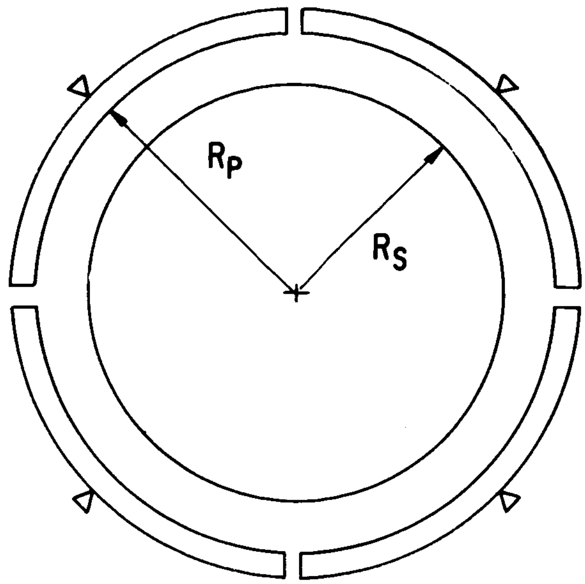

4 PAD BEARING
ZERO PRELOAD
(a)

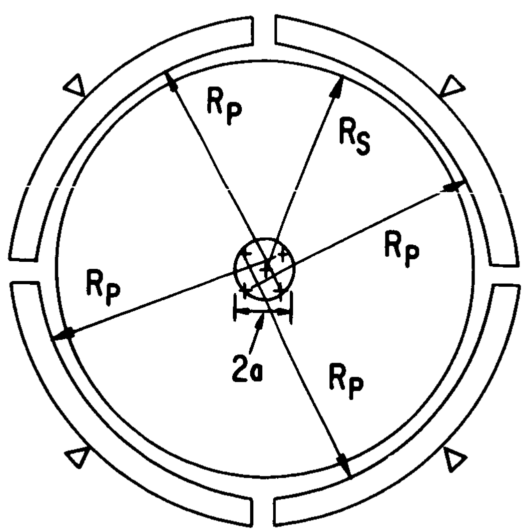

4 PAD BEARING
PRELOAD = a

(PRELOAD COEFFICIENT $= \frac{a}{R_P - R_S}$)

(b)

Figure 2. - Geometrical arrangement of pads.

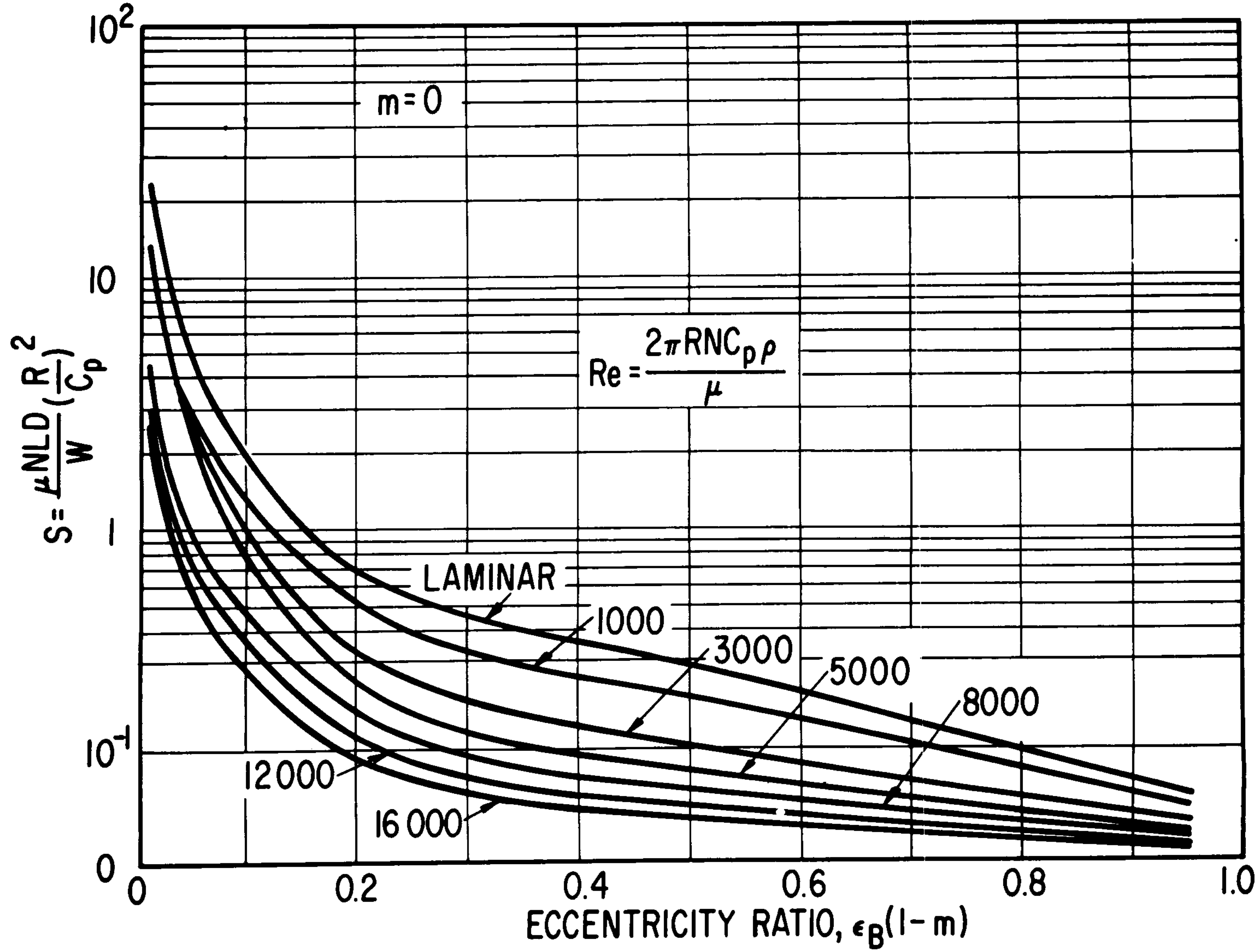

Figure 3. - Calculated static load capacity - m = 0. 4 Pads, $\beta = 80^o$, $\theta_p = 0.55$, L/D = 1.0.

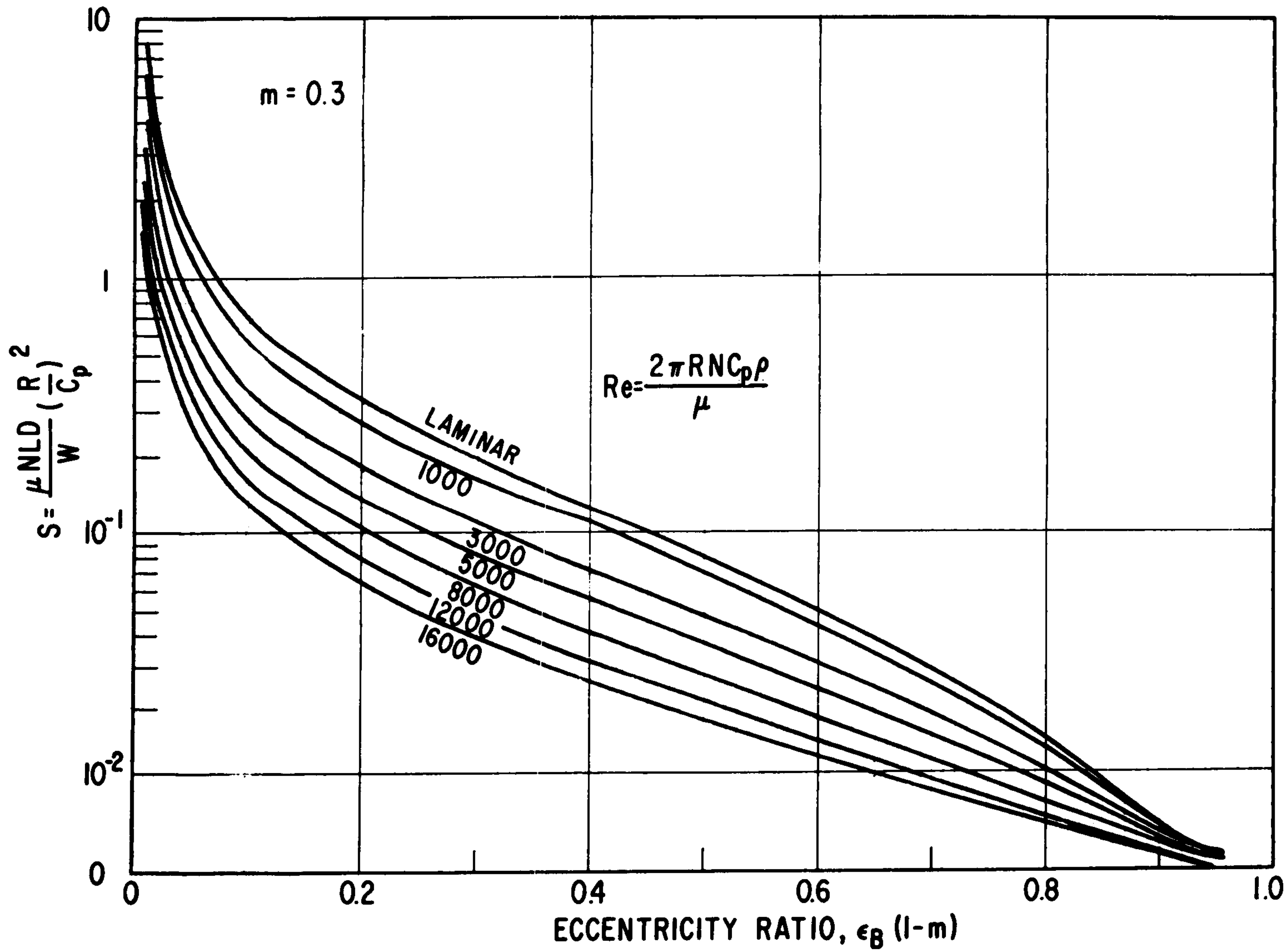

Figure 4. - Calculated static load capacity - m = 0.3. 4 Pads, $\beta = 80^{\circ}$, $\theta_p = 0.55$, L/D = 1.0.

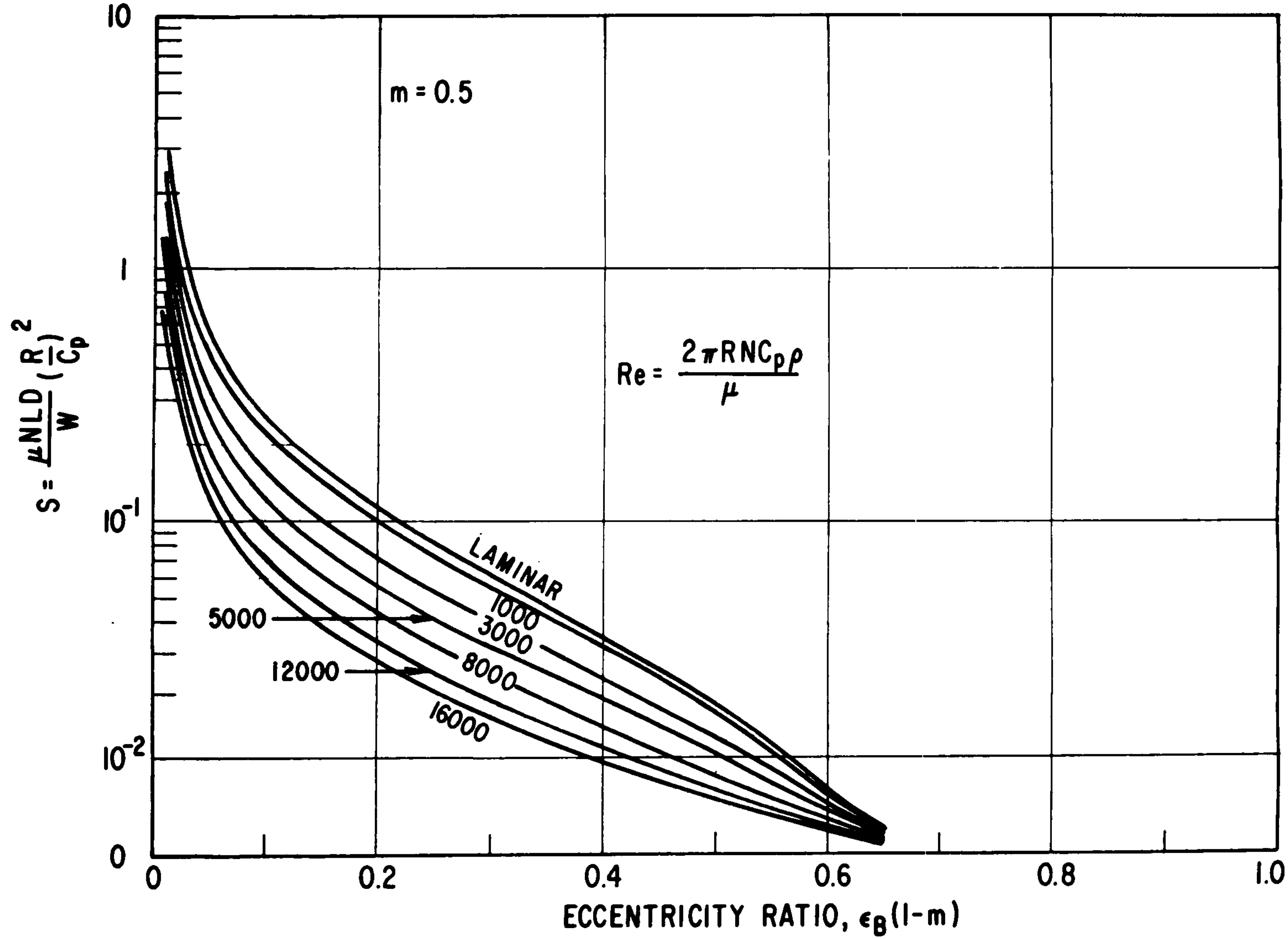

Figure 5. - Calculated static load capacity - m = 0.5. 4 Pads, $\beta = 80^\circ$, $\theta_p = 0.55$, $L/D = 1.0$.

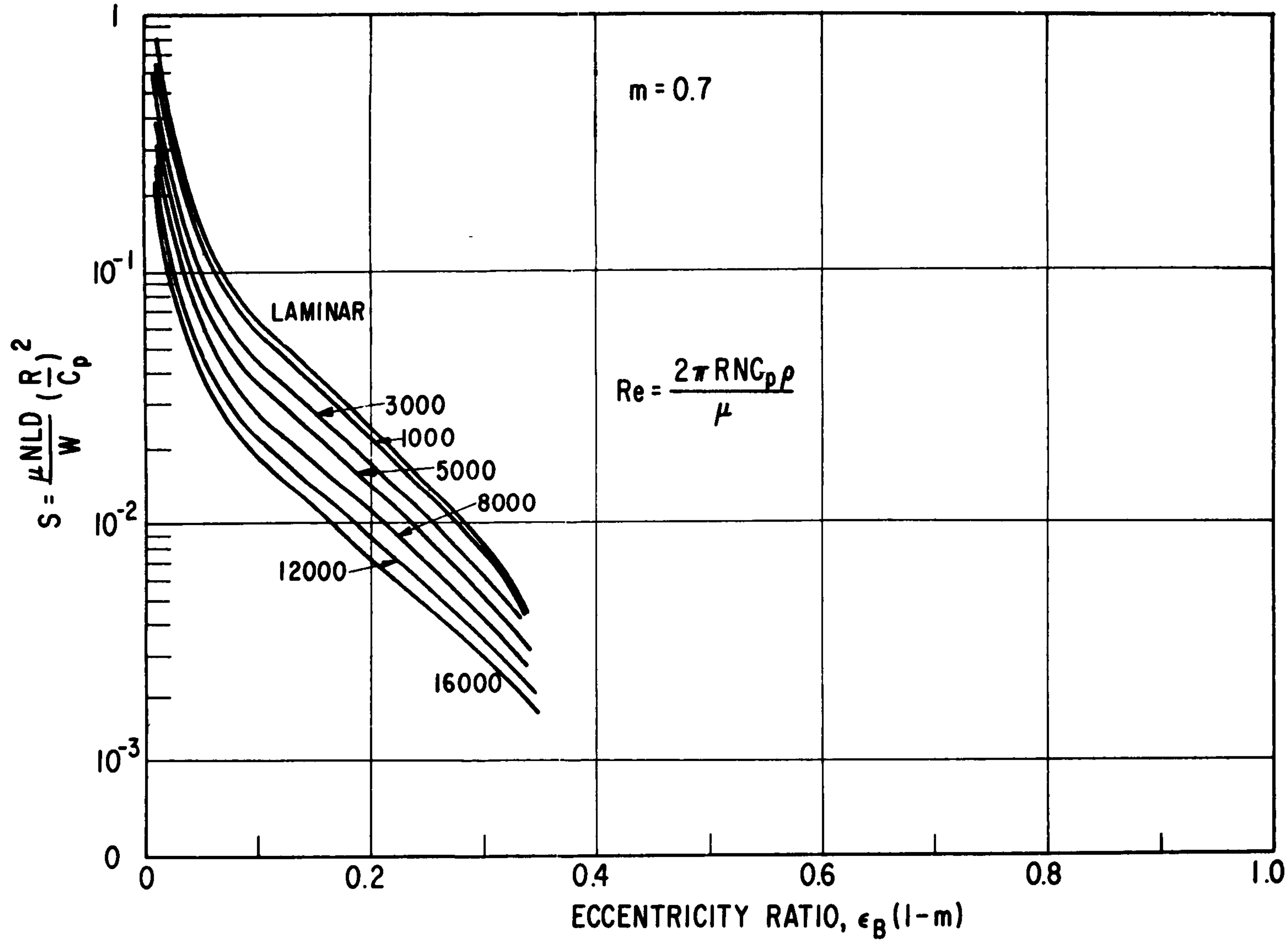

Figure 6. - Calculated static load capacity - m = 0.7. 4 Pads, $\beta = 80^{\circ}$, $\theta_p = 0.55$, L/D = 1.0.

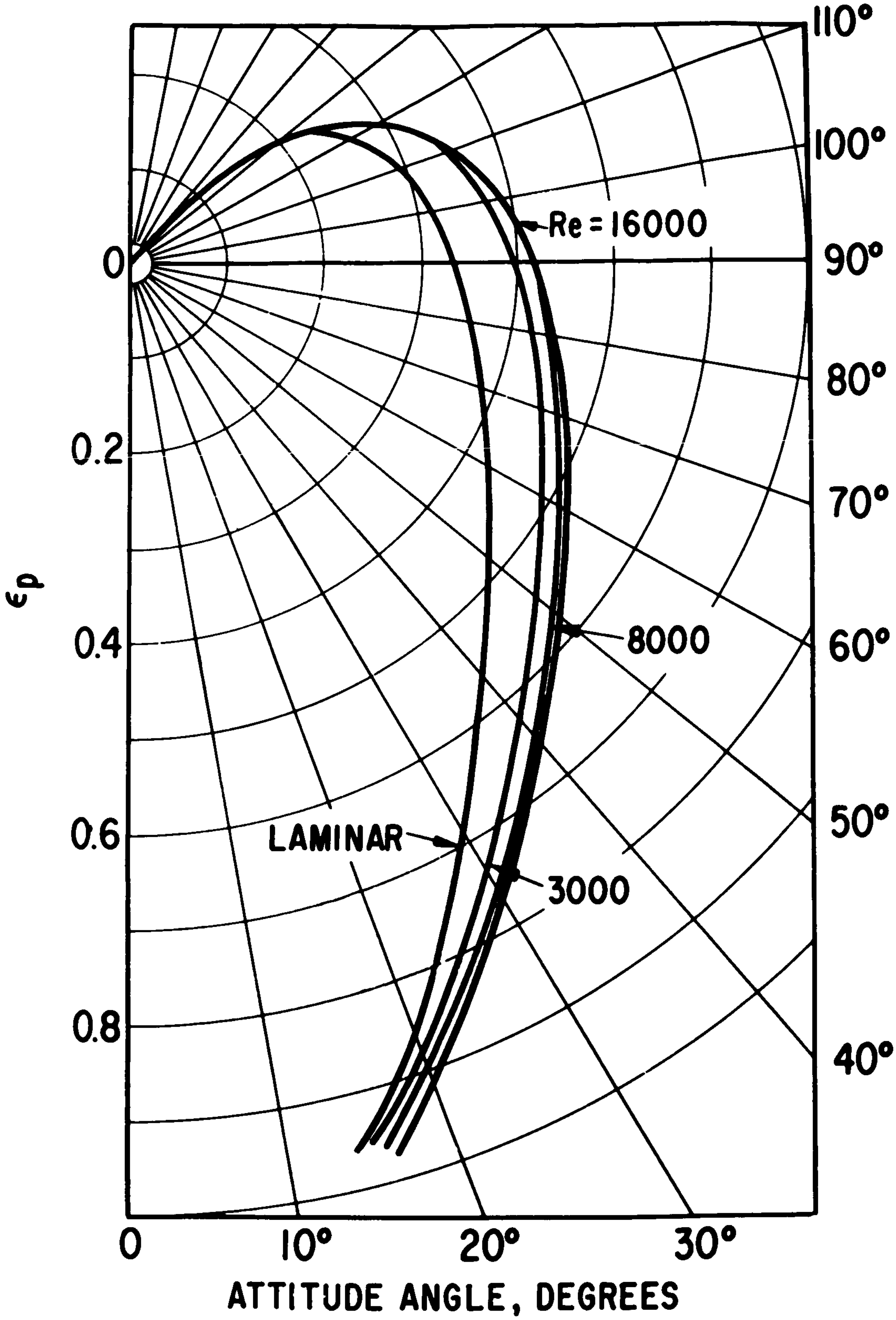

Figure 7. - Attitude angle versus eccentrictiy for single pad.
$\beta = 80^{\circ}$, $\theta_p = 0.55$, L/D = 1.0.

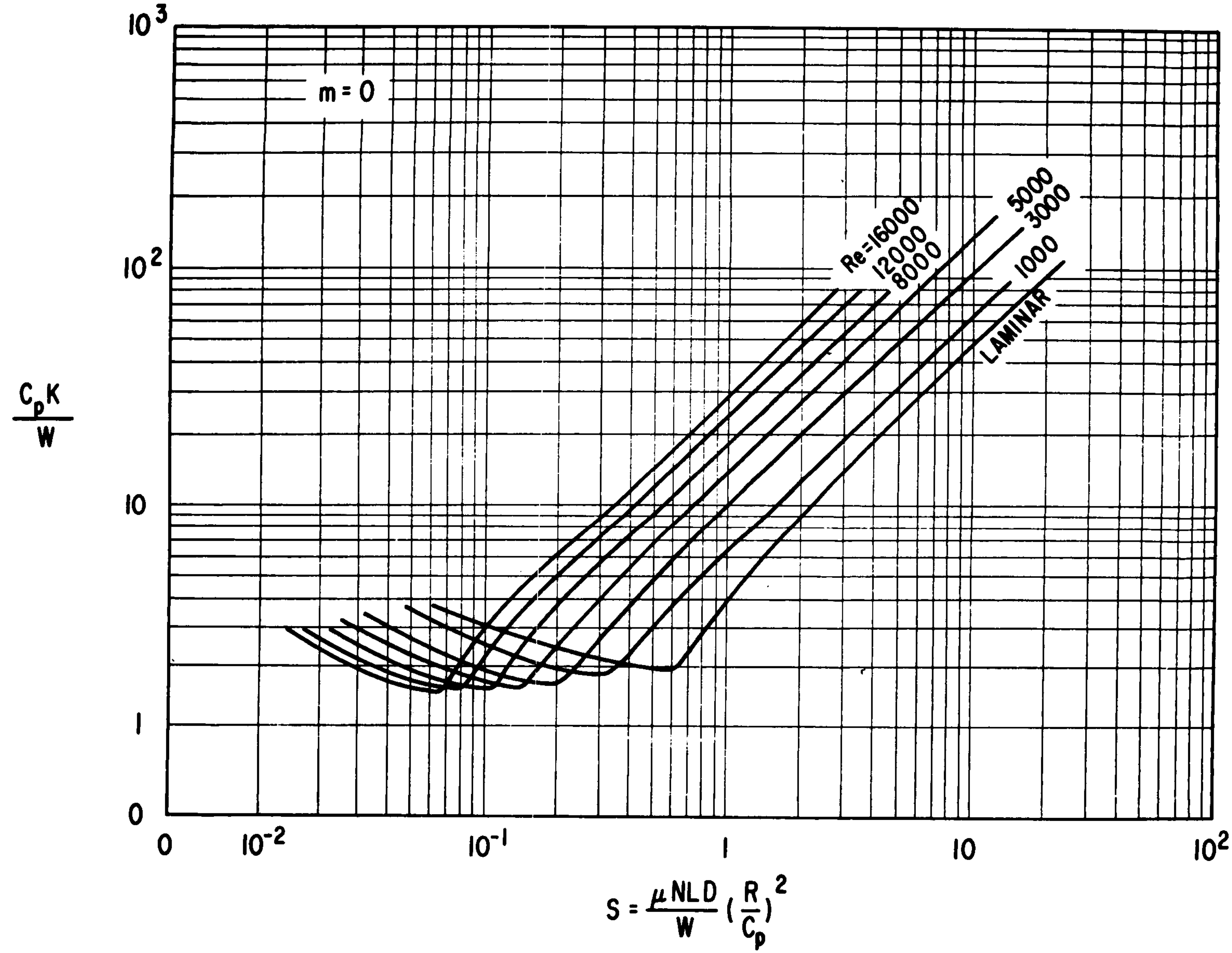

Figure 8. - Stiffness coefficient versus Sommerfeld number - m = 0. 4 Pads, $\beta = 80^o$, $\theta_p = 0.55$, L/D = 1.0.

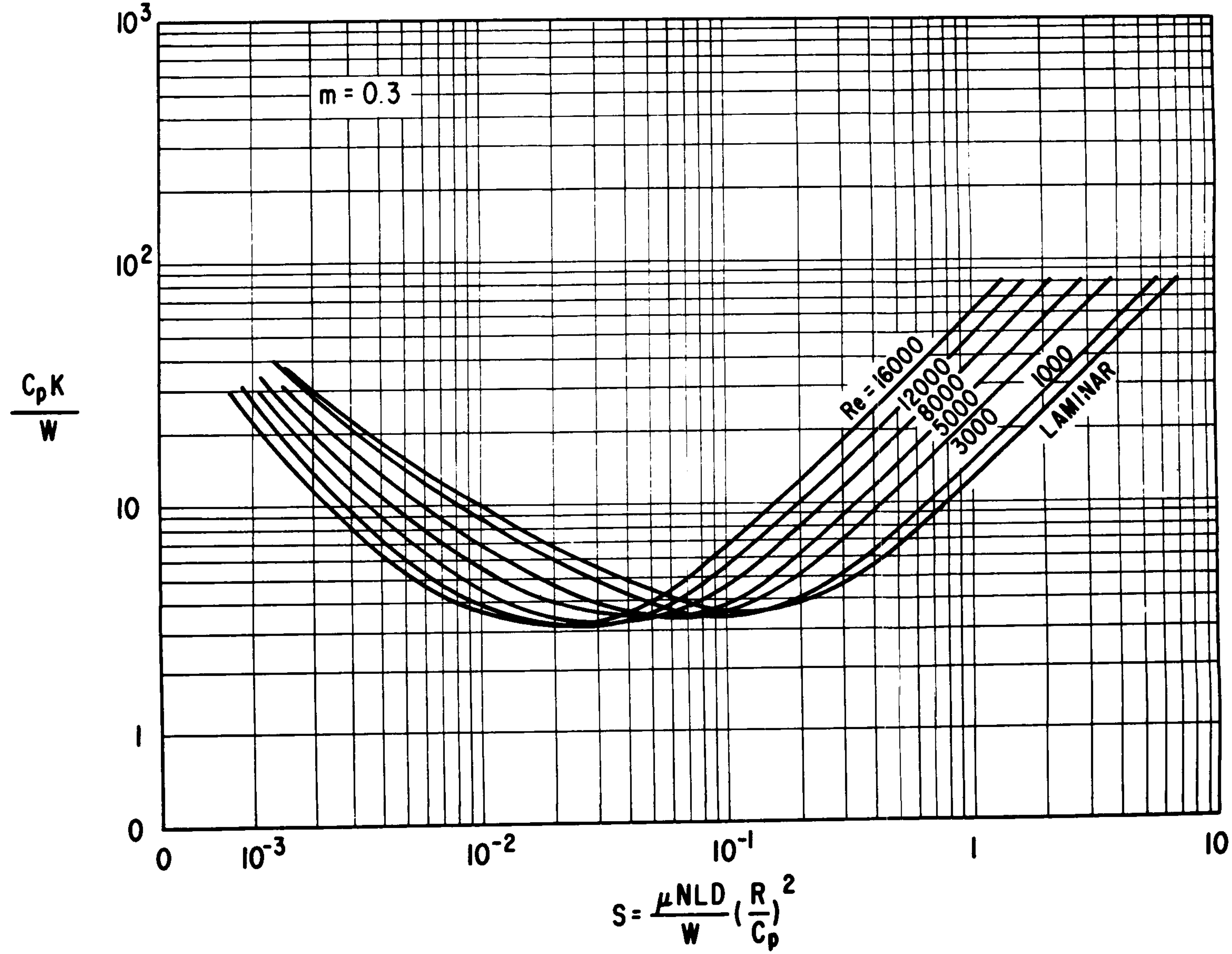

Figure 9. - Stiffness coefficient versus Sommerfeld number - m = 0.3. 4 Pads, $\beta = 80^\circ$, $\theta_p = 0.55$, L/D = 1.0.

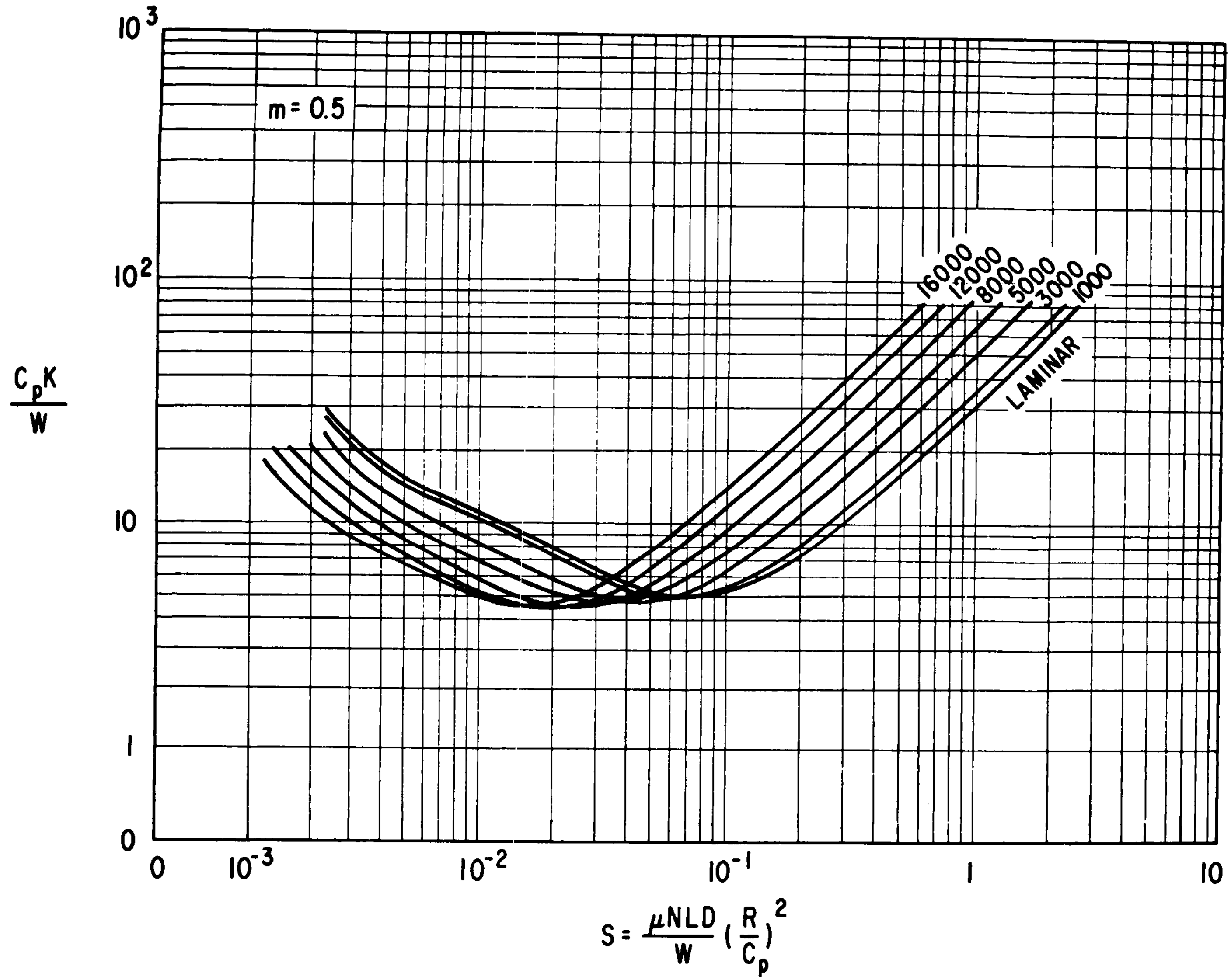

Figure 10. - Stiffness coefficient versus Sommerfeld number - m = 0.5. 4 Pads, $\beta = 80^{\circ}$, $\theta_p = 0.55$, L/D = 1.0.

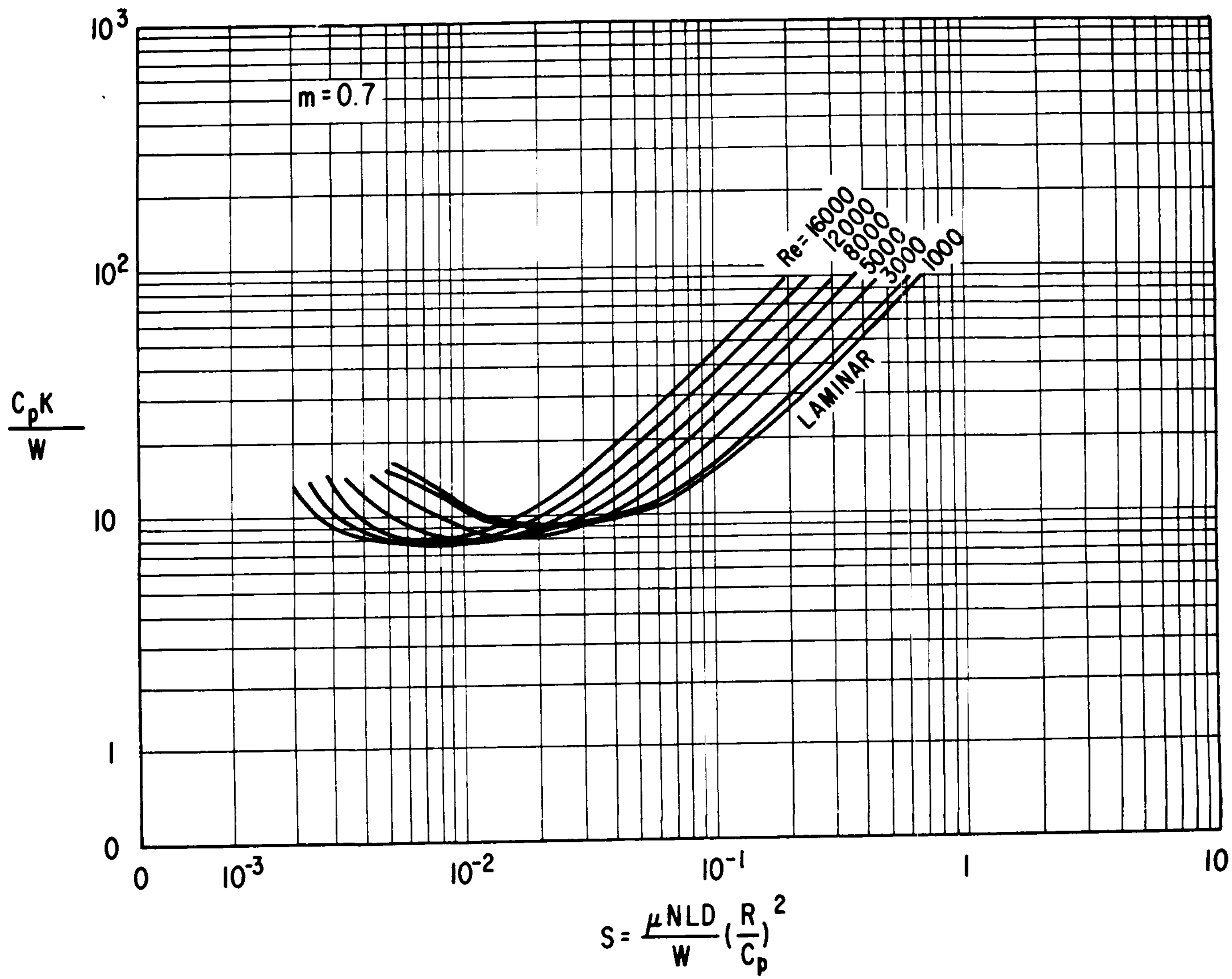

Figure 11. - Stiffness coefficient versus Sommerfeld number - m = 0.7. 4 Pads, $\beta = 80^o$, $\theta_p = 0.55$, L/D = 1.0.

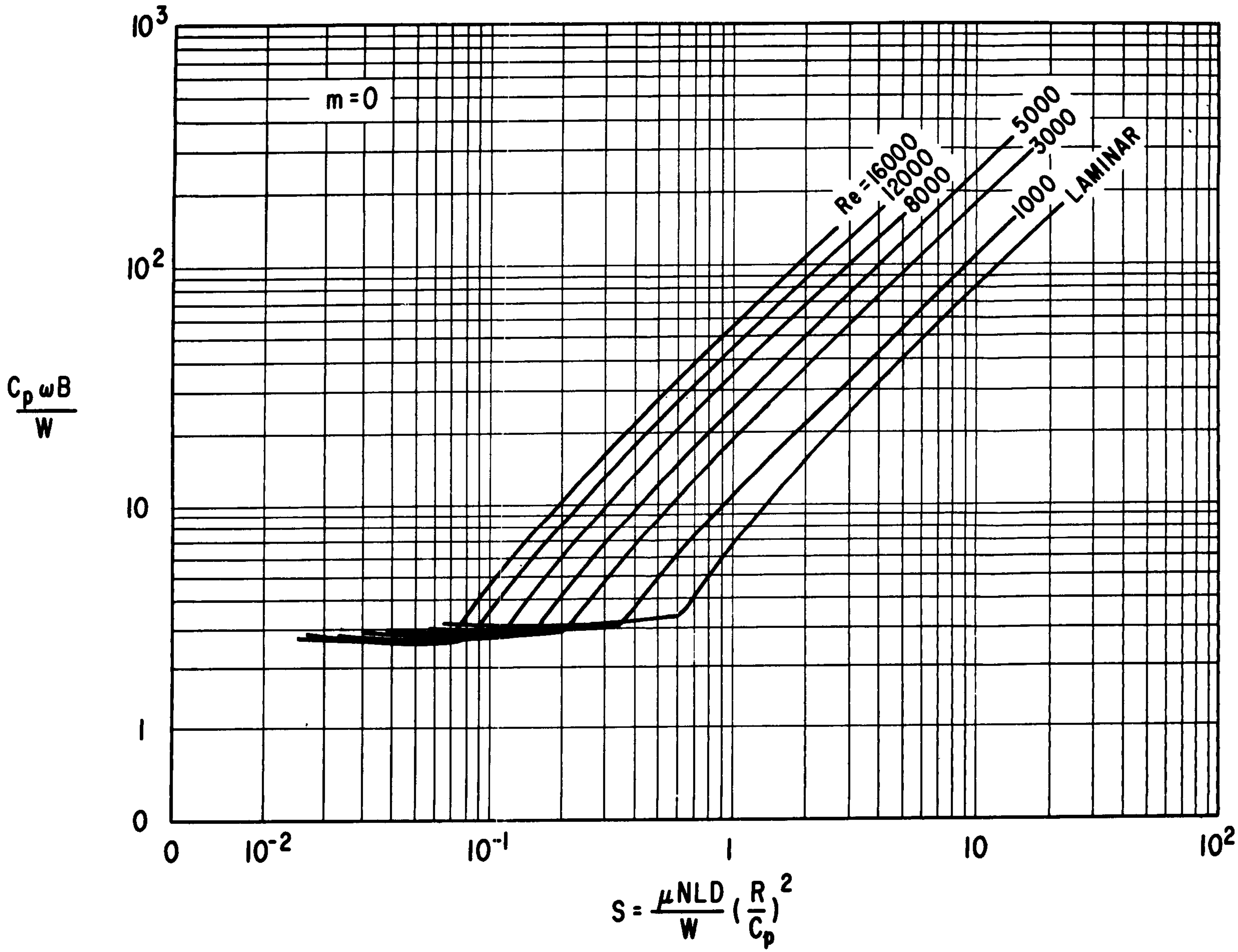

Figure 12. - Damping coefficient versus Sommerfeld number - m = 0. 4 Pads, $\beta = 80^{\circ}$, $\theta_p = 0.55$, L/D = 1.0.

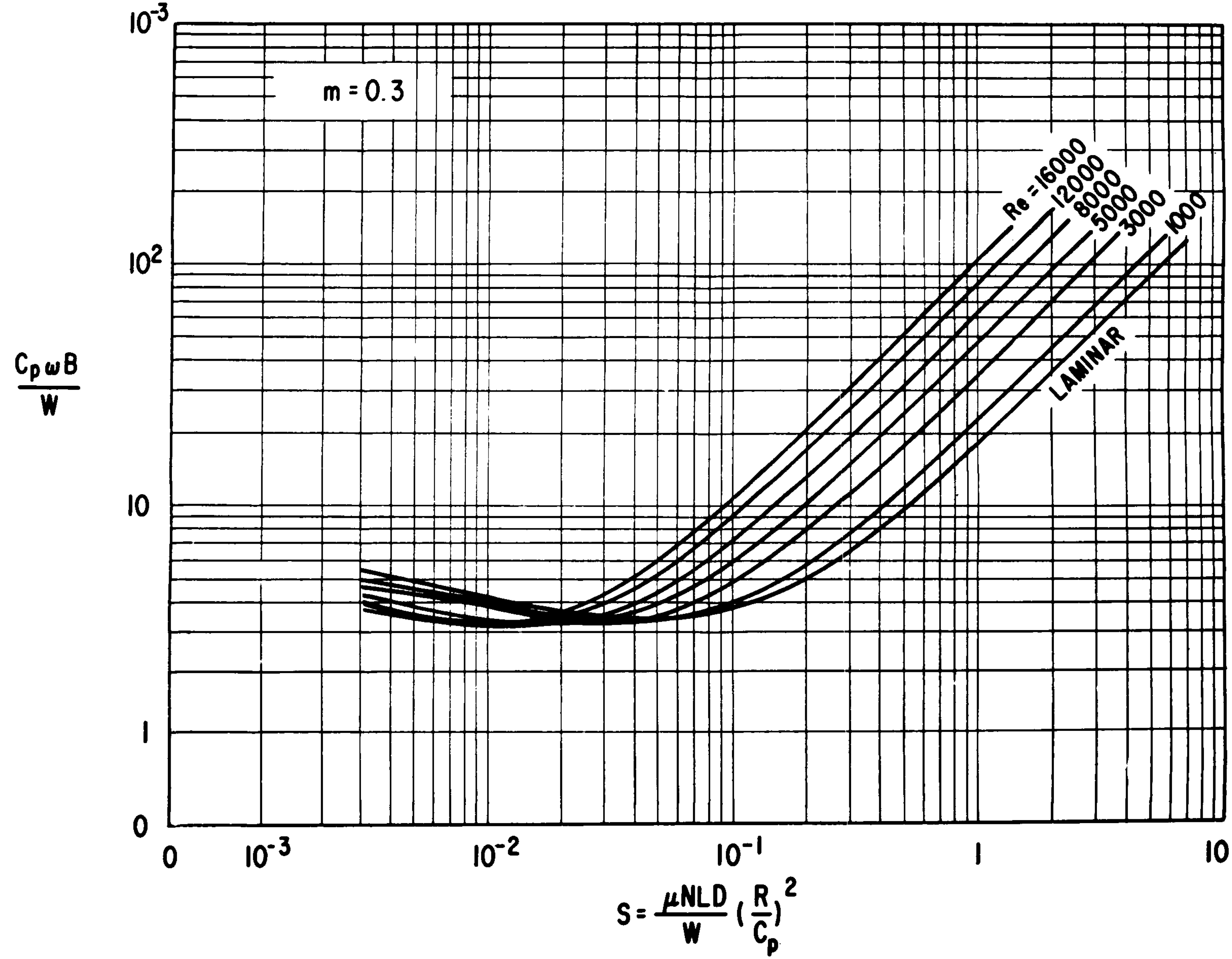

Figure 13. - Damping coefficient versus Sommerfeld number - m = 0.3. 4 Pads, $\beta = 80^{\circ}$, $\theta_p = 0.55$, L/D = 1.0.

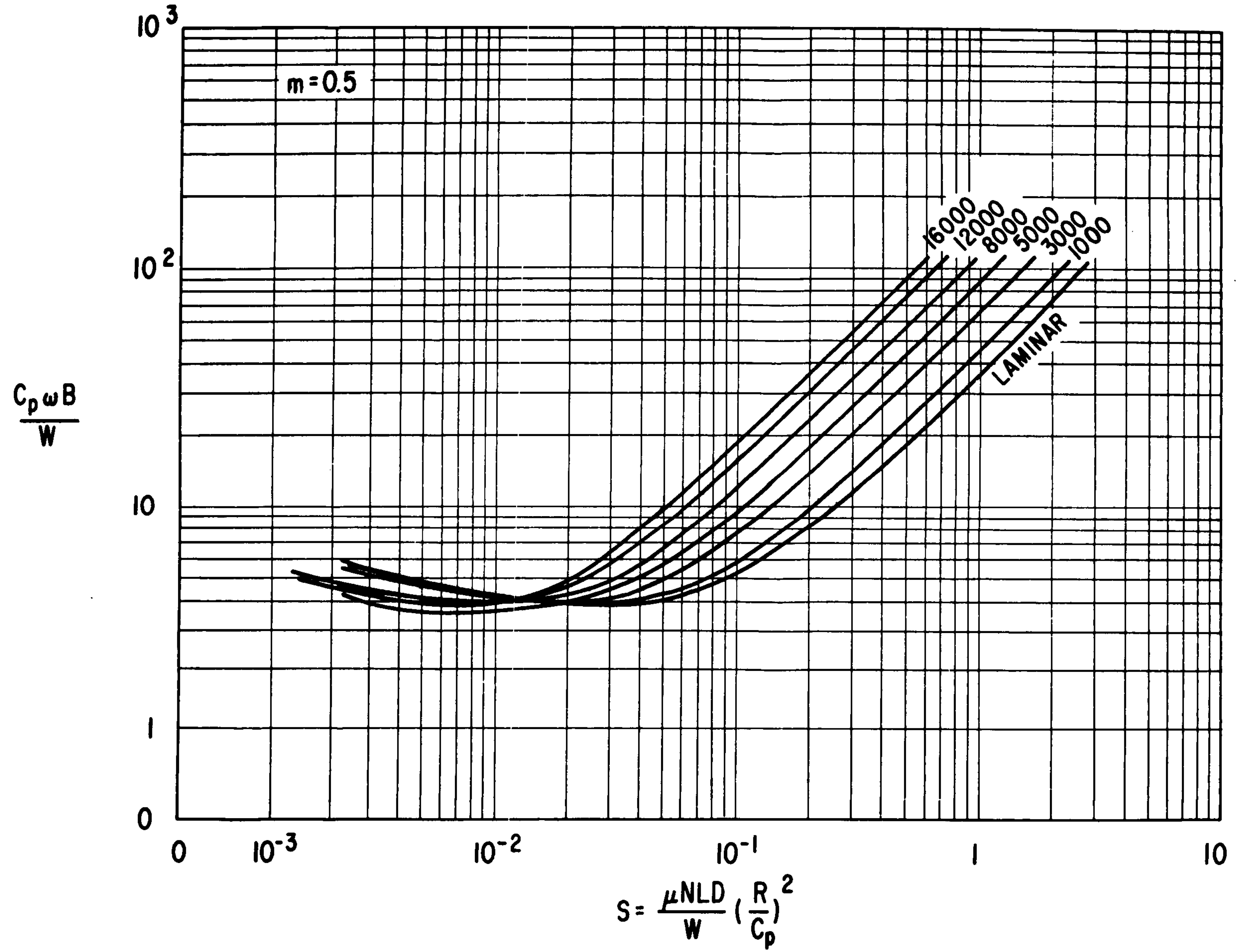

Figure 14. - Damping coefficient versus Sommerfeld number - m = 0.5. 4 Pads, $\beta = 80^{\circ}$, $\theta_p = 0.55$, L/D = 1.0.

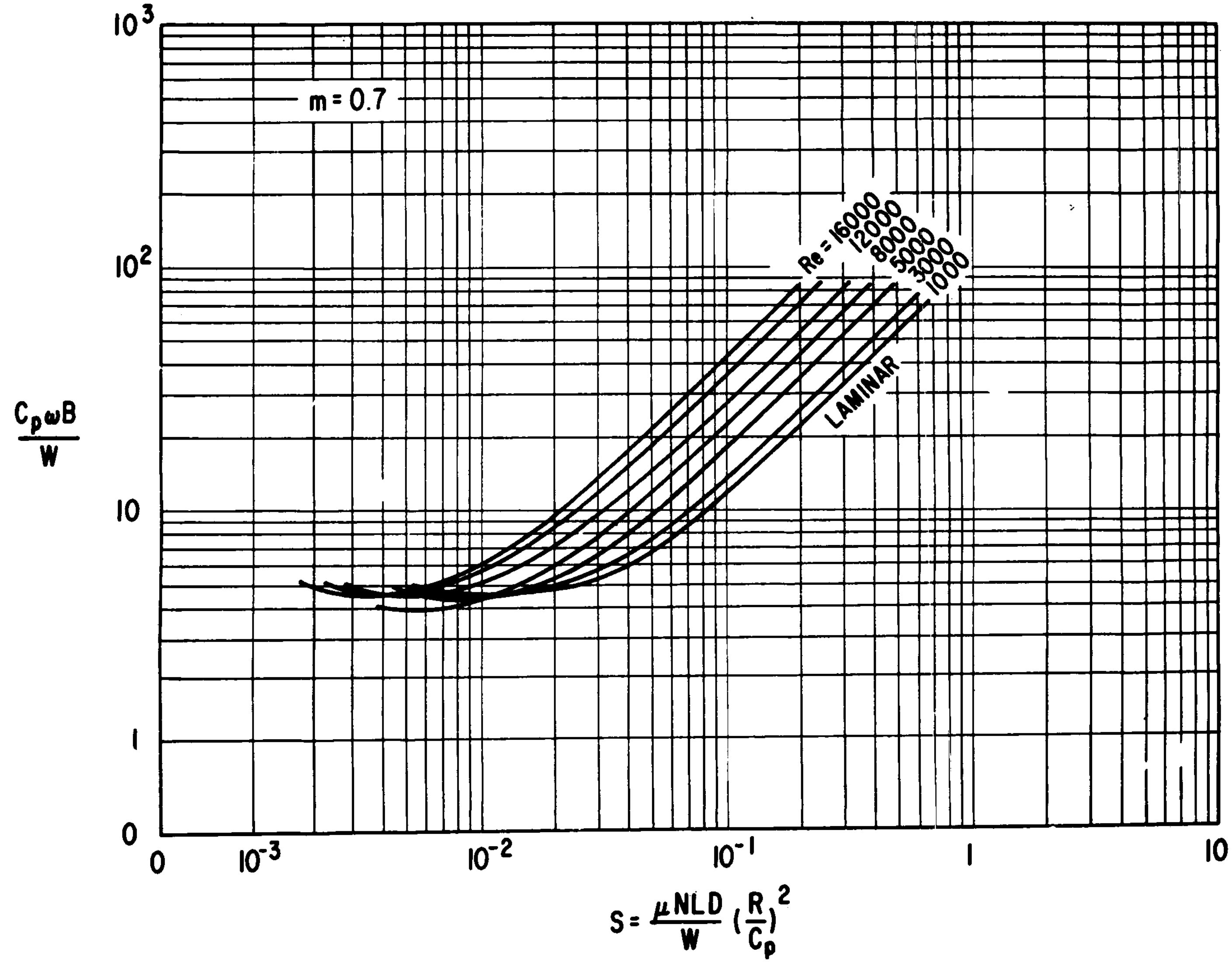

Figure 15. - Damping coefficient versus Sommerfeld number - m = 0.7. 4 Pads, $\beta = 80^o$, $\theta_p = 0.55$, L/D = 1.0.

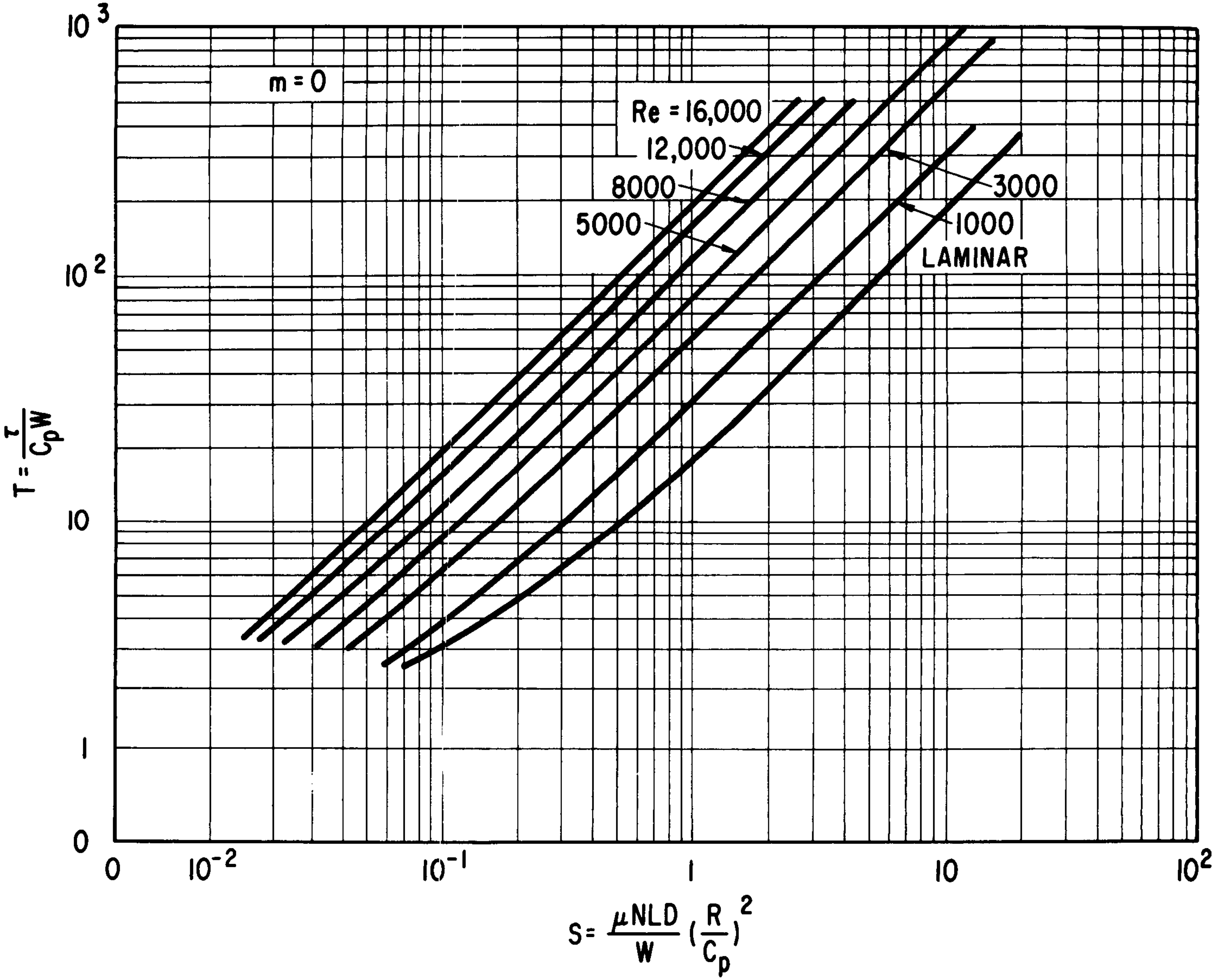

Figure 16. - Friction torque versus Sommerfeld number - m = 0. 4 Pads, $\beta = 80^{\circ}$, $\theta_p = 0.55$, L/D = 1.0.

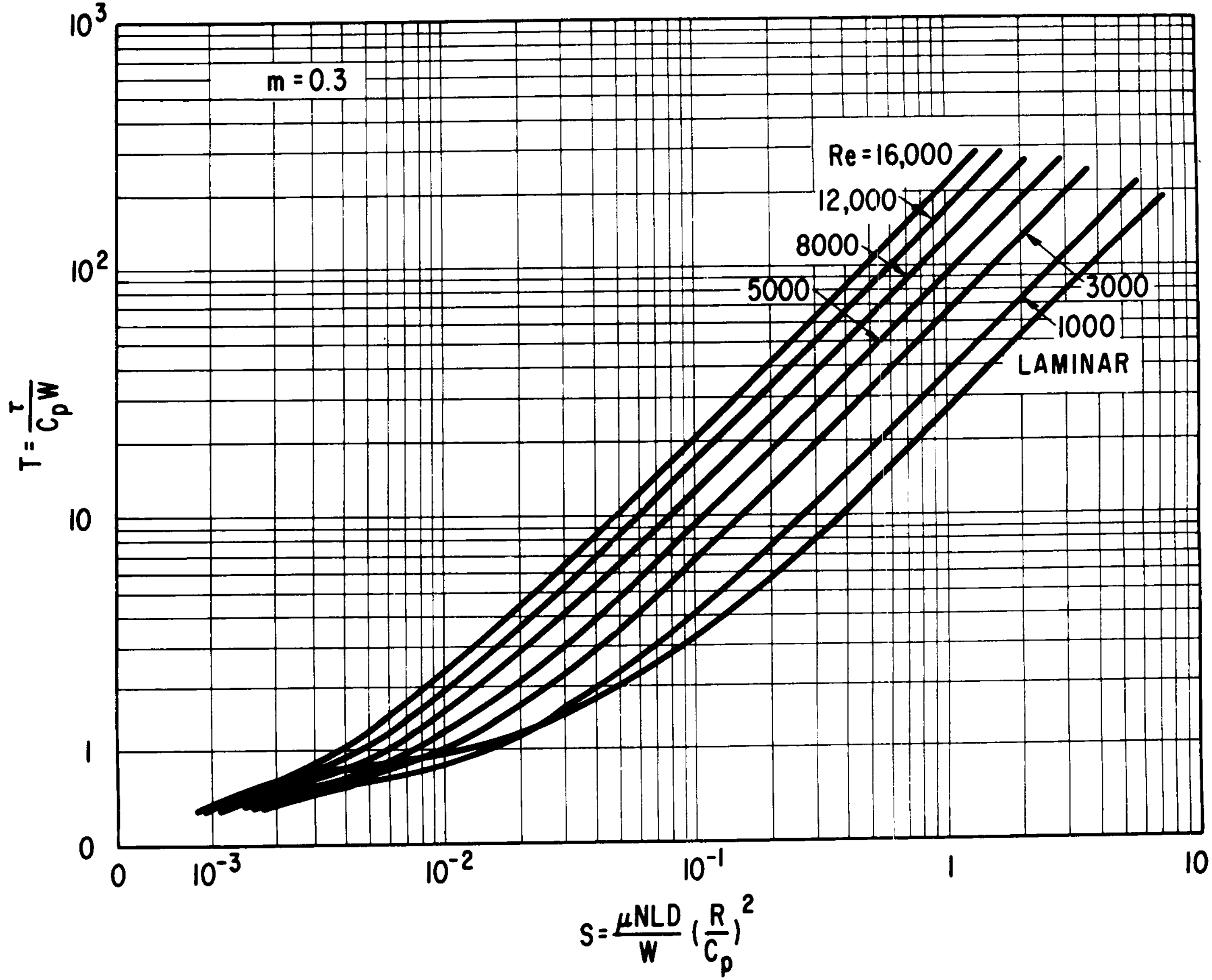

Figure 17. - Friction torque versus Sommerfeld number - m = 0.3. 4 Pads, $\beta = 80^{o}$, $\theta_p = 0.55$, L/D = 1.0.

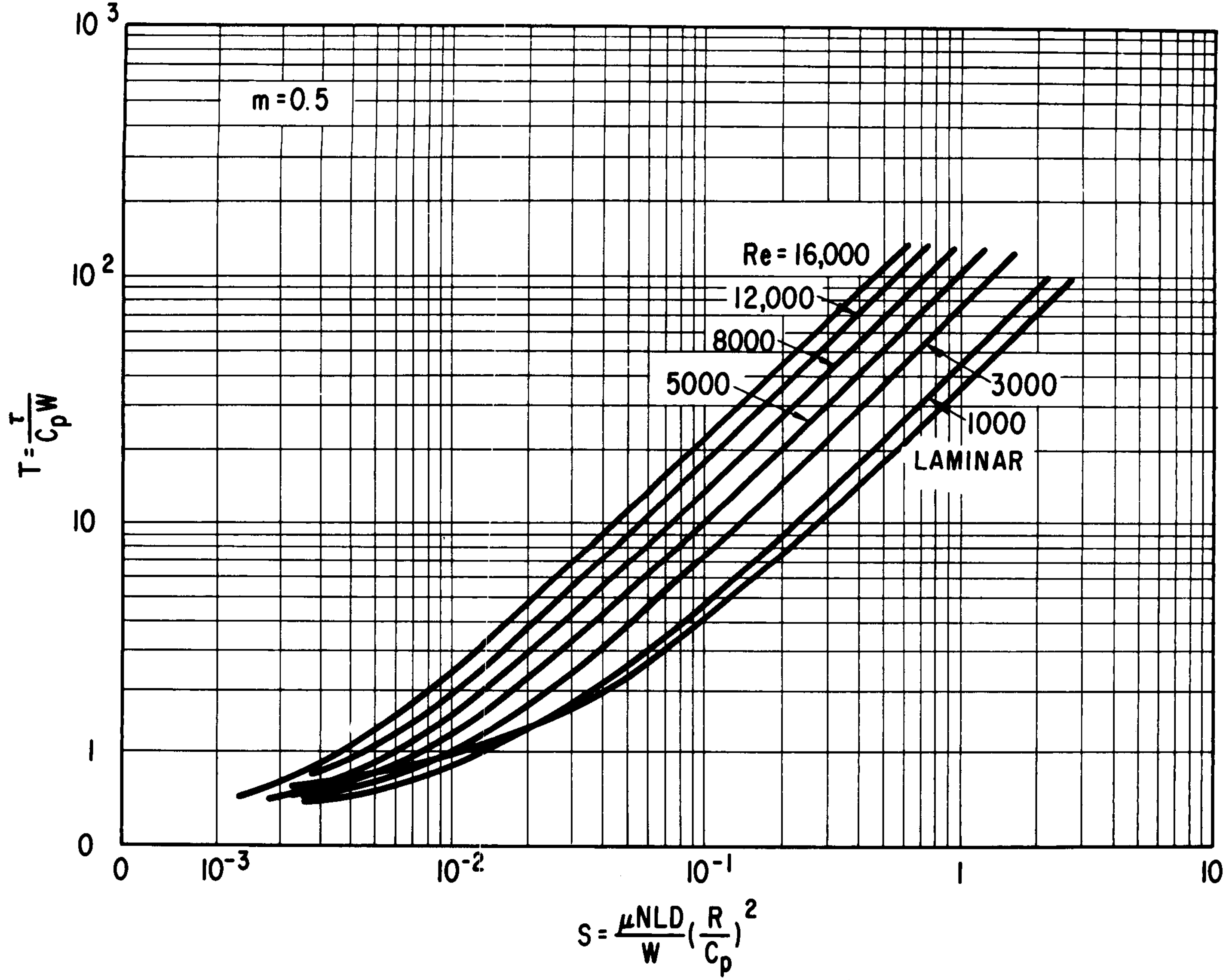

Figure 18. - Friction torque versus Sommerfeld number - m = 0.5. 4 Pads, $\beta = 80^\circ$, $\theta_p = 0.55$, L/D = 1.0.

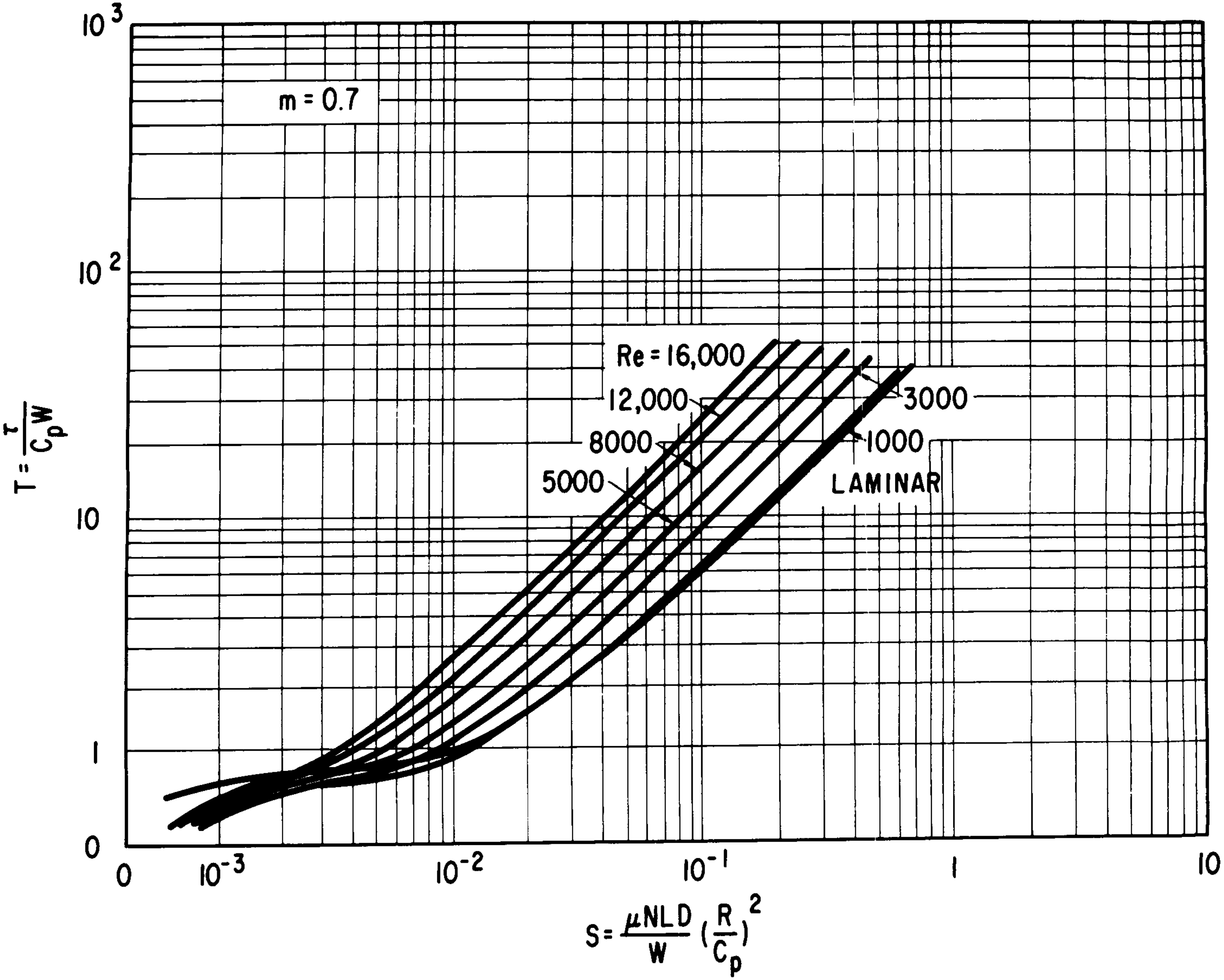

Figure 19. - Friction torque versus Sommerfeld number - m = 0.7. 4 Pads, $\beta = 80^{\circ}$, $\theta_p = 0.55$, L/D = 1.0.

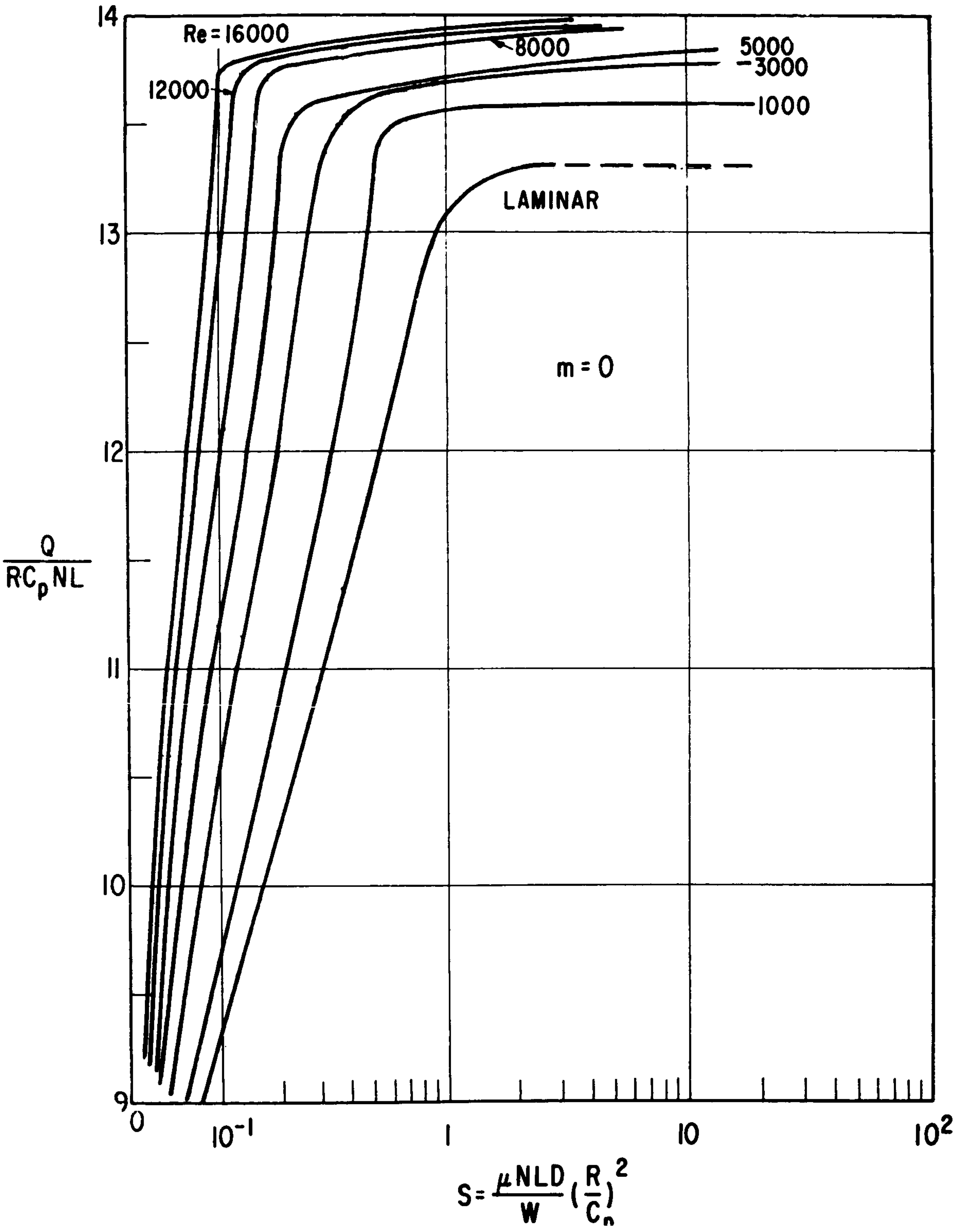

Figure 20. - Dimensionless flow versus Sommerfeld number - m = 0.
4 Pads, $\beta = 80^{\circ}$, $\theta_p = 0.55$, L/D = 1.0.

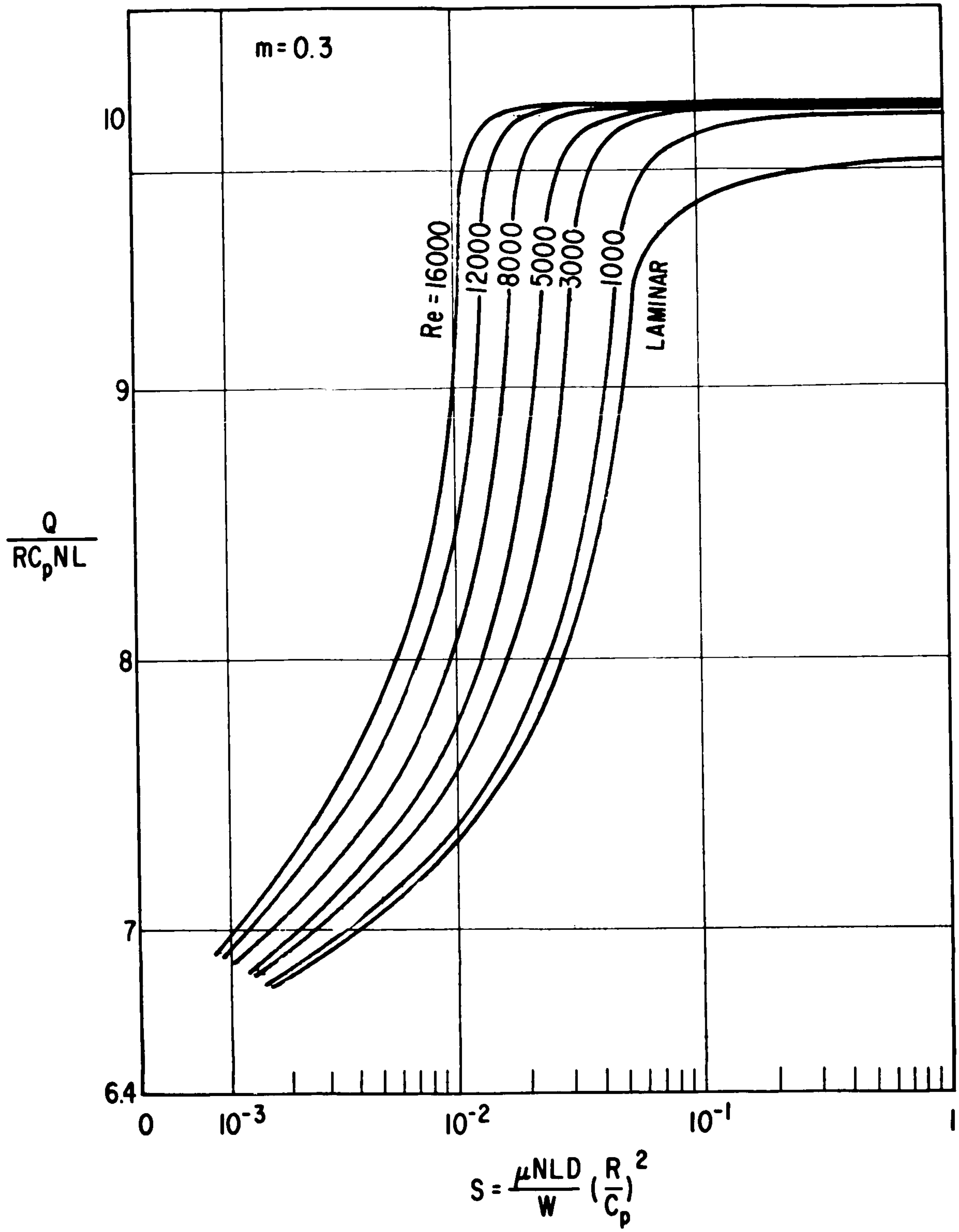

Figure 21. - Dimensionless flow versus Sommerfeld number - m = 0.3.
4 Pads, $\beta = 80^{\circ}$, $\theta_p = 0.55$, L/D = 1.0.

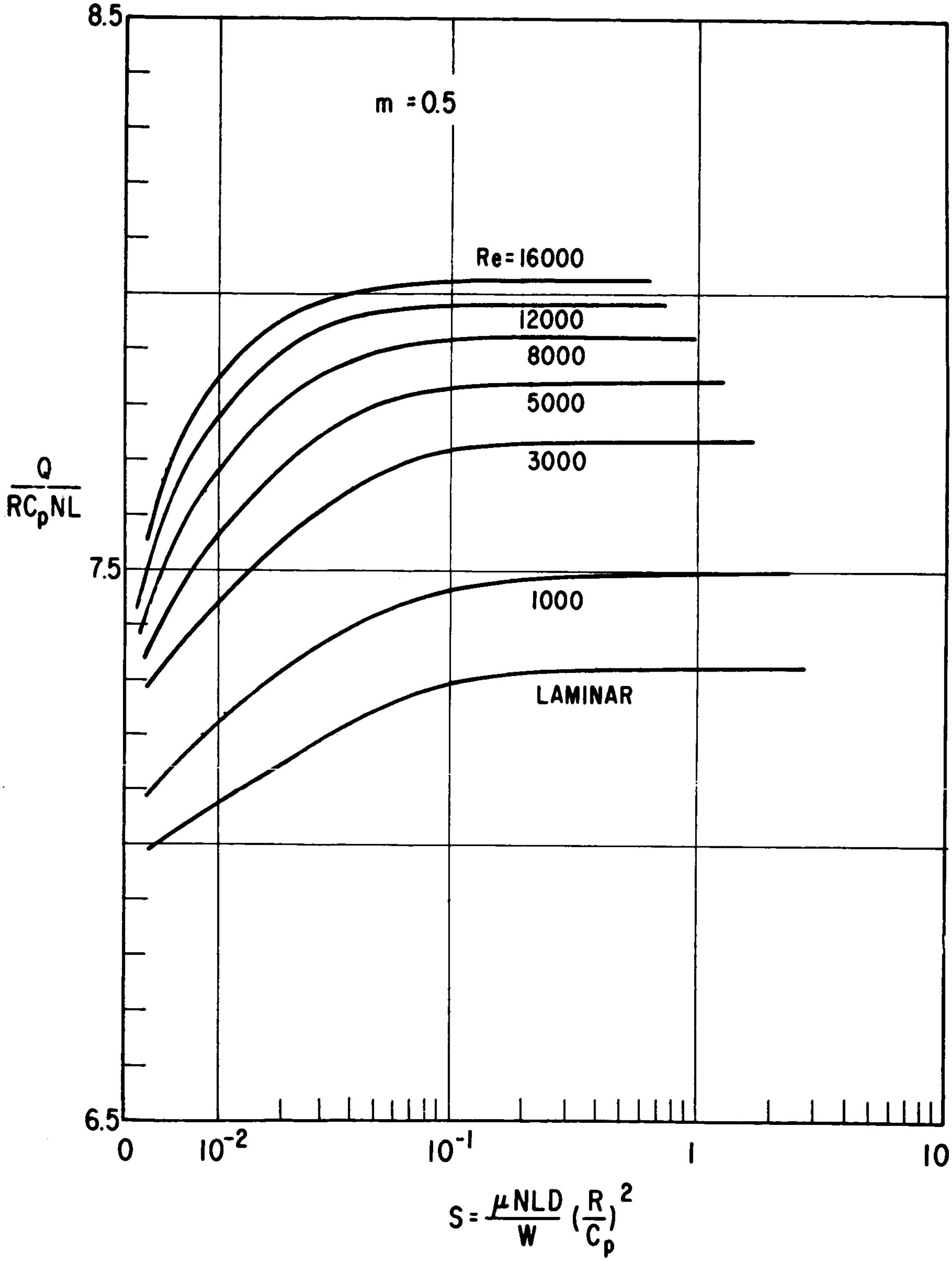

Figure 22. - Dimensionless flow versus Sommerfeld number - m = 0.5. 4 Pads, $\beta = 80^o$, $\theta_p = 0.55$, L/D = 1.0.

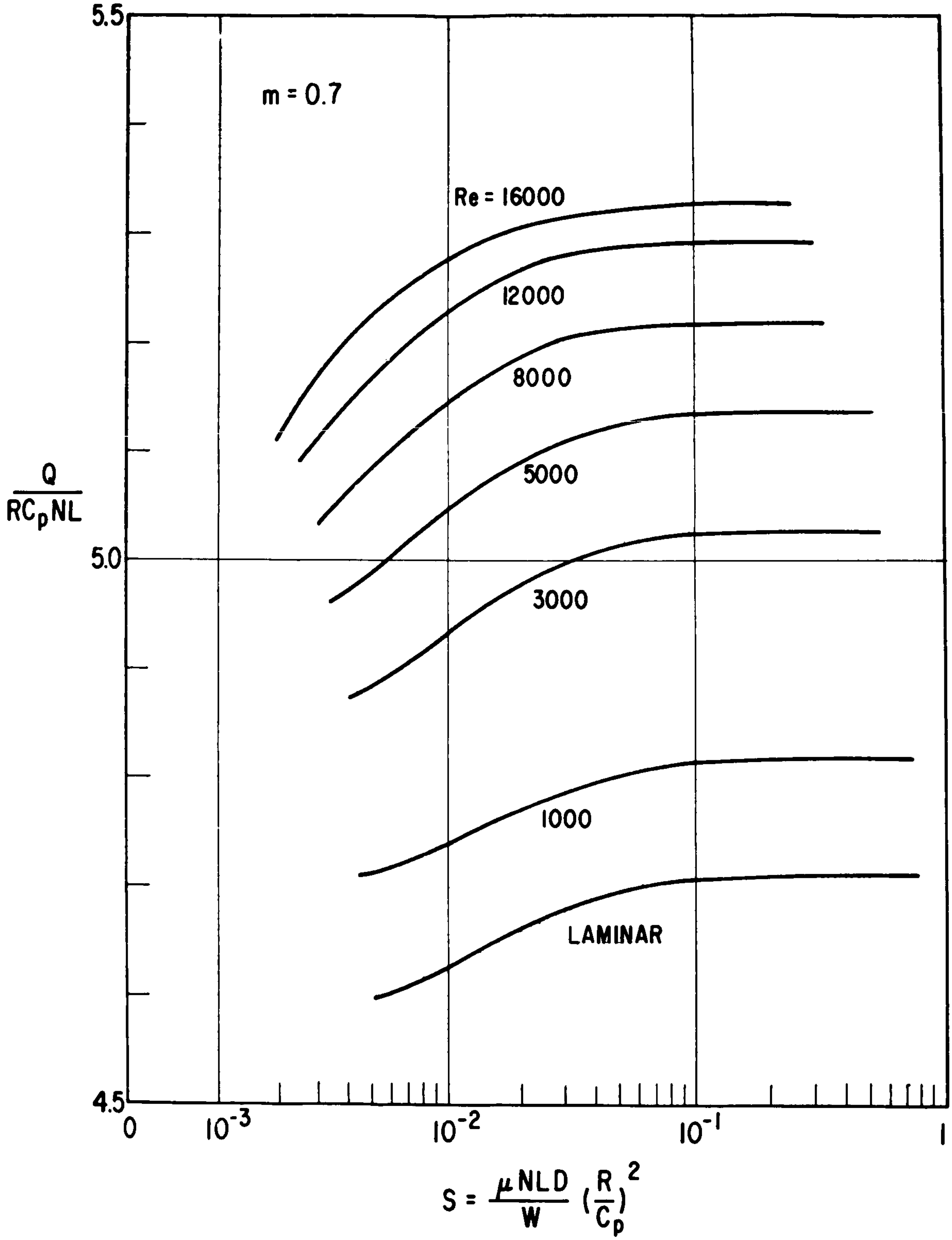

Figure 23. - Dimensionless flow versus Sommerfeld number - m = 0.7. 4 Pads, $\beta = 80^{\circ}$, $\theta_p = 0.55$, $L/D = 1.0$.

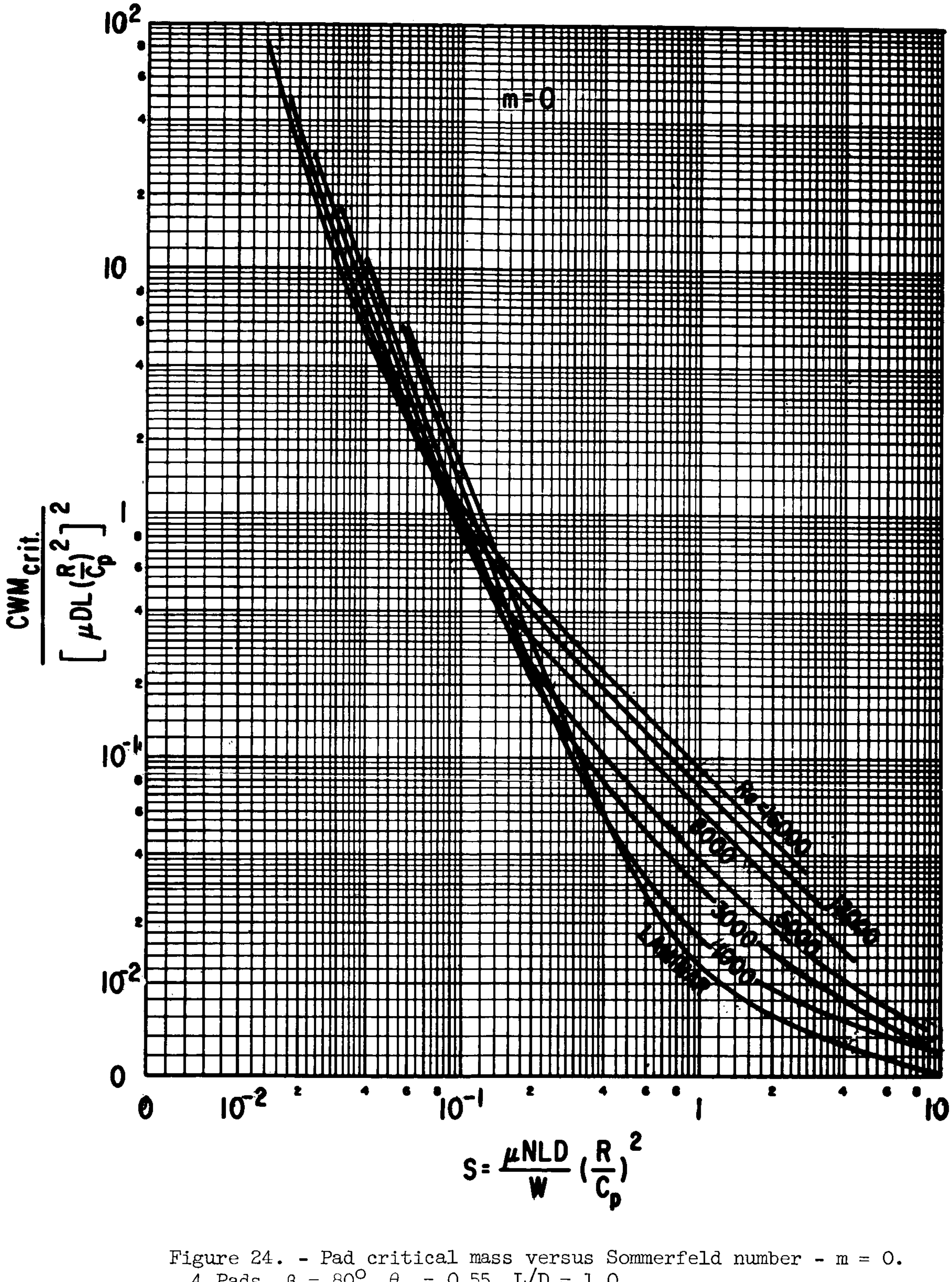

Figure 24. - Pad critical mass versus Sommerfeld number - m = 0. 4 Pads, $\beta = 80^{\circ}$, $\theta_p = 0.55$, L/D = 1.0.

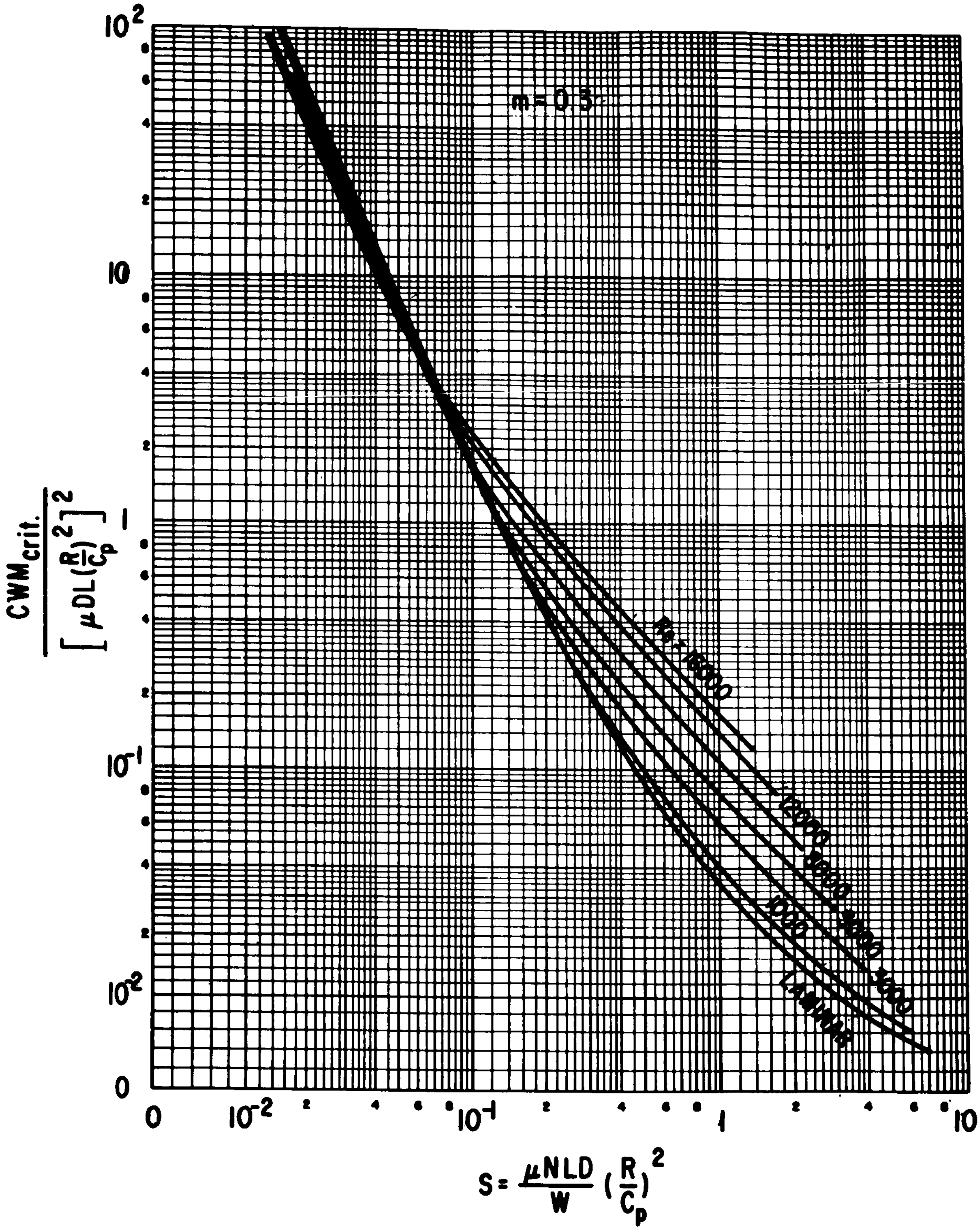

Figure 25. - Pad critical mass versus Sommerfeld number - m = 0.3. 4 Pads, $\beta = 80^{\circ}$, $\theta_p = 0.55$, L/D = 1.0.

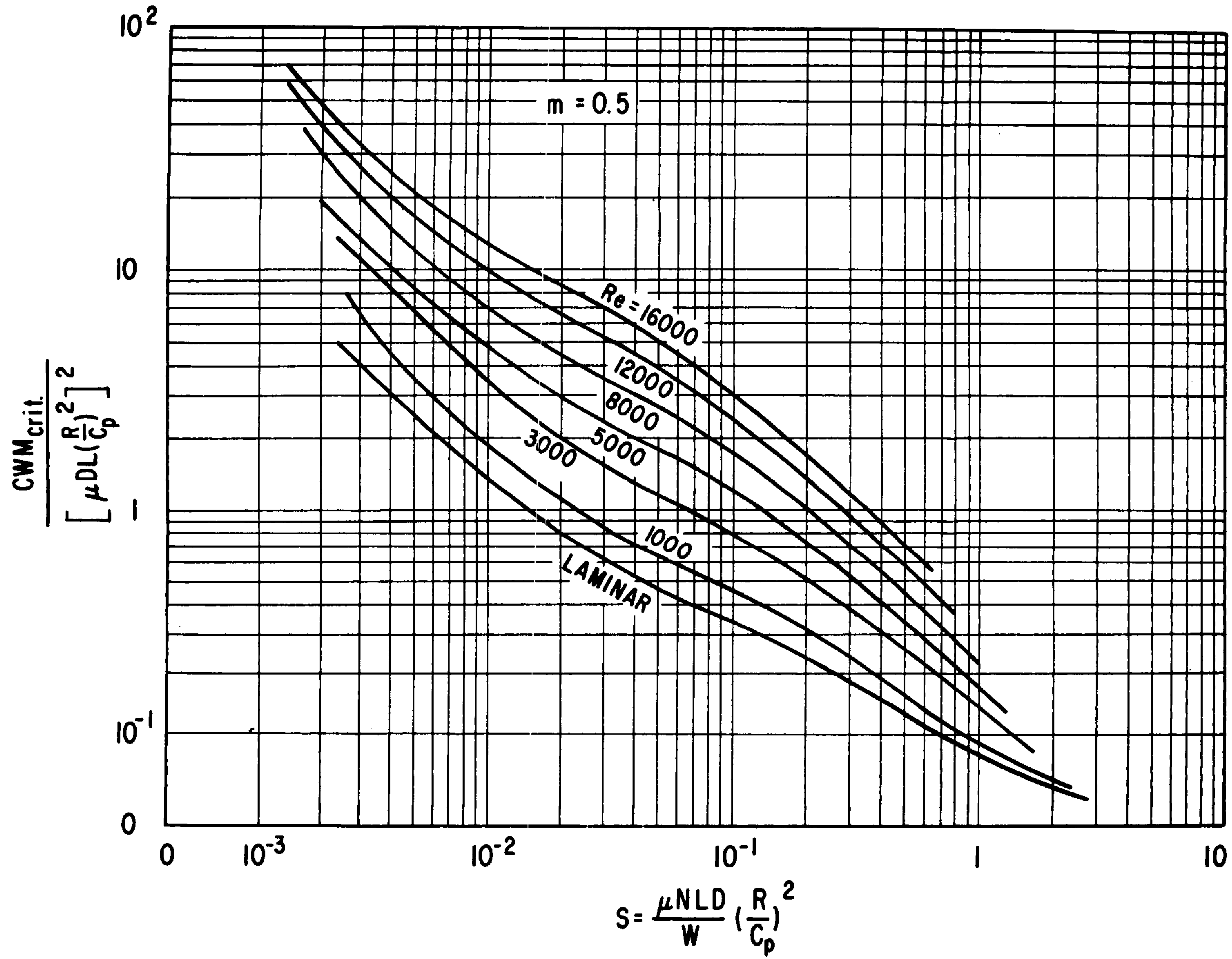

Figure 26. - Pad critical mass versus Sommerfeld number - m = 0.5.
4 Pads, $\beta = 80^{\circ}$, $\theta_p = 0.55$, L/D = 1.0.

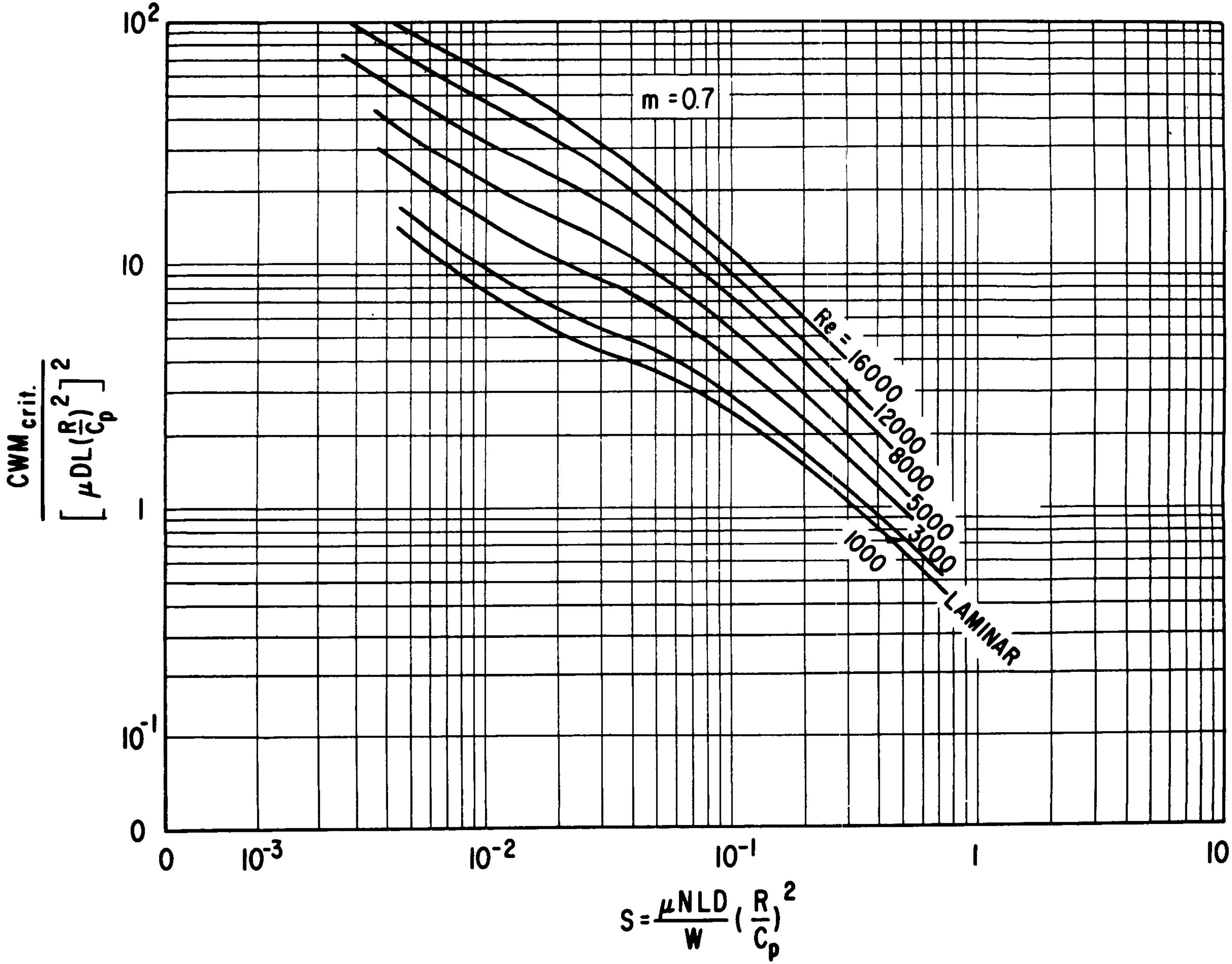

Figure 27. - Pad critical mass versus Sommerfeld number - m = 0.7.
4 Pads, $\beta = 80^{\circ}$, $\theta_p = 0.55$, L/D = 1.0.

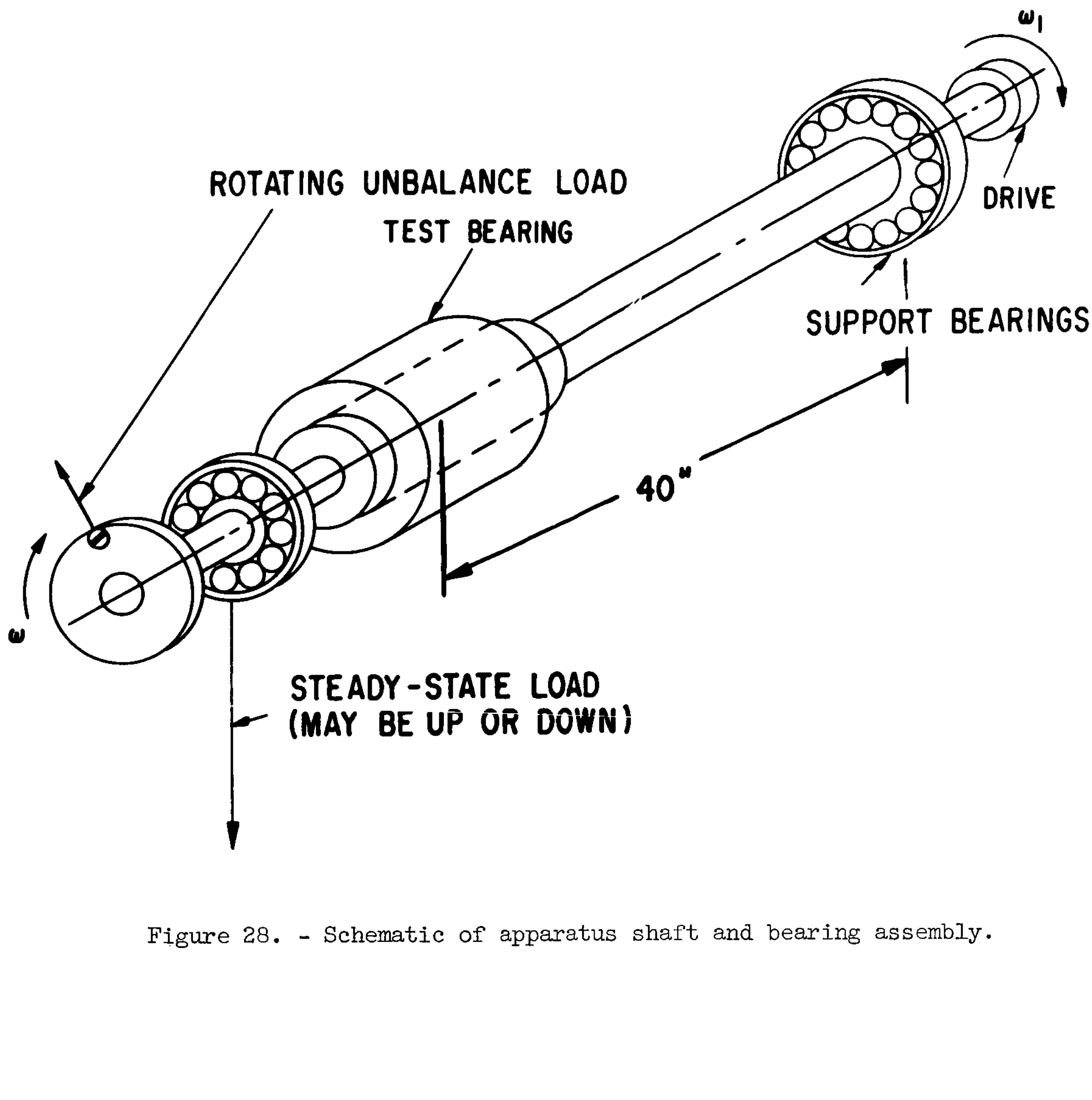

Figure 28. - Schematic of apparatus shaft and bearing assembly.

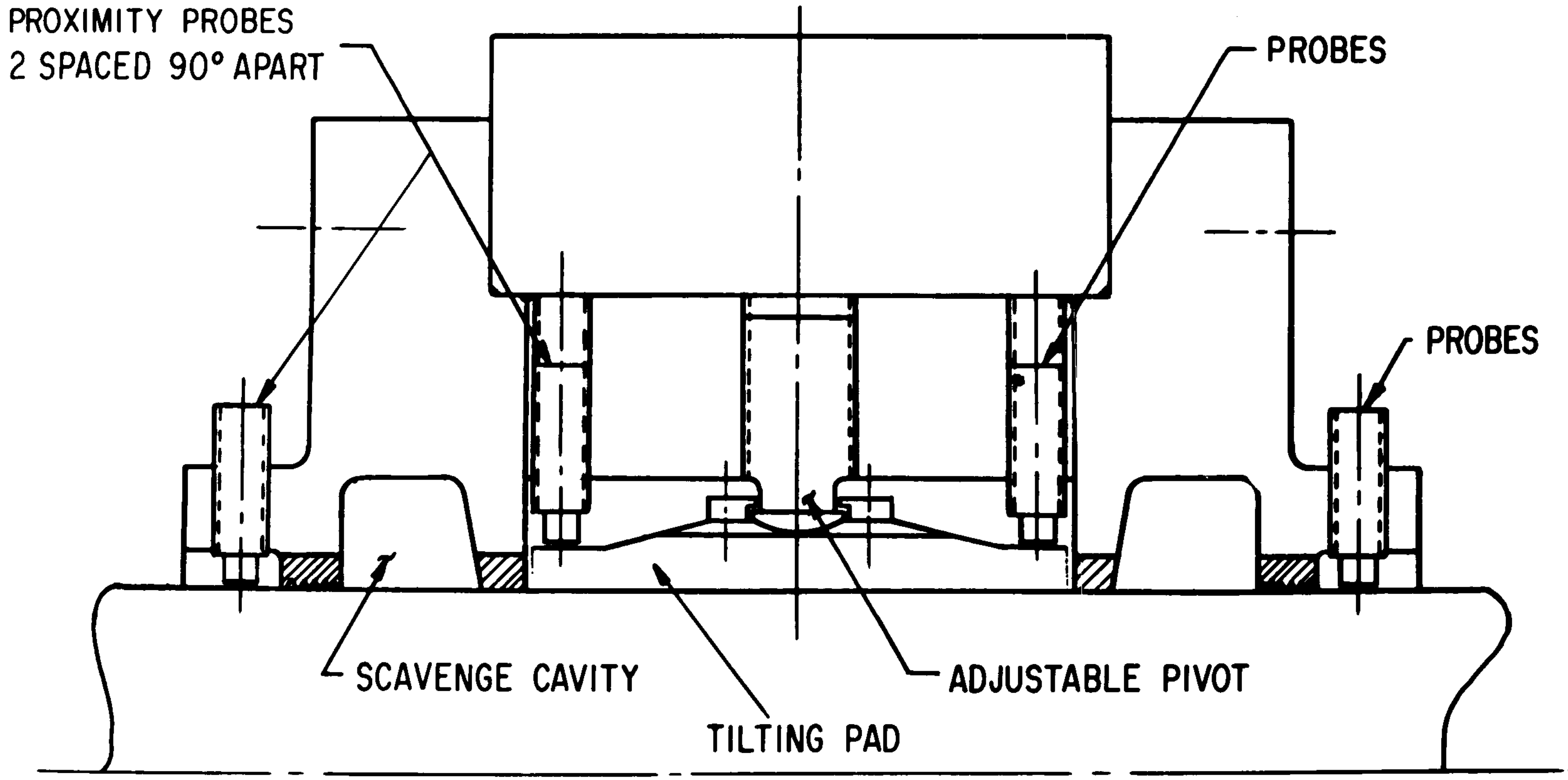

Figure 29. - Schematic of tilting-pad bearing installed in test bearing housing.

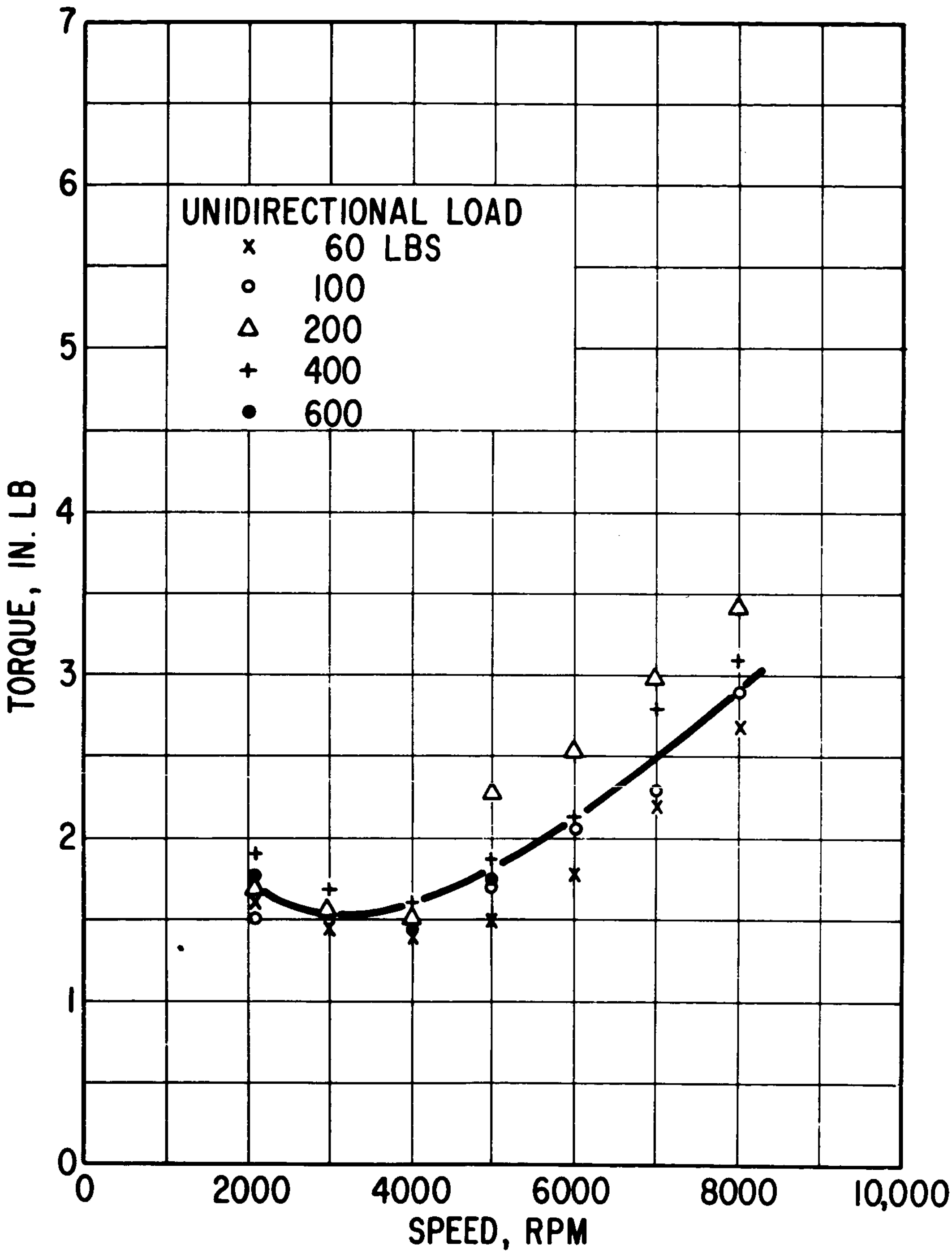

Figure 30. - Dynamic load bearing apparatus support and loader bearing friction torque.

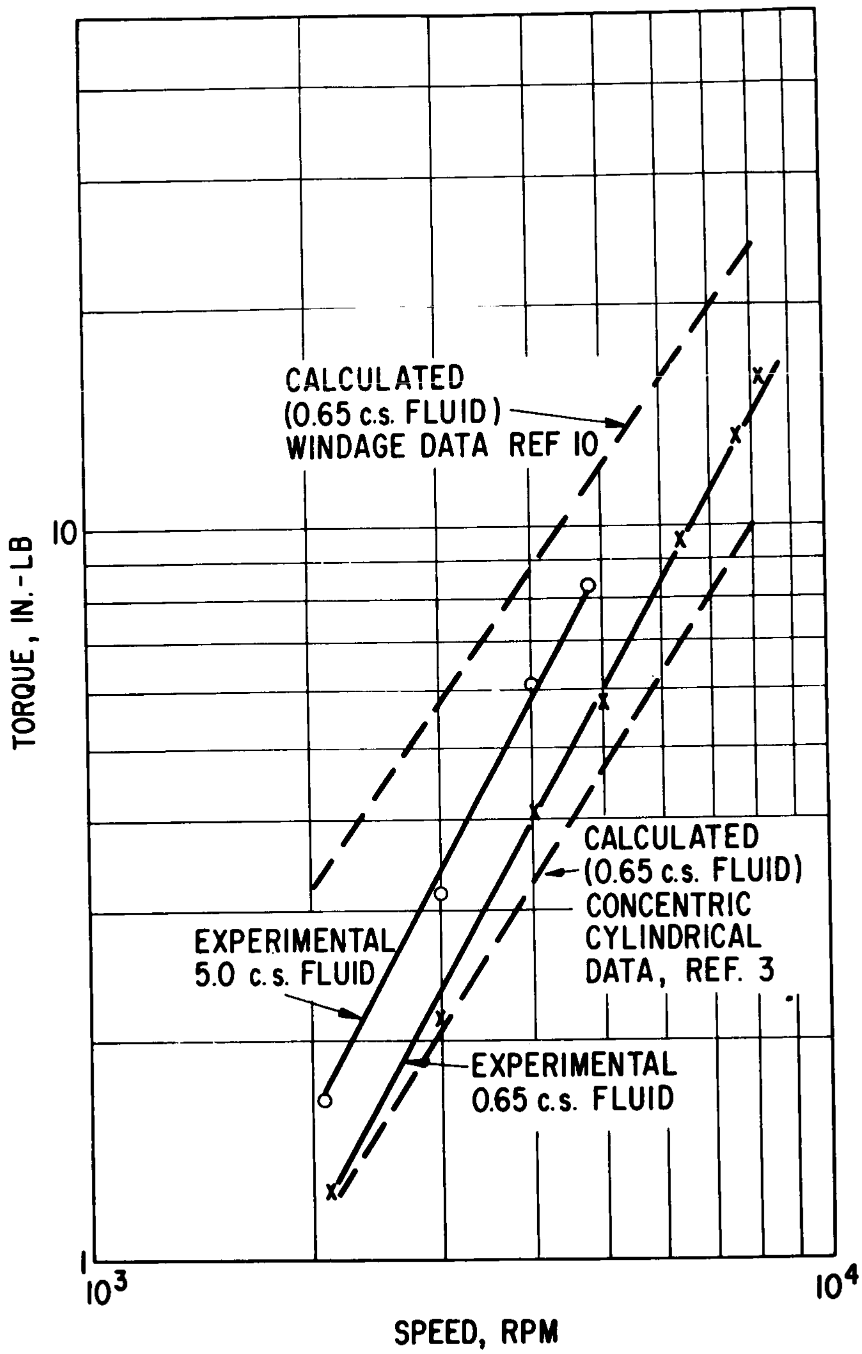

Figure 31. - Dynamic load bearing apparatus measured friction drag from test bearing housing and seals.

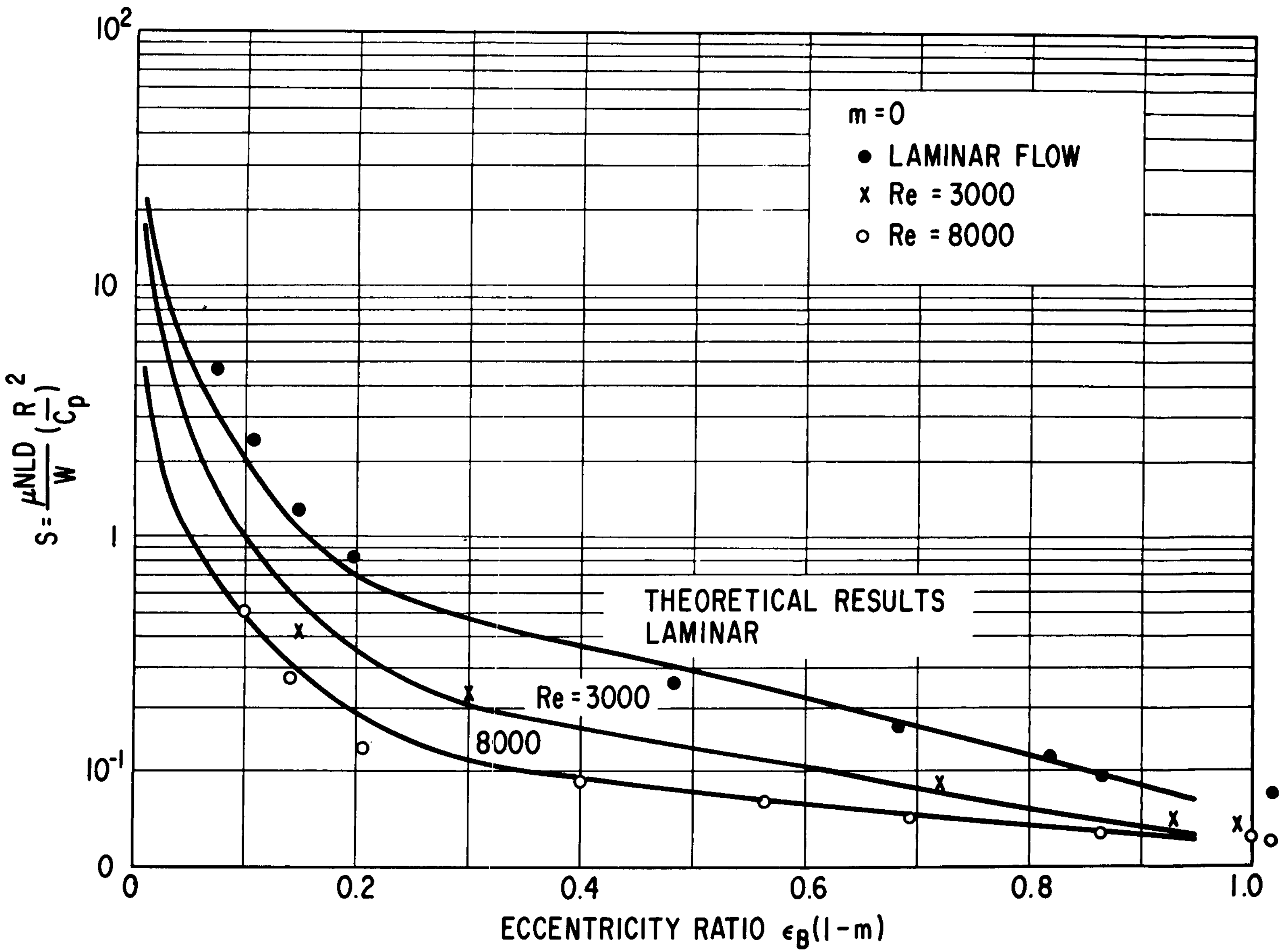

Figure 32. - Comparison between measured and calculated static load capacity - m = 0.

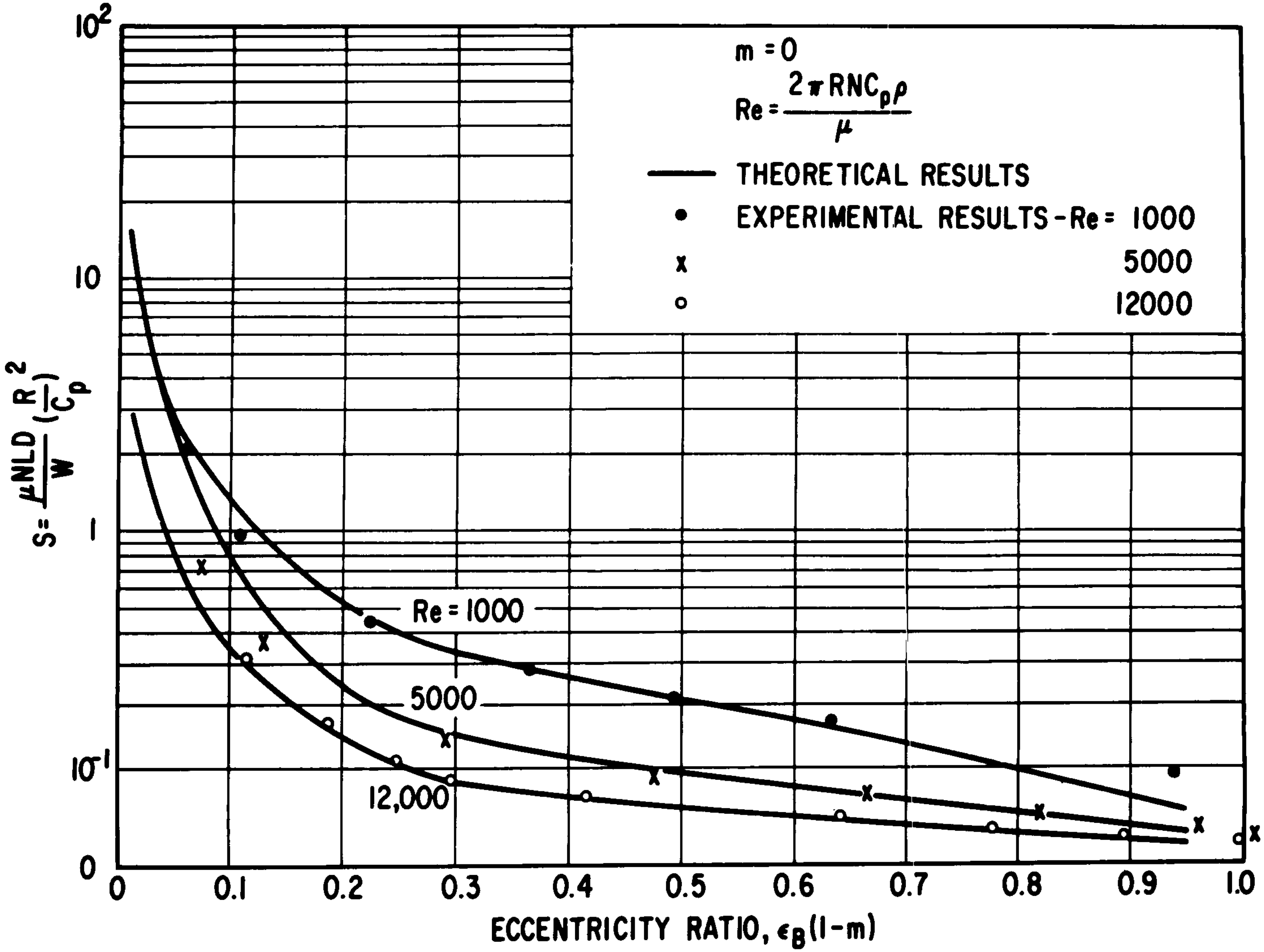

Figure 33. - Comparison between measured and calculated static load capacity - m = 0.

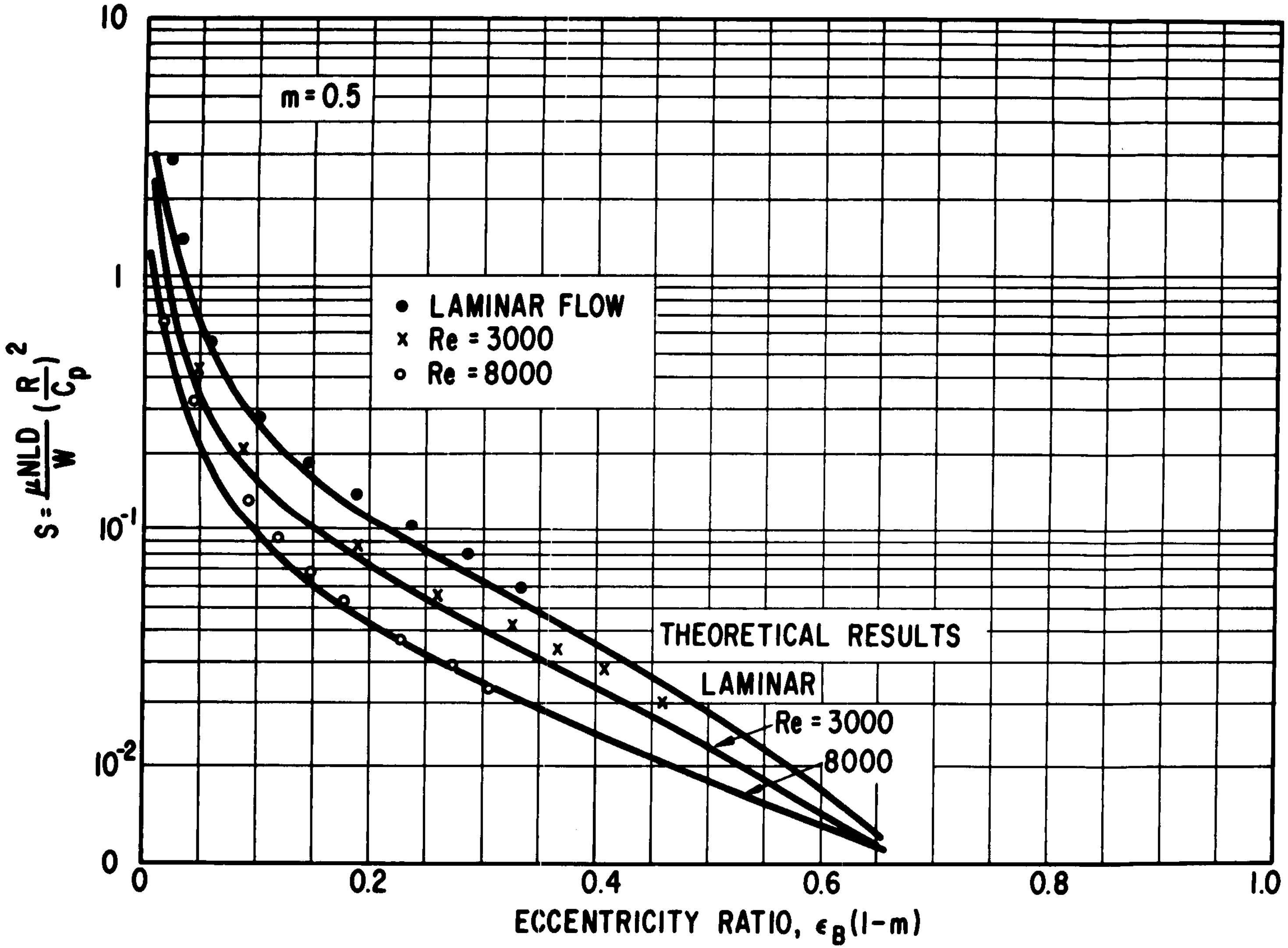

Figure 34. - Comparison between measured and calculated static load capacity - m = 0.5.

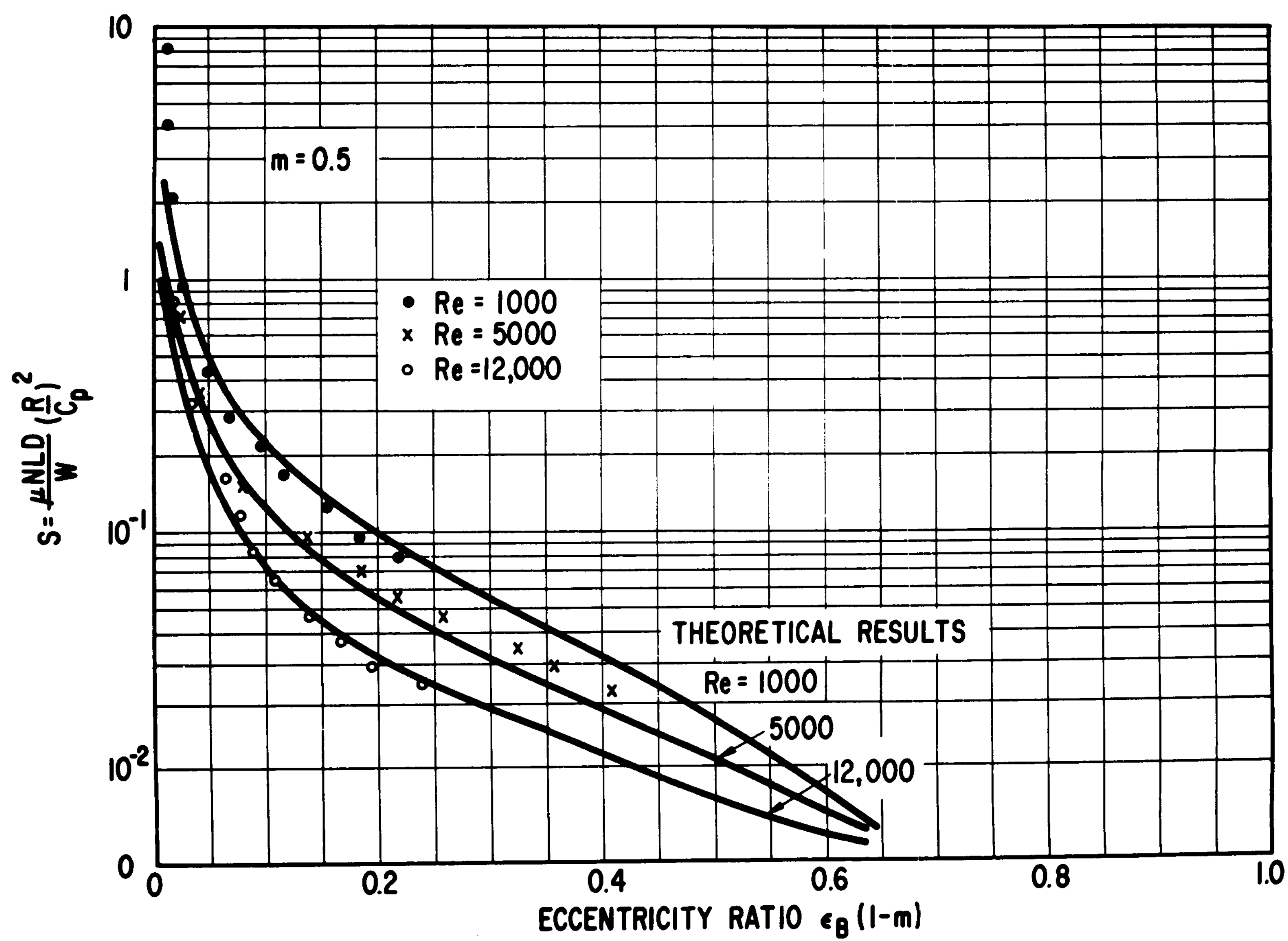

Figure 35. - Comparison between measured and calculated static load capacity - m = 0.5.

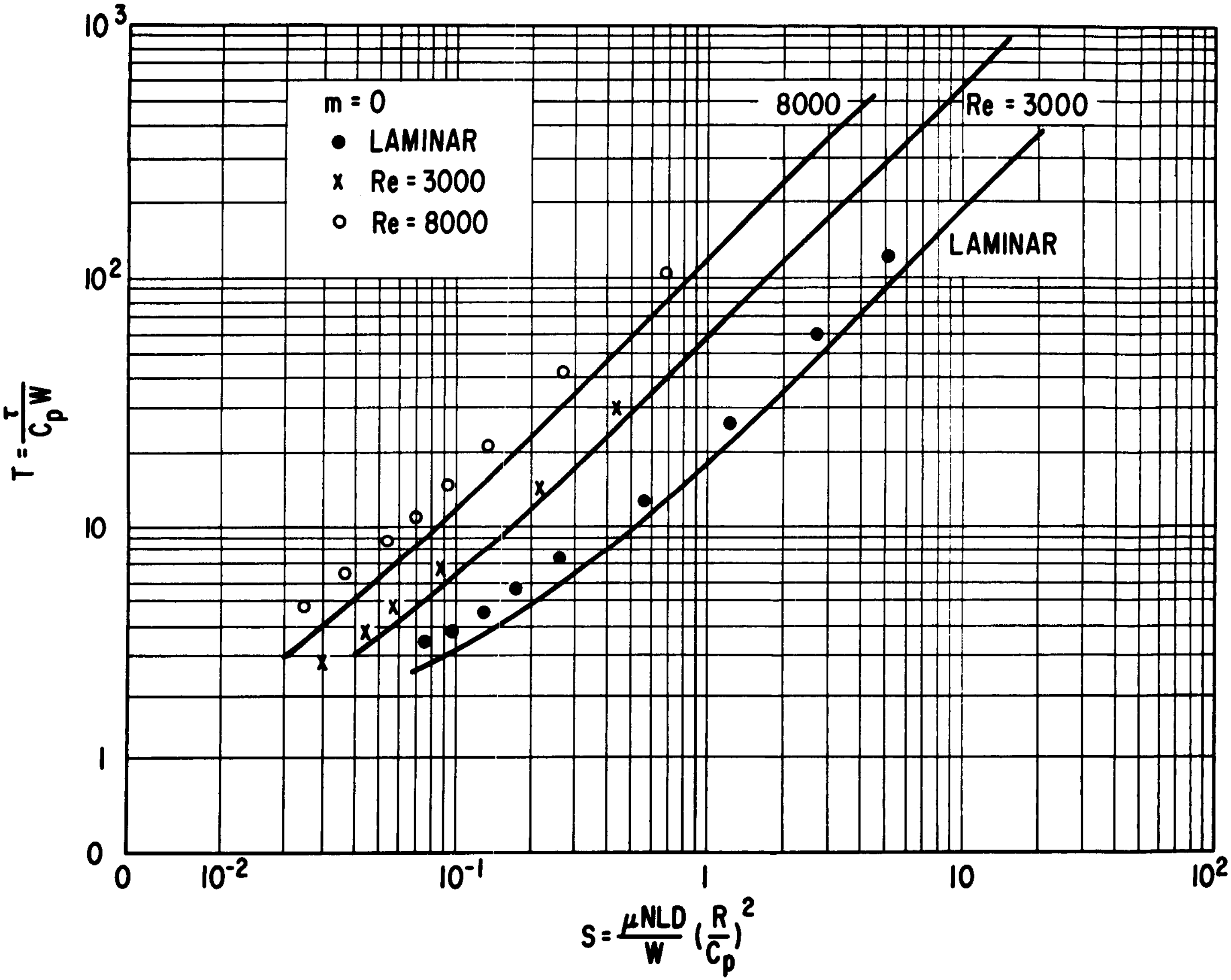

Figure 36. - Comparison between measured and calculated bearing friction torque - m = 0.

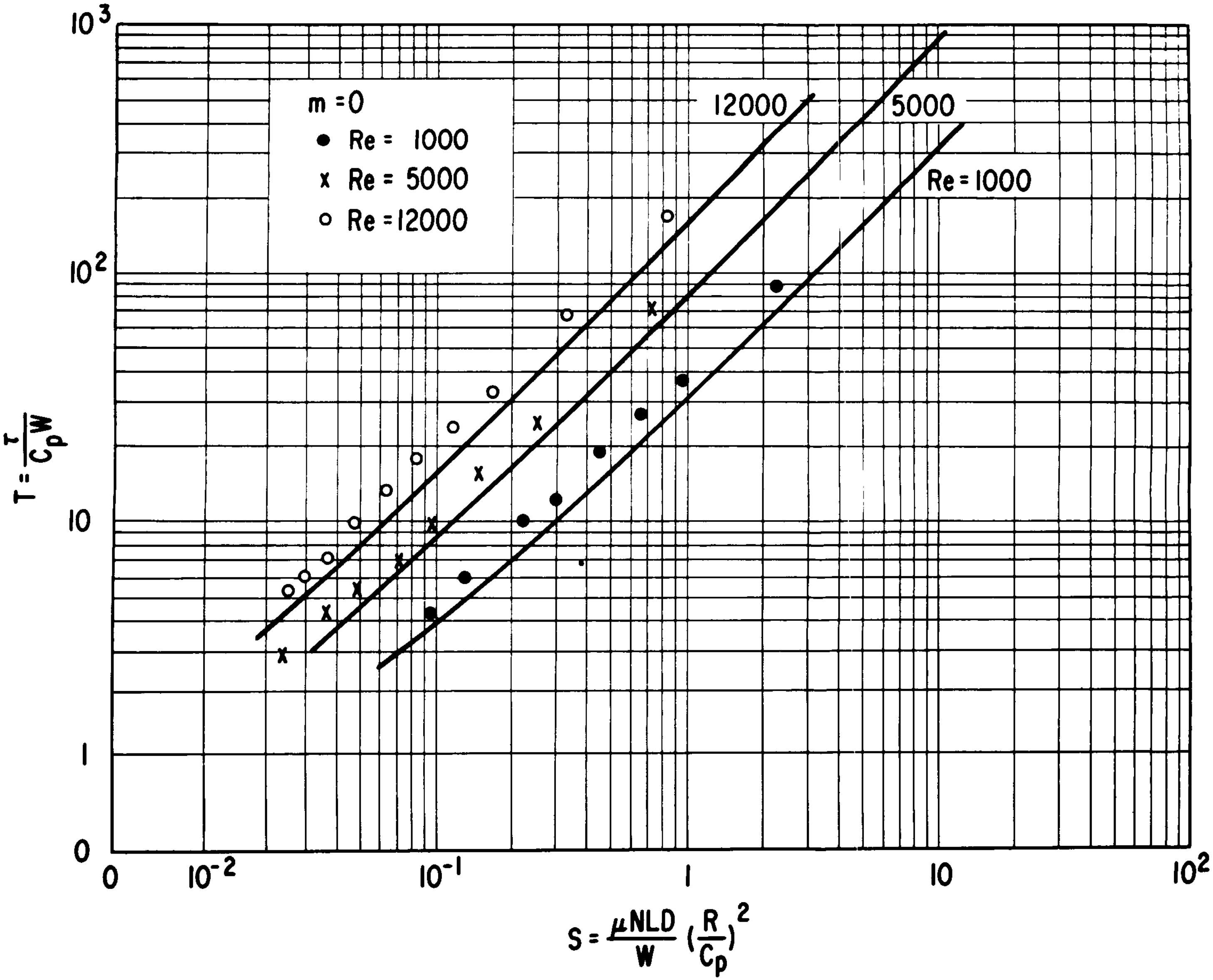

Figure 37. - Comparison between measured and calculated bearing friction torque - m = 0.

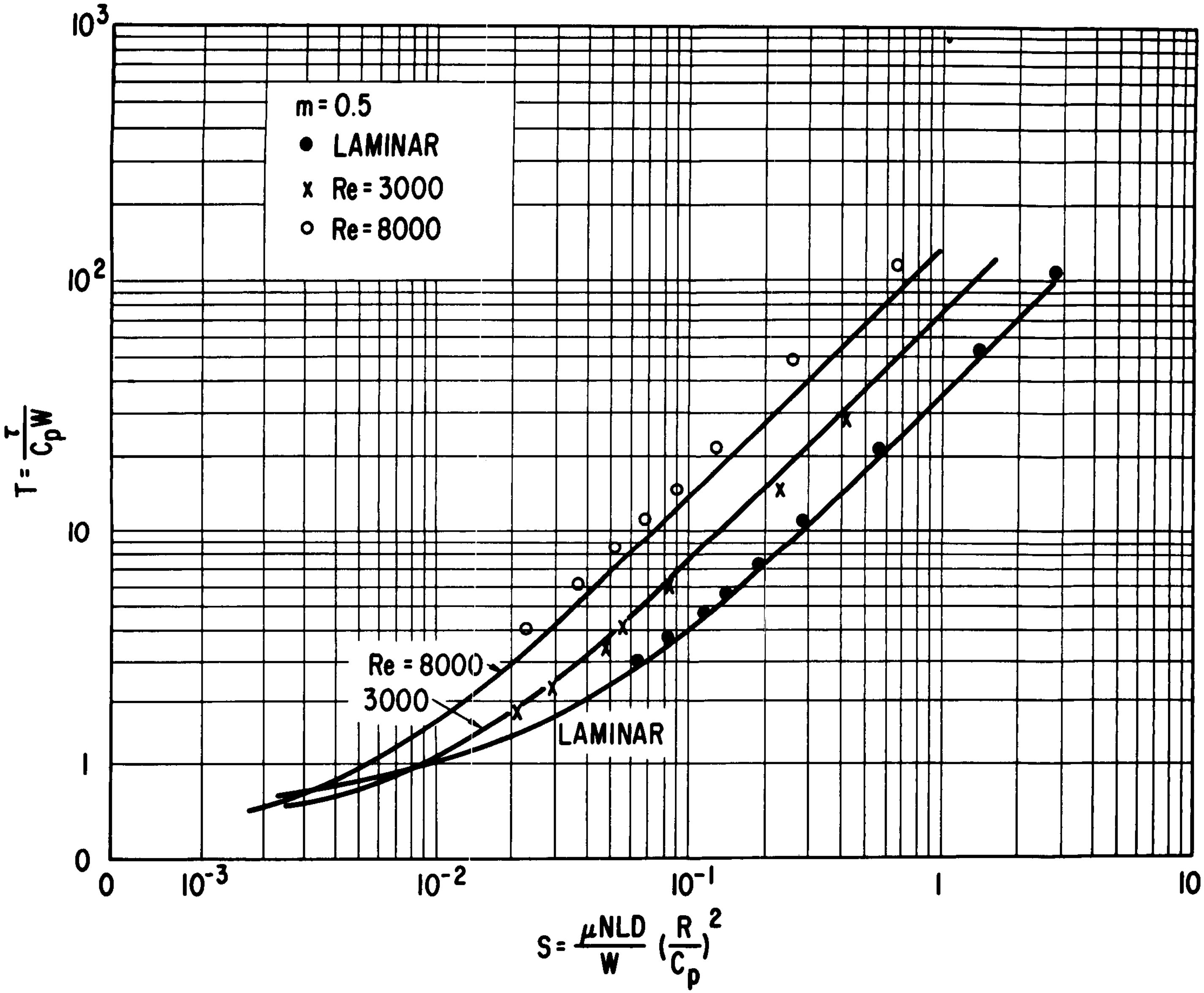

Figure 38. - Comparison between measured and calculated bearing friction torque - m = 0.5.

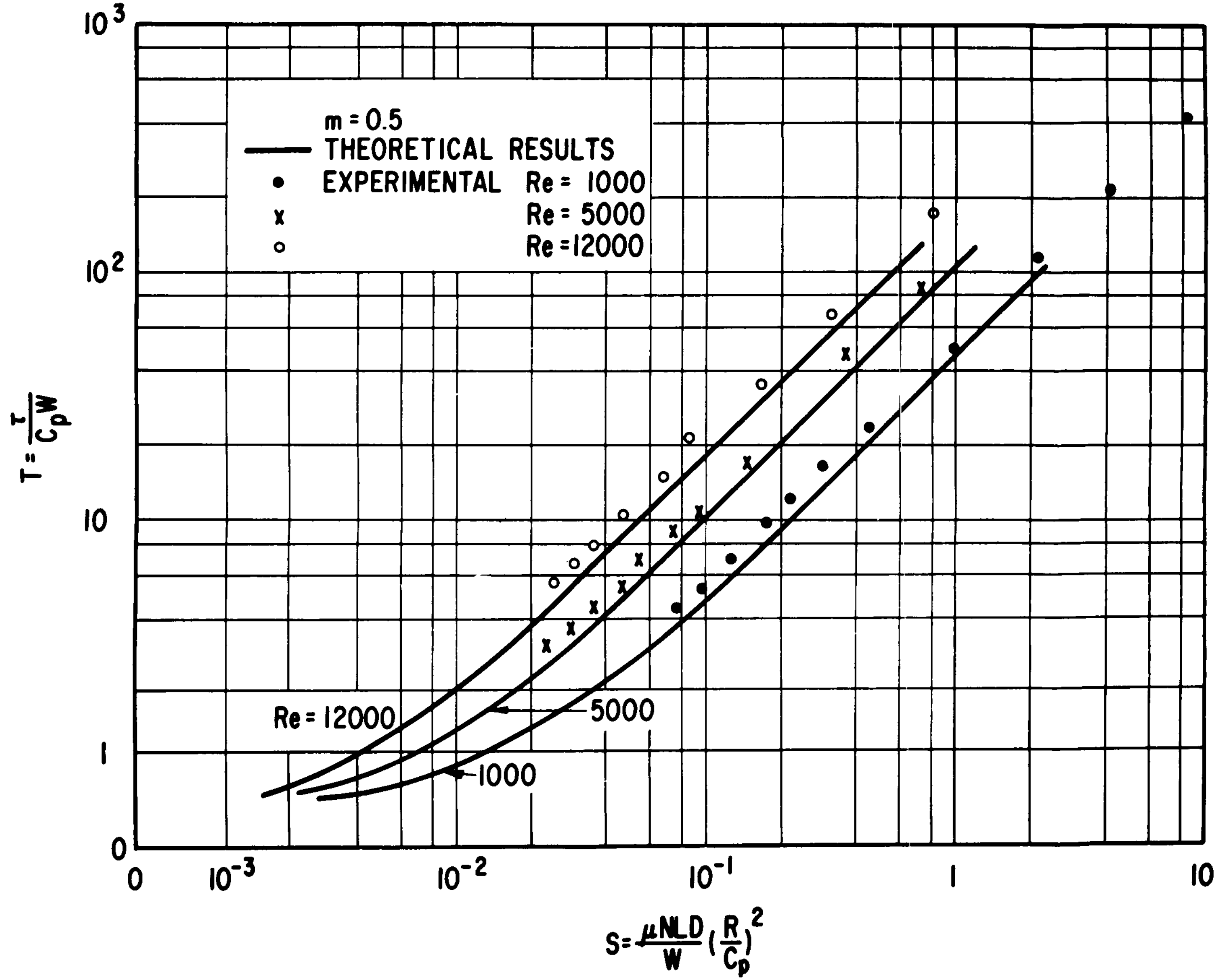

Figure 39. - Comparison between measured and calculated bearing friction torque - m = 0.5.

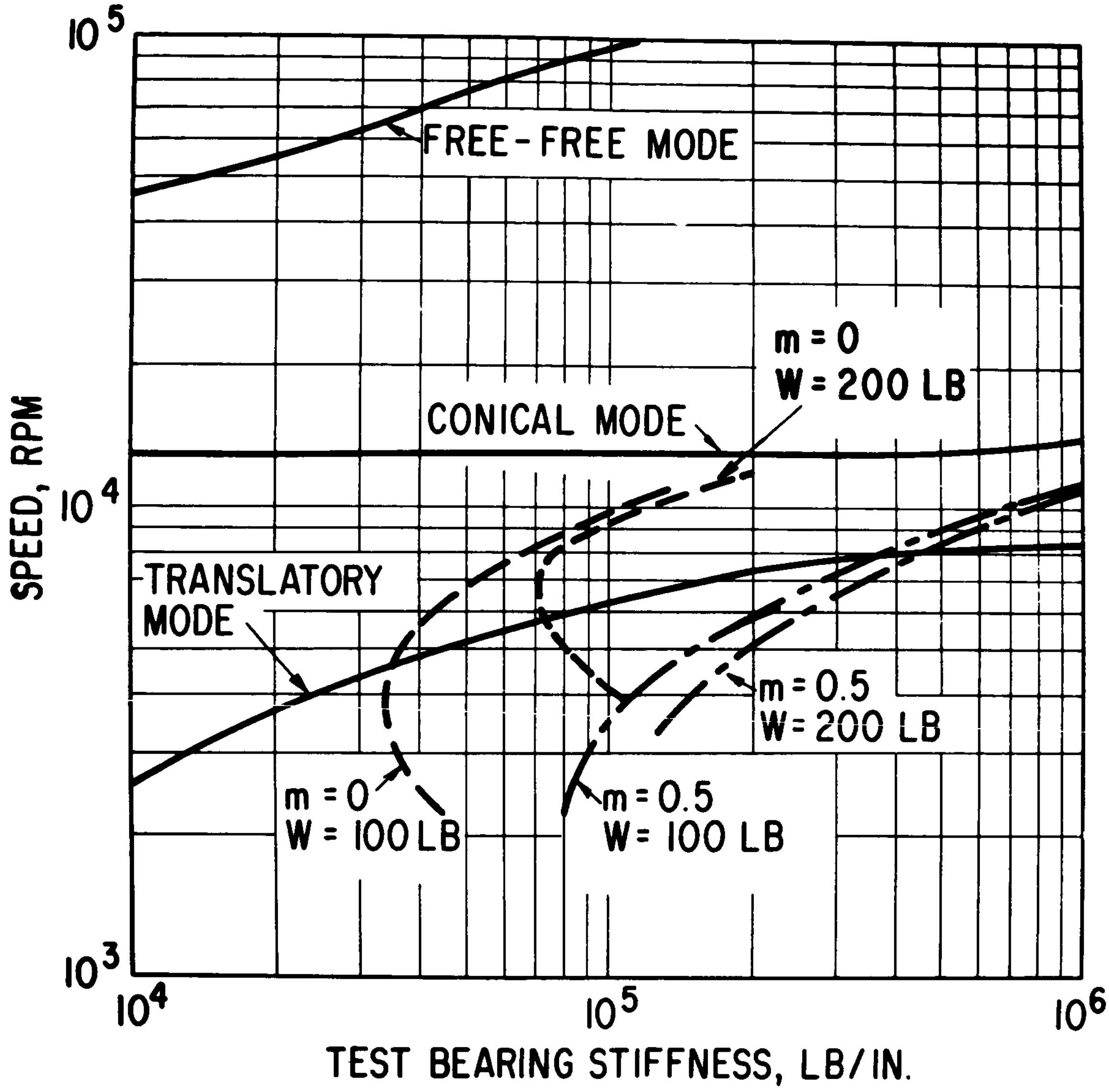

Figure 40. - Critical speed map for the dynamic load bearing apparatus.

(a) DC coupling, 0.5 v/cm.

(b) Filtered, 20 mv/cm.

Figure 41. - Oscilloscope traces of shaft motion in response to unbalance load. The "Square on Edge" in figure (a) shows the limits of the bearing clearance. The side of the square = 2 Cp (1-m) = 0.006 in. 4000 rpm (Re = 5000), 50 lb load.

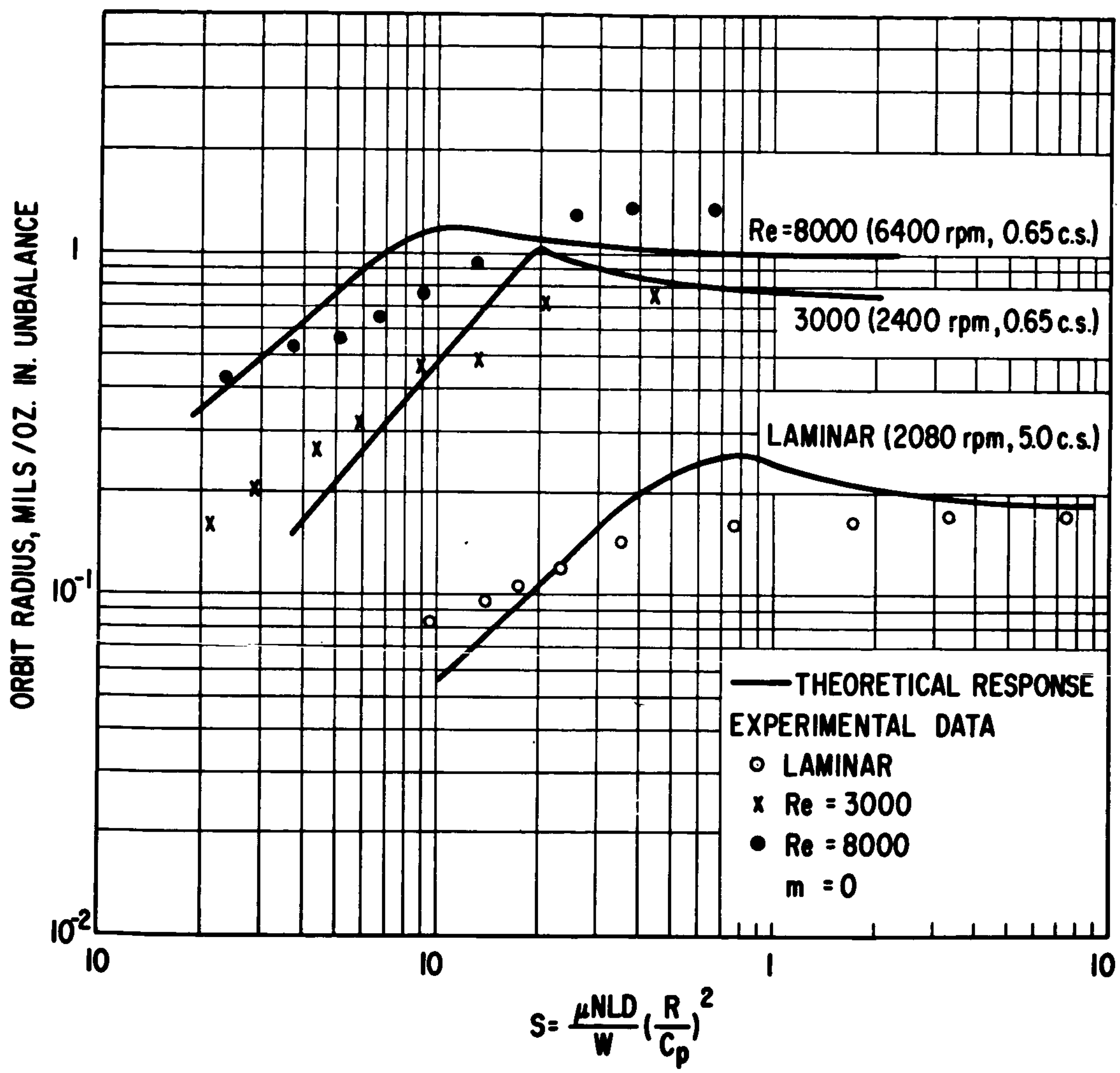

Figure 42. - Comparison between calculated and measured dynamic load response orbit amplitude - m = 0.

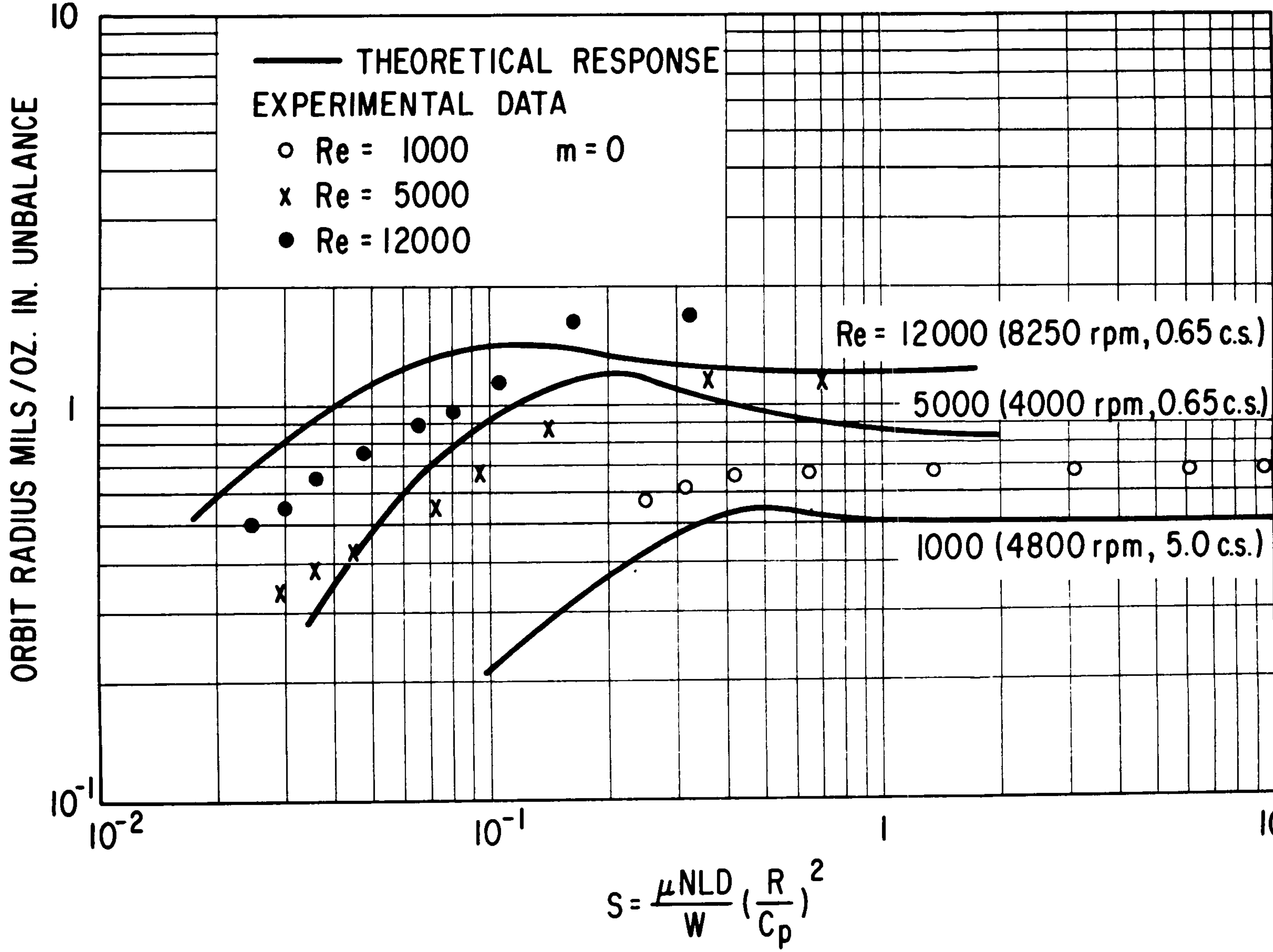

$$S = \frac{\mu N L D}{W}\left(\frac{R}{C_p}\right)^2$$

Figure 43. - Comparison between calculated and measured dynamic load response orbit amplitude - m = 0.

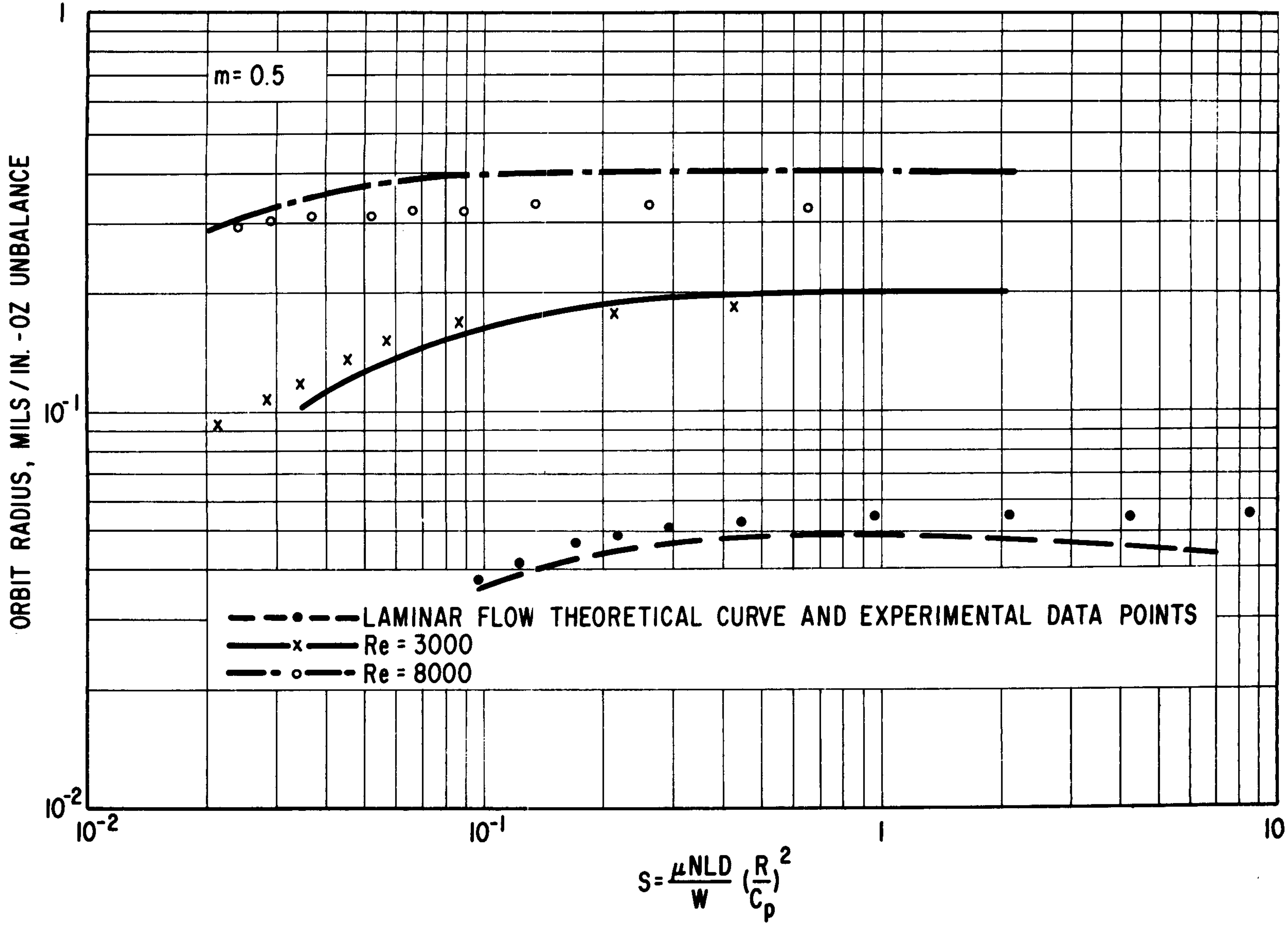

Figure 44. - Comparison between calculated and measured dynamic load response orbit amplitude - m = 0.5.

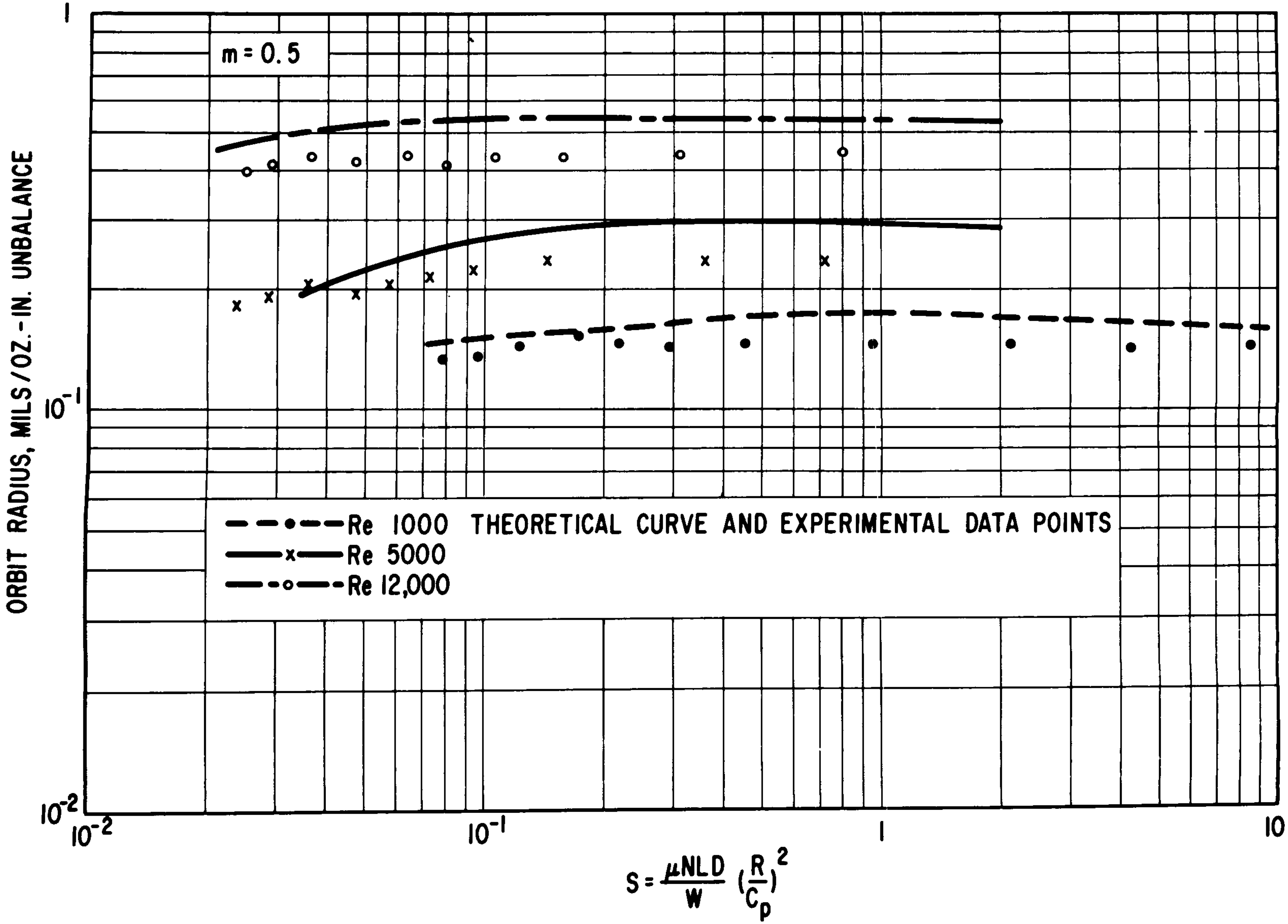

Figure 45. - Comparison between calculated and measured dynamic load response orbit amplitude - m = 0.5.

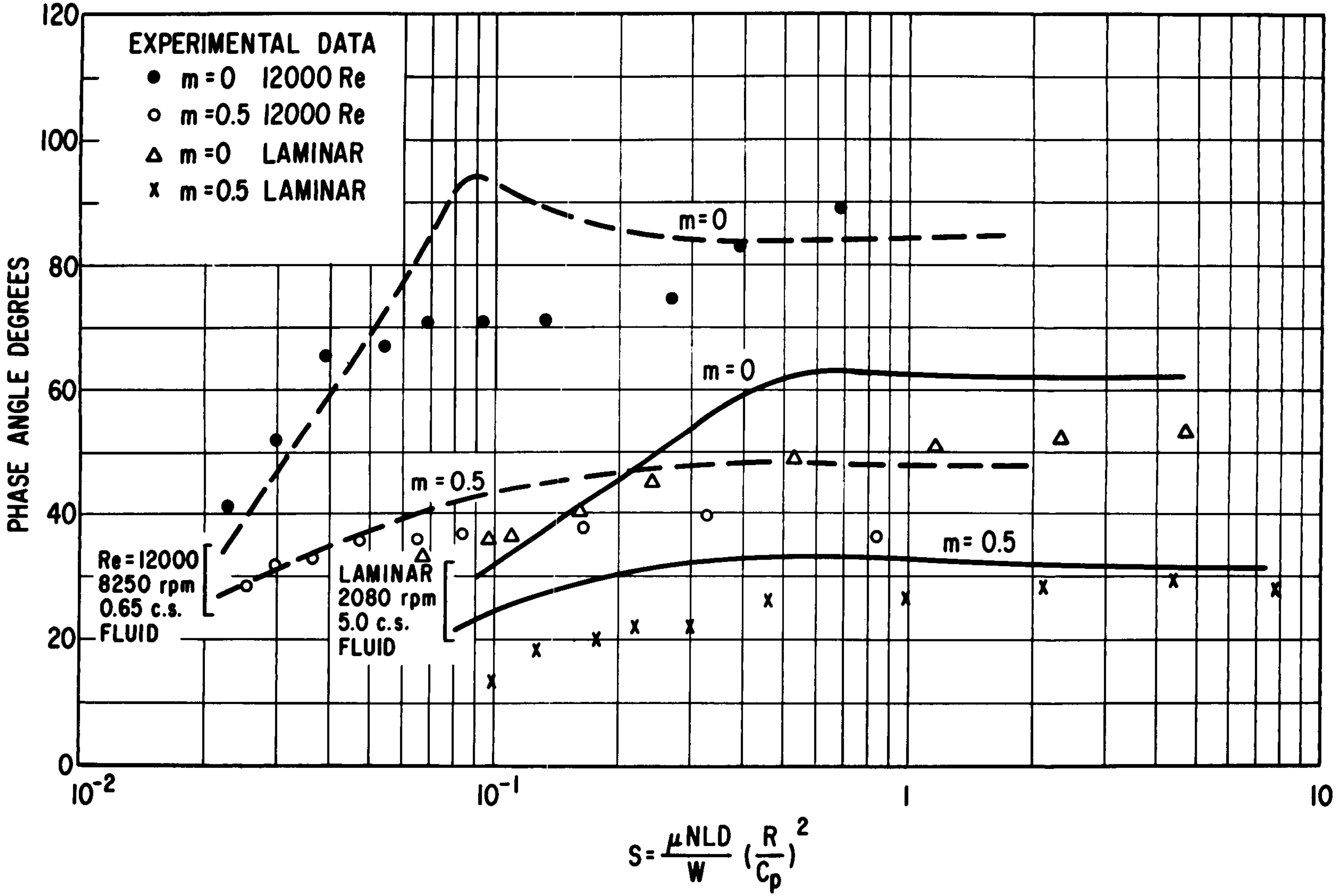

Figure 46. - Comparison between calculated and measured dynamic load response phase angles.

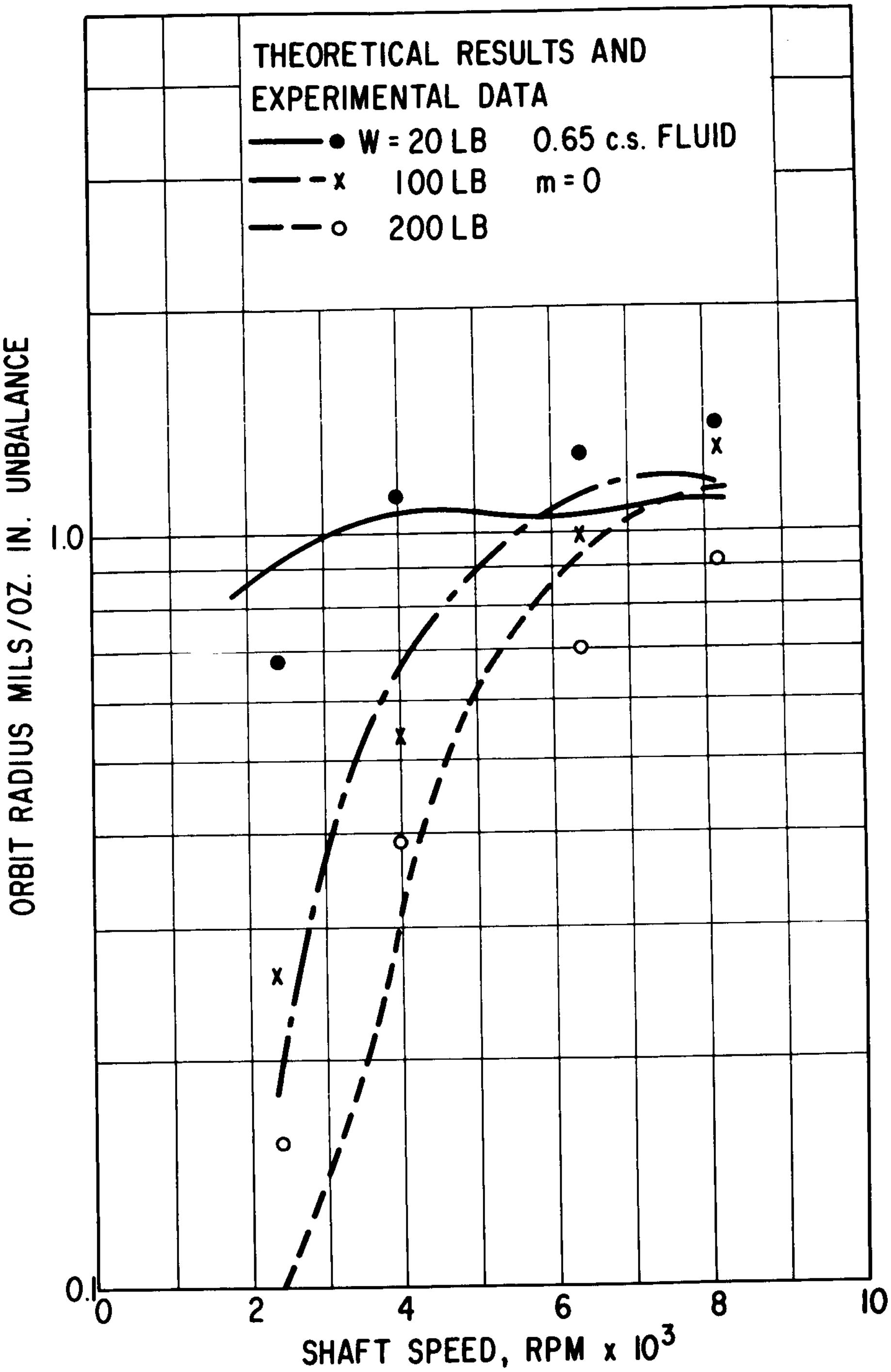

Figure 47. - Sample rotor response design analysis curves - m = 0.

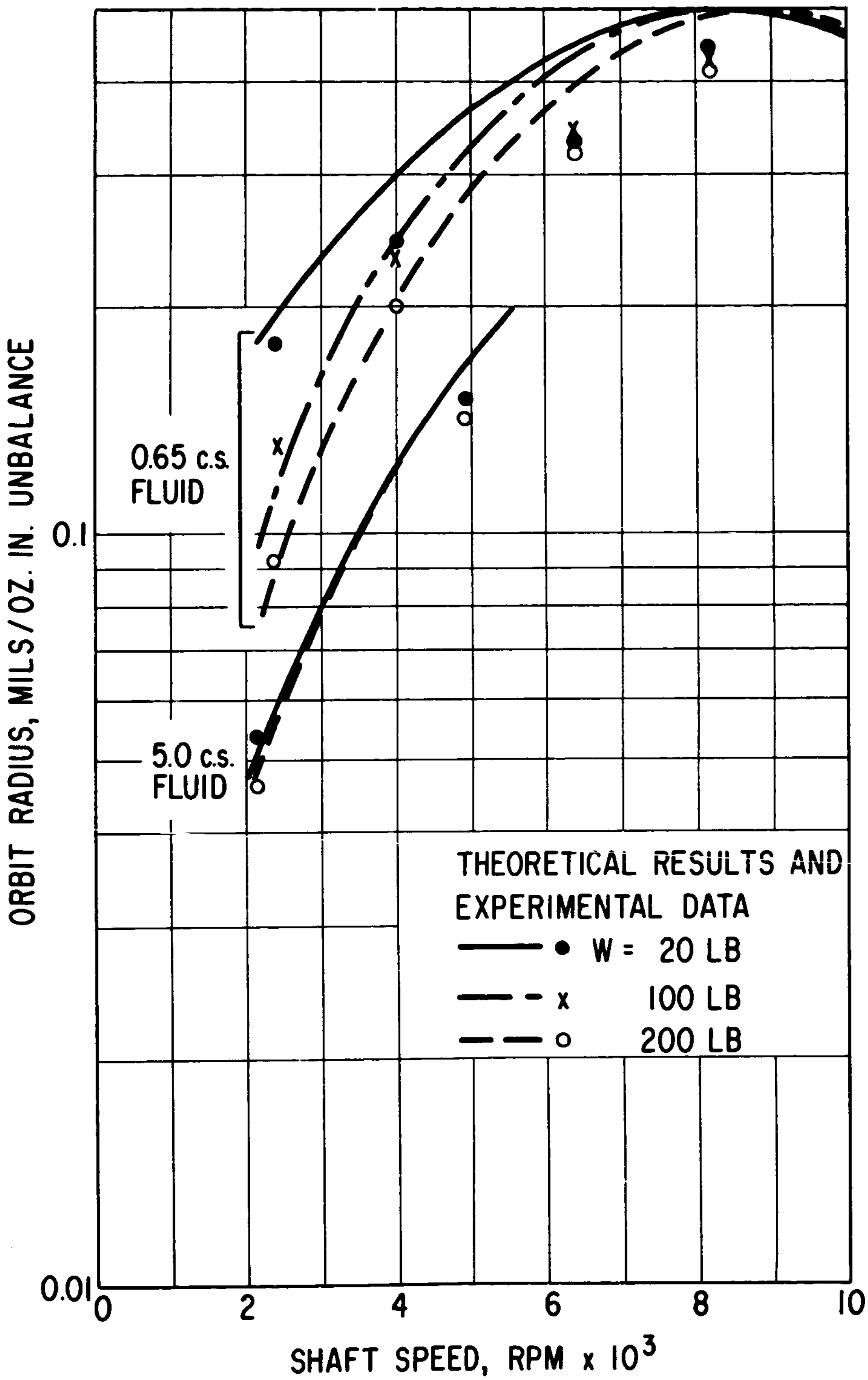

Figure 48. - Sample rotor response design analysis curves - m = 0.5.

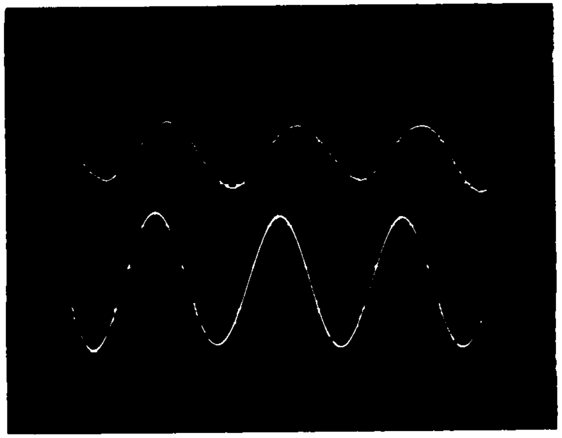

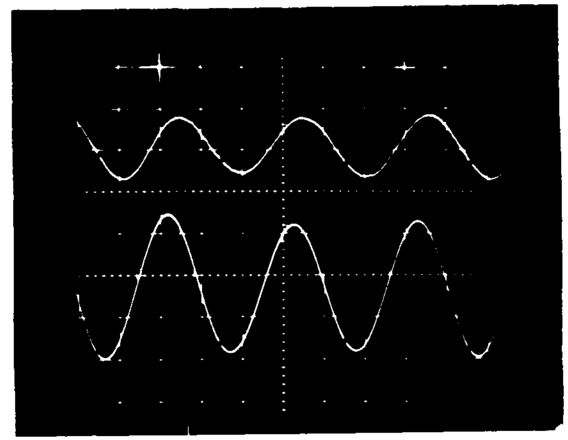

(a) 20 lb load, 0.216 mil/div., 2.5 msec/cm.

(b) 200 lb load, 0.216 mil/div., 2.5 msec/cm.

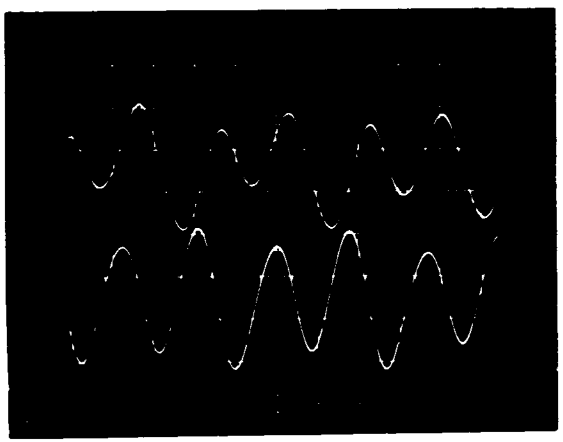

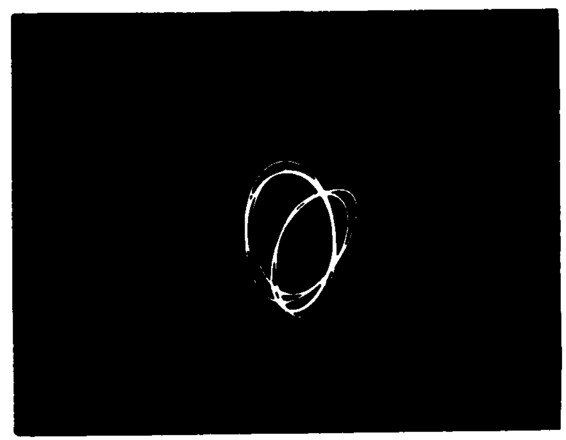

(c) 20 lb load, 0.432 mil/div., 10 msec/div. m = 0, roll and pitch motions of bearing pad.

(d) 20 lb load, 0.432 mil/div., m = 0, shaft center motion with fractional frequency whirl (3000 rpm)

Figure 49. - Oscilloscope traces of pad and shaft motions for stable and unstable operation. In all cases there was a synchronous unbalance load on the shaft.

NASA-Langley, 1967 — 17 E-3718

"The aeronautical and space activities of the United States shall be conducted so as to contribute . . . to the expansion of human knowledge of phenomena in the atmosphere and space. The Administration shall provide for the widest practicable and appropriate dissemination of information concerning its activities and the results thereof."

—NATIONAL AERONAUTICS AND SPACE ACT OF 1958

NASA SCIENTIFIC AND TECHNICAL PUBLICATIONS

TECHNICAL REPORTS: Scientific and technical information considered important, complete, and a lasting contribution to existing knowledge.

TECHNICAL NOTES: Information less broad in scope but nevertheless of importance as a contribution to existing knowledge.

TECHNICAL MEMORANDUMS: Information receiving limited distribution because of preliminary data, security classification, or other reasons.

CONTRACTOR REPORTS: Scientific and technical information generated under a NASA contract or grant and considered an important contribution to existing knowledge.

TECHNICAL TRANSLATIONS: Information published in a foreign language considered to merit NASA distribution in English.

SPECIAL PUBLICATIONS: Information derived from or of value to NASA activities. Publications include conference proceedings, monographs, data compilations, handbooks, sourcebooks, and special bibliographies.

TECHNOLOGY UTILIZATION PUBLICATIONS: Information on technology used by NASA that may be of particular interest in commercial and other non-aerospace applications. Publications include Tech Briefs, Technology Utilization Reports and Notes, and Technology Surveys.

Details on the availability of these publications may be obtained from:

SCIENTIFIC AND TECHNICAL INFORMATION DIVISION

NATIONAL AERONAUTICS AND SPACE ADMINISTRATION

Washington, D.C. 20546